The effects of lithospheric thickness variations on the dynamics of the Earth's upper mantle.

by

Christopher Thomas Harig

B.S., Cornell University, 2004

A thesis submitted to the

Faculty of the Graduate School of the

University of Colorado in partial fulfillment

of the requirements for the degree of

Doctor of Philosophy in Geophysics

Department of Geology

2010

This thesis entitled:
The effects of lithospheric thickness variations on the dynamics of the Earth's upper mantle.
written by Christopher Thomas Harig
has been approved for the Department of Geology

Prof. Peter Molnar

Prof. Shijie Zhong

Date

The final copy of this thesis has been examined by the signatories, and we find that both the content and the form meet acceptable presentation standards of scholarly work in the above mentioned discipline.

Harig, Christopher Thomas (Ph.D., Geophysics)

The effects of lithospheric thickness variations on the dynamics of the Earth's upper mantle.

Thesis directed by Prof. Peter Molnar

The first-order cause of lithospheric motion at the Earth's surface is convection within the mantle. I examine how lithospheric thickness variations affect the dynamics of the upper mantle and the impact they can have on the surface in a series of analytical and numerical experiments. Perturbations to the thickness of mantle lithosphere from horizontal shortening are considered as Rayleigh-Taylor instabilities. This deformation is considered in the context of the Sierra Nevada range in California, where lithosphere may be downwelling and the lower crust may be weak. Lithospheric instabilities are also considered in relation to intracontinental magmatism, several hundred kilometers away from active plate boundaries or rift zones. In cratonic regions, where lithosphere can be several times thicker than the global average, the motion of continental keels cause pressure gradients within the upper mantle. Constraints on upper mantle viscosity can be obtained by considering the dynamic gravity effects from these induced pressure gradients. At subduction zones the motion of subducted lithosphere within the mantle is examined along with its effects on the pressure field and dip angle evolution. Overall, lithosphere of varying thickness can have significant regional impacts on Earth's near surface dynamics, which occur against the background first-order dynamics.

Dedication

To Dana, who's patience knows no bounds.

Acknowledgements

Thanks must begin with my parents. A child could have no better advocates of education.

I would like to thank my thesis advisors, Peter Molnar and Shijie Zhong, for putting some of their best ideas in the hands of a newcomer. Both of them excel at mentoring scientists, not just guiding a student to complete a Ph.D.. I would also like to thank the rest of my committee, Craig Jones, Bob Anderson, and Steve Nerem, for their support and helpful criticism.

I am thankful to Greg Houseman and Frederik Simons for their patience and generosity as I struggled to use their codes. Their initial hard work made my contributions possible.

Thanks to all of my lab mates, especially Walter Szeliga and Joya Tetreault, for the many helpful and enlightening discussions as well as fellowship that I will always remember. Also, the funding generosity of the Department of Geological Sciences, CIRES, and the Graduate School aided my work in times of need.

"I won and I get to scream and jump a little. But I got to go back to work tomorrow." - Benicio Del Toro, Oscar Acceptance

Contents

Chapter

Tables

Table

Figures

Figure

Chapter 1

Introduction

1.1 Motivations

The Earth's lithosphere forms the rigid mobile lid of convection within the mantle. While the oceanic lithosphere is created and later recycled into the mantle with regular frequency, the chemically distinct continental lithosphere persists on the surface for much longer time periods. As these plates collide and separate the thickness of lithosphere can vary by several hundred kilometers. Understanding how these variations in thickness interact with dynamics in the upper mantle is a key to understanding the topography, motion, and geology we see at the surface.

Since variations in lithospheric thickness are largest in continental lithosphere, these regions provide the best opportunity to study these regional dynamics. In this thesis I focus on two aspects of deformation: first, deformation within the lithosphere, and second deformation within the upper mantle. This approach elucidates information on two distinct areas of the Earth's interior, both of which can significantly affect the surface, and on two distinct timescales. The objective is to relate changes at the Earth's surface to processes at depth, which can then be considered in other regions.

Dynamic processes within the Earth are mainly studied with a combination of analytical and numerical models. For analytical models approximations are made both to processes and to the conservation equations in order to find simple relations between, for instance, lower lithosphere thickness and deformation length scales. Numerically, the governing equa-

tions are solved (approximately) with the finite element method, which allows examination of processes with fewer approximations. Together they allow us to infer how processes at depth affect changes in observations at the Earth's surface.

1.2 Outline

Each chapter is written as a scientific paper and can be considered self-contained. Considered together, however, they address different questions of a common theme and examine the interaction between lithosphere and upper mantle from different viewpoints.

In Chapter 2, "Rayleigh-Taylor instability under a shear-stress free top boundary condition and its relevance to removal of mantle lithosphere from beneath the Sierra Nevada" (*Harig et al.*, 2008), I examine the separation of zones of apparent downwelling flow at the ends of the Sierra Nevada in the context of lithospheric instabilities. By using analytical solutions and numerical experiments of Rayleigh-Taylor deformation I show that in geologic situations where the lower crust is weak, instability growth rate factors are enhanced at long wavelengths. Since the separation between downwellings in the Sierra Nevada is larger than commonly assumed for instabilities, it implies that perhaps the lower crust is weak enough that long wavelength instabilities are permissible.

In Chapter 3, "Lithospheric thinning and localization of deformation during Rayleigh–Taylor instability with non-linear rheology and implications for intracontinental magmatism" (*Harig et al.*, 2010a), I examine Rayleigh-Taylor instabilities in the lithosphere in the context of intracontinental magmatism, several hundred kilometers from active subduction or rifting. When viscous deformation in the lower lithosphere is non-linear and viscosity varies little with depth, regions of thinning and thickening can be separated by a coherent block undergoing minimal strain. In this instance, a narrow zone of thinning and upwelling could occur in the continental interior, which could facilitate decompression related volcanism.

Chapter 4, "Constraints on upper mantle viscosity from the flow-induced pressure gradient across the Australian continental keel" (*Harig et al.*, 2010b), examines the motion

of continental keels through the upper mantle, with a concentration on the Australian keel. This motion is expected to induce a pressure gradient in the mantle and result in dynamic topography at the surface. I use three-dimensional finite-element calculations to study this deformation and the resulting topography. By analyzing the modeled and observed geoid anomalies over the Australian continental keel, I place constraints on the viscosity of the upper mantle.

Chapter 2

Rayleigh-Taylor instability under a shear-stress free top boundary condition and its relevance to removal of mantle lithosphere from beneath the Sierra Nevada

2.1 Abstract

The separation of zones of apparent downwelling flow at the ends of the Sierra Nevada suggest a relatively large wavelength (≈500km) of unstable growth, but Rayleigh-Taylor instability for plausible rheological structures with a fixed top boundary condition require much shorter wavelengths (<100km) for maximum growth rates. To understand this difference we analyze analytical solutions and perform numerical 2D plane-strain experiments for Rayleigh-Taylor instability of a dense layer overlying a less dense substratum, representing the instability between the mantle lithosphere and the underlying asthenosphere, focusing on the effects of a shear-stress free boundary condition at the top. The overall effect of this condition is an enhancement of growth rate factors at long wavelengths, which depends greatly on the exponential viscosity variation with depth of the layer. With large or little variation across the unstable layer, the solutions approximate those with a fixed top boundary condition, or for constant viscosity, respectively. An intermediate zone showing the enhanced growth rates includes ratios of layer thickness to viscosity e-folding length, h/L, of ≈ 1 - 8 for Newtonian viscosity, and ≈ 1 - 4 for non-linear viscosity. The free top condition is likely applicable to geologic situations where the lower crust is weak. Olivine flow laws and low temperature estimates at 35km depth (255–355°C) place the Sierra Nevada viscosity

scaling ratio, h/L, between 5 and 9. Thus longer wavelengths than commonly assumed for Rayleigh-Taylor instabilities seem permissible when viscosity decreases with depth and the top surface of the layer is only weakly constrained.

2.2 Introduction

The conductive temperature profile across the mantle lithosphere indicates that the mantle lithosphere should be more dense than the underlying upper mantle when brought to the same pressure, assuming no compositional differences. This density contrast is inherently unstable. Small temperature, and hence density, perturbations to this layering are normally destroyed by thermal diffusion, but if a perturbation is large or can grow fast enough, thermal diffusion can be neglected due to its long timescale. In this case, the mantle lithosphere can be treated as a case of Rayleigh-Taylor instability (*Canright and Morris*, 1993; *Chandrasekhar*, 1961; *Conrad and Molnar*, 1997). For Newtonian viscosity density perturbations will initially grow exponentially with time. When perturbations grow to several tens of percent of the unstable layer thickness, sinking regions will downwell into the upper mantle super-exponentially (e.g. *Canright and Morris*, 1993). As it is removed, mantle lithosphere will be replaced with less dense asthenosphere in the isostatic column. Therefore this removal would cause the surface to rise to maintain pressure balance (e.g. *Bird*, 1978; *England and Houseman*, 1989).

In Tibet, an area of much current study, convective removal of thickened Asian lithosphere is one (*Houseman et al.*, 1981) of many tectonic processes proposed to occur beneath the Tibetan Plateau in response to the Indian-Eurasian collision (e.g. *Dewey and Bird*, 1970; *Dewey and Burke*, 1973; *Ni and Barazangi*, 1983; *Owens and Zandt*, 1997; *Willett and Beaumont*, 1994; *Zhao and Morgan*, 1985). The upper mantle of the Tibetan plateau is characterized by large east-west seismic wave speed gradients and attenuation, and possible north-south wave speed gradients (e.g. *Dricker and Roecker*, 2002; *McNamara et al.*, 1997; *Molnar*, 1990; *Ni and Barazangi*, 1983; *Woodward and Molnar*, 1995). Additionally,

tomographic imaging has revealed what seems to be a narrow zone of downwelling mantle lithosphere beneath central Tibet (*Tilmann et al.*, 2003). Together, these observations suggest a dynamic origin for some of the plateau's deformation such as high mean elevation and the distribution of normal faulting across the plateau (*Houseman and Molnar*, 1997). What remains uncertain, however, is the length scale of mantle lithosphere deformation. Studies covering both large areas, such as *Dricker and Roecker* (2002) ($\approx 25°$), and small areas, such as *Tilmann et al.* (2003) ($\approx 5°$), show lateral variations in the upper mantle on these scales.

In the Sierra Nevada in California, the evidence favoring removal of mantle lithosphere from beneath the range is clearer. Examination of entrained xenoliths between depths of 40 and 100km from before 8 Ma indicate the presence of a 40 - 60 km eclogite-rich layer beneath the Sierran batholith in the crust (*Ducea and Saleeby*, 1996, 1998; *Lee et al.*, 2001). Magmatism at 3.5 Ma and additional xenoliths erupted since imply the absence of this eclogite layer and presumably its removal by this time, and logically, the deeper mantle lithosphere as well (*Farmer et al.*, 2002). Indications of this removal event are also seen in geomorphic observations. For instance, there is evidence of tilting with an increase in height of the range crest on its western range flank (e.g. *Stock et al.*, 2004; *Unruh*, 1991), a fairly uniform westward shift of the edge of normal faulting and horizontal extension around 3.5 Ma, and possible initiation of folding and thrust faulting along the western margin of the Sierran micro-plate (*Jones et al.*, 2004).

Two high seismic wave speed anomalies, the Isabella and Redding anomalies, extending to more than 250 km depth beneath the Central Valley near the ends of the range are likely locations for the removed lower lithosphere (Figure 2.1) (*Benz and Zandt*, 1993; *Jones et al.*, 1994; *Reeg et al.*, 2007). Both the Isabella (*Jones and Phinney*, 1999) and the Redding anomalies (*Hartog and Schwartz*, 2000; *Özalaybey and Savage*, 1995) are seismically isotropic which can be characteristic of eclogites (*Fountain and Christensen*, 1989). Furthermore, the area above the Isabella anomaly is undergoing active subsidence, which would be expected over such a downwelling (*Saleeby and Foster*, 2004). Certainly, there is not complete north-

south symmetry to the Sierra Nevada Pliocene history, as the passing of the southern edge of the Gorda plate and Mendocino Fracture Zone illustrates (*Atwater and Stock*, 1998). But, it seems more likely than not that the two anomalies are the result of the same process, and very reasonable to postulate so (*Jones et al.*, 2004; *Le Pourhiet et al.*, 2006).

Although Rayleigh-Taylor experiments have been carried out for no-slip top boundary conditions and differing rheological structures, the $\approx$ 500 km separation of the Sierran anomalies is significantly longer than the wavelength for the peak growth rates for these conditions. Simple experiments (constant viscosity, constant density) have shown that the wavelength corresponding to maximum growth rate factor is about three times the unstable layer thickness ($\lambda_{max} \approx 3h$) (e.g. *Conrad and Molnar*, 1997). Other experiments have shown that a buoyant crustal layer also influences the growth rate of instabilities and suppresses growth of longer wavelengths (*Neil and Houseman*, 1999). We explore what other factors might influence the Rayleigh-Taylor instability process to favor the growth of longer wavelength perturbations and downwellings.

Our goal is to determine the effects of a shear-stress free boundary between the crust and mantle lithosphere on growth rates of Rayleigh-Taylor instability under various rheological stratification, such as exponentially varying viscosity with depth. This boundary condition represents one possible end member, with the other being a no-slip top boundary condition. The state of Sierran lithosphere at the time convective removal began was surely in between these two idealized states. Arguments can be made, however, that both are reasonable approximations.

The thermal structure of the lithosphere around 10 Ma can be inferred from several measures. The present day surface heat flux in the western Sierra is very low (18 to $60 mW m^{-2}$), and can bound the temperature at 35 km depth to 255–355°C simply by assuming a steady state (*Lachenbruch and Sass*, 1977; *Saltus and Lachenbruch*, 1991). Separate temperature estimates from xenolith geothermometry can bound the temperature at greater depth, 130 km, to only 925°C (*Ducea and Saleeby*, 1998). A steady state using this measure-

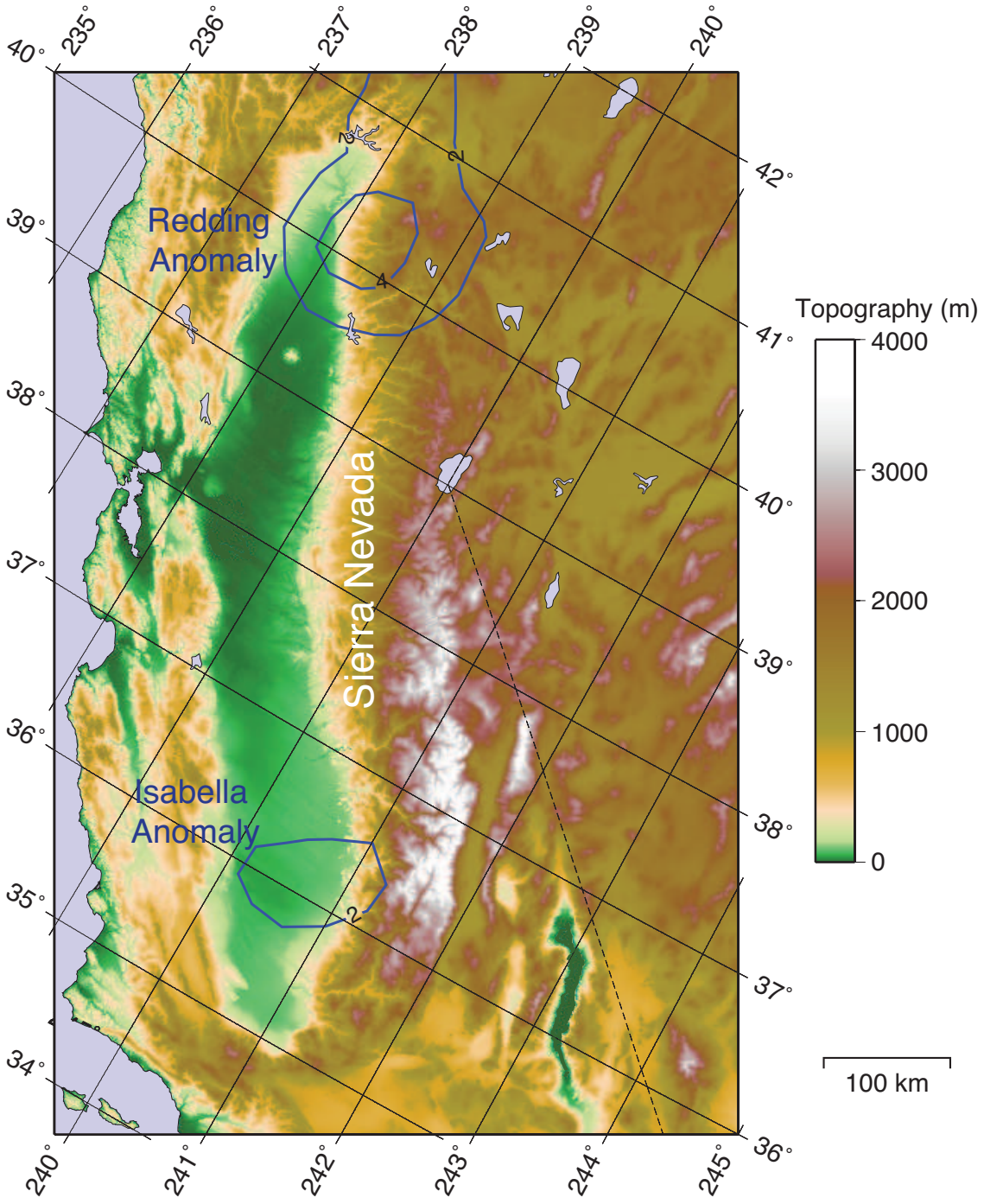

Figure 2.1: Map view of the Sierra Nevada range in California with colored topography from The Global Land One-km Base Elevation (GLOBE) Project. High speed seismic anomalies at about 150km depth are contoured in percent V_p perturbation from the IASP91 model. Tomography contour provided from *Reeg et al.* (2007).

ment would indicate a temperature at 35 km depth of similar range to before, 250–350°C (*Molnar and Jones*, 2004). Thus, on the one hand, very low lithosphere temperatures might be used to assume a no-slip condition at the Moho with an undeforming crust. Alternatively, as mentioned, the Sierra Nevada is estimated to have had a 40 - 60 km thick eclogite-rich layer beneath the batholith (*Ducea and Saleeby*, 1996, 1998; *Lee et al.*, 2001). Field observations of eclogite and granulite (e.g. *Austrheim*, 1991) have shown that eclogites can deform with much lower viscosity than their granulite protoliths. Moreover, the felsic quartz-rich upper crust that survives today could have been weak even at the low temperatures estimated for depths of 30-40 km, for quartz flows at relatively low shear stress at such temperatures (e.g. *Brace and Kohlstedt*, 1980; *Sibson*, 1977, 1982).

Jull and Keleman (2001) examined the conditions under which dense mafic lower crustal material could become convectively unstable. Under their most extreme circumstances, such as an assumed background strain rate of $10^{-14}s^{-1}$, Moho temperatures as cold as $550 - 650$°C could produce an instability in 10 Myr for a dense layer 10 km thick immediately below. Given estimates for a Sierran eclogite layer are much thicker, it is possible the bottom several kilometers were at or above this range of temperatures. An instability initiated in the Sierra mantle lithosphere could provide the background strain rate necessary, and eclogite could be swept along with lower material. Thus, if viscosity of the middle crust were sufficiently low, the top boundary condition appropriate for removal of this eclogite layer with the underlying mantle lithosphere could be approximated by a shear-stress free boundary, either at the Moho or within the eclogite layer. Here, we present both analytical and numerical solutions to idealized problems with this stress-free boundary above our unstable layer.

2.3 Background Theory and Methods

The Rayleigh-Taylor instability problem in the Earth is one of Stokes flow for viscous fluids, representing a balance between body forces and surface tractions after assuming

incompressibility and neglecting inertial terms. The governing equation takes the form:

$$\frac{\partial \sigma_{ij}}{\partial x_j} - \rho g \delta_{iz} = 0 \tag{2.1}$$

where σ_{ij} are stress components, x_j are spatial coordinates, ρ is density, g is gravity, and δ_{ij} is the Kronecker delta. We solve this equation for a material layer overlying a less dense half-space (or a subspace of finite depth), seen schematically in Figures 2.2 and 2.3. We allow for a general non-linear constitutive equation between deviatoric stress,τ_{ij}, and strain rate,$\dot{\epsilon}_{ij}$,

$$\tau_{ij} = B\dot{E}^{(1/n-1)}\dot{\epsilon}_{ij} \tag{2.2}$$

where $\dot{E}$ is the second invariant of the strain-rate tensor, n is the rheological exponent, and B is the viscosity coefficient. Under familiar Newtonian rheology, $n = 1$, and we have the relation $\eta = (1/2)B$. For a non-Newtonian fluid, $n > 1$, viscosity is strain-rate dependent as $\eta_{eff} = (1/2)B\dot{E}^{(1/n-1)}$, where η_{eff} is an effective viscosity, which changes as strain rates change with time.

Temperature gradients inherent to the mantle lithosphere will cause viscosity to vary within the layer. Laboratory experiments have shown that linear temperature gradients translate approximately to an exponential variation of viscosity with depth (e.g. *Fletcher and Hallet*, 1983). We therefore consider cases in which B varies exponentially with depth, as seen in Figure 2.2. Depth, z, is set to zero at the interface between layers of different density and decreases downward. Viscosity, η, then takes the form:

$$\bar{\eta} = \eta_0 e^{(\gamma z)} \tag{2.3}$$

where η_0 is the viscosity at the layer interface, and $1/\gamma = L$ is the viscosity (e-folding) decay length. Various values of decay length are used so that over a layer of thickness h we have $h\gamma = 1, 2, 4$, etc.

We also perform calculations with different density structures. The majority of our work is done with a constant density difference. For a few cases we use density decreasing

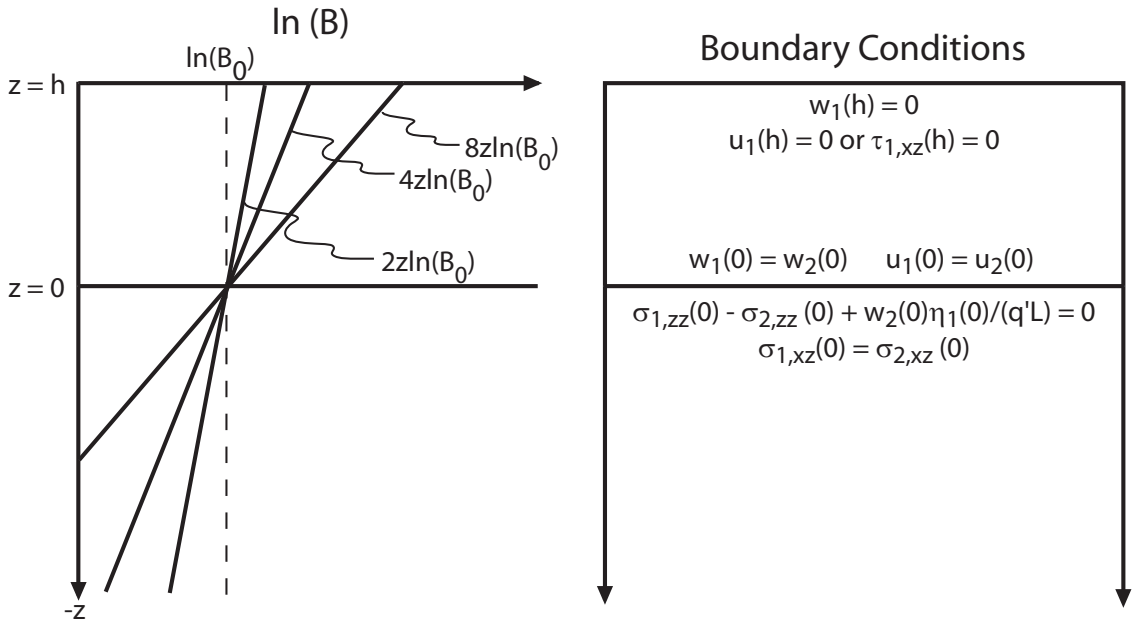

Figure 2.2: Viscosity structure (left) and Linear Stability boundary conditions (right). Depth, z, is zero at the bottom interface of the unstable layer and decreases downward. $z = 0$ represents the bottom of the mantle lithosphere, and $z = h$ represents the shear-stress free top surface, which could be either at the Moho or within the lower crust. We include the unused fixed-top condition to better show the difference to previous work. Viscosity is an exponential function with depth, and B is the viscosity coefficient. Subscripts of 1 are for quantities in the layer while subscripts of 2 are quantities of the lower half-space.

linearly with depth in the layer, as would be the case for a linear temperature gradient in the lithosphere and a constant coefficient of thermal expansion. Linear density takes the form

$$\rho(z) = \frac{2\Delta\rho}{h} z \tag{2.4}$$

so that over a layer of thickness h, the dimensionless $(\rho(z)/\Delta\rho)$ density at the top and bottom surfaces are 2 and 0 respectively, and we have the same total mass anomaly in the layer in both sets of experiments. The density anomaly in the substrate is zero.

To simplify solutions, we non-dimensionalize growth-rate factors (q) and wavenumbers (k) by the appropriate length- and time-scales. Symbols used here and elsewhere are listed in Table 4.1. For exponentially varying Newtonian viscosity with depth we have

$$q'_L = q\frac{2\eta_0}{\Delta\rho g L}, \qquad k'_L = kL \tag{2.5}$$

with subscripts denoting the choice of non-dimensionalization as in *Molnar et al.* (1998). The time-scale $\frac{2\eta_0}{\Delta\rho g L}$ is determined from the time required to produce unit strain under a deviatoric stress of magnitude $\Delta\rho g L$. We also devote some discussion later to comparisons between cases with large viscosity variations and those with no viscosity variations, given the different non-dimensionalizations required.

We perform linear stability analyses for cases with constant density to find analytical solutions for growth rate factor, q' as a function of dimensionless wavenumber, $k' = kL$. With linear stability, the assumed form of solution for $n = 1$ cases is

$$W(z)f(x,y)e^{qt} \tag{2.6}$$

where

$$\nabla^2 f(x,y) = -k^2 f(x,y). \tag{2.7}$$

$W(z)$ is the function of downward velocity dependent on z and $f(x,y)$ is a harmonic function with wavenumber k, here assumed to be $cos(kx)$. We consider only first order perturbations to background stress and strain rates, and follow the approach of *Conrad and Molnar* (1997). The boundary conditions for these cases are shown in Figure 2.2.

Linear stability analyses are paired with 2D plane-strain numerical calculations using the finite element program Basil (http://homepages.see.leeds.ac.uk/~eargah/basil/). For numerical experiments of a layer over an inviscid half-space, a single layer of triangular mesh is created from $0 \leq z \leq h$ and a harmonic perturbation of $0.01(1-z)$ amplitude is applied to the mesh. Velocity fields and subsequent deformation are then calculated iteratively through time. For cases of a viscous substratum, we follow a similar process, but the mesh is extended from $-4h \leq z \leq 1h$. This depth is chosen to strike a balance between minimizing the influence of the bottom boundary of the substratum and the calculation requirements of a finer mesh. Boundary conditions for the calculation are shown in Figure 2.3. For each experiment the bottom boundary of the unstable layer is perturbed using a specific wavelength equal to twice the width of the box, and to sample the k' spectrum we varied

the horizontal dimension of the box. For Newtonian viscosity calculations, $n = 1$, we fit $|Z'|$, the absolute value of the vertical coordinate of the maximum downwelling, vs. dimensionless time, t' ($= \frac{\Delta\rho g L}{2\eta_0}$), to a straight line of the form

$$ln|Z'| = lnZ_0 + q'_{est}t' \tag{2.8}$$

to estimate the growth rate factor, q'_{est}. Line fitting is limited to the section of growth that follows the decay of initial transient, and before growth to large amplitudes (a few tens of percent). We plot both growth rate curves from linear stability analyses and numerical values of q'. In general the numerical results agree within 3% of linear stability analyses.

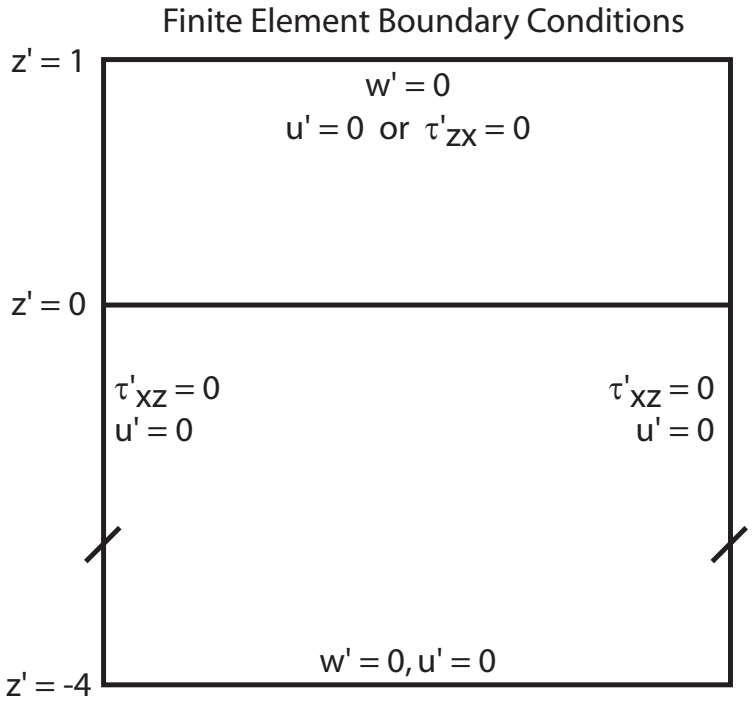

Figure 2.3: Finite element calculation boundary conditions for a viscous half-space. Again, $z' = 0$ is the bottom of the unstable layer (i.e. the mantle lithosphere) and $z' = 1$ represents the shear free top surface (i.e. at the Moho or within the lower crust). We also include the unused fixed-top condition to better show the difference to previous work. In calculations with an inviscid half-space, the mesh extends from 0 to 1.

For calculations with a non-linear (non-Newtonian) viscosity relation we use a power

law exponent of $n = 3$. Following *Houseman and Molnar* (1997), lines of the form

$$Z'^{(1-n)} = (n-1)\left(\frac{C}{n}\right)^n (t'_b - t') \tag{2.9}$$

with $t' = t(\frac{\Delta\rho g L}{B})^n$ are fit to the output position data Z'. Here, t'_b represents the time when the downward speed of the downwelling approaches infinity, signaling when the blob would drop off completely from the layer. C is a dimensionless parameter analogous to the growth rate factor, q', in Newtonian calculations, which we will use to compare growth rates for various wavenumbers.

2.4 Exponentially Varying Newtonian Viscosity with Depth

2.4.1 Inviscid Substratum and Constant Density

In the most basic Rayleigh-Taylor experiments there is a fundamental difference between using a no-slip and a free-slip boundary condition at the top of the unstable layer. The use of a no-slip boundary condition ensures that as k' approaches zero, the growth rate factor q' also approaches zero (e.g. *Conrad and Molnar*, 1997; *Molnar et al.*, 1998; *Whitehead and Luther*, 1975). When the free-slip condition is used, however, q' can be finite in the limit of small k', as in the linear stability analysis in Figure 2.4. We plot four simple cases with constant viscosity and density to illustrate this difference, and show how the addition of a viscous substratum can retard growth. Here, the case with a free top and an inviscid subspace maintains a finite value near $k' = 0$, but the other cases trend to 0 when $k' \to 0$. We further examine this difference with more complex, depth-varying physical properties.

If there is significant viscosity contrast between the mantle lithosphere and asthenosphere, any motion will be dominated by the viscosity of the lithosphere. In this instance, the asthenosphere can be approximated by an inviscid substratum of infinite depth by setting the ratio $\eta_{astheno}/\eta_{man.lith} \to 0$. Considering this assumption in the context of stagnant lid convection, we can imagine how the mantle lithosphere could deform irrespective of asthenosphere influence (*Moresi and Solomatov*, 1995). We begin by examining cases that use

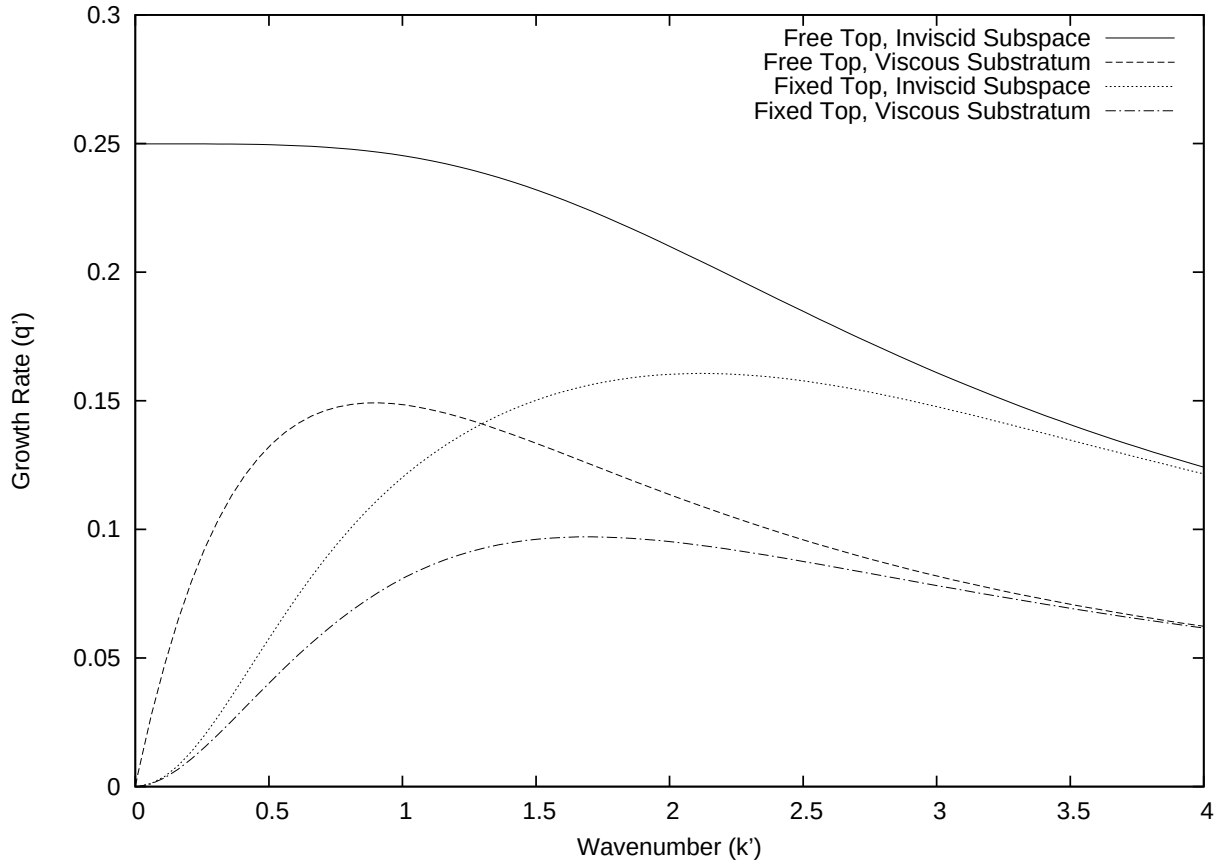

Figure 2.4: Linear stability analysis curves of growth rate factors (q') vs. wavenumber (k') for simple, previously known experiments. The free-top cases were discussed briefly in *Hoogenboom and Houseman* (2006) and substratum viscosity was explored in *Molnar et al.* (1998), though with a fixed-top condition. These cases have density and viscosity constant with depth, but vary in their top boundary condition and subspace viscosity.

this approximation for the subspace and depth varying viscosity in the unstable layer above it. We examined a range of h/L values with results shown in Figure 2.5. These calculations exhibit two styles of growth. For large viscosity variations across the layer ($h/L > 8$), growth rate curves approach those for the case with exponential viscosity in two infinite halfspaces, from *Conrad and Molnar* (1997). The viscosity in the top part of the layer becomes so great that its free boundary is essentially removed from the problem. When the ratio of h/L drops below ≈ 8, however, the growth rates transition to a style characteristic of a free top, with finite q' at $k' = 0$. Here, the entire layer is involved in the foundering, and the stress-free

boundary condition at the surface becomes important.

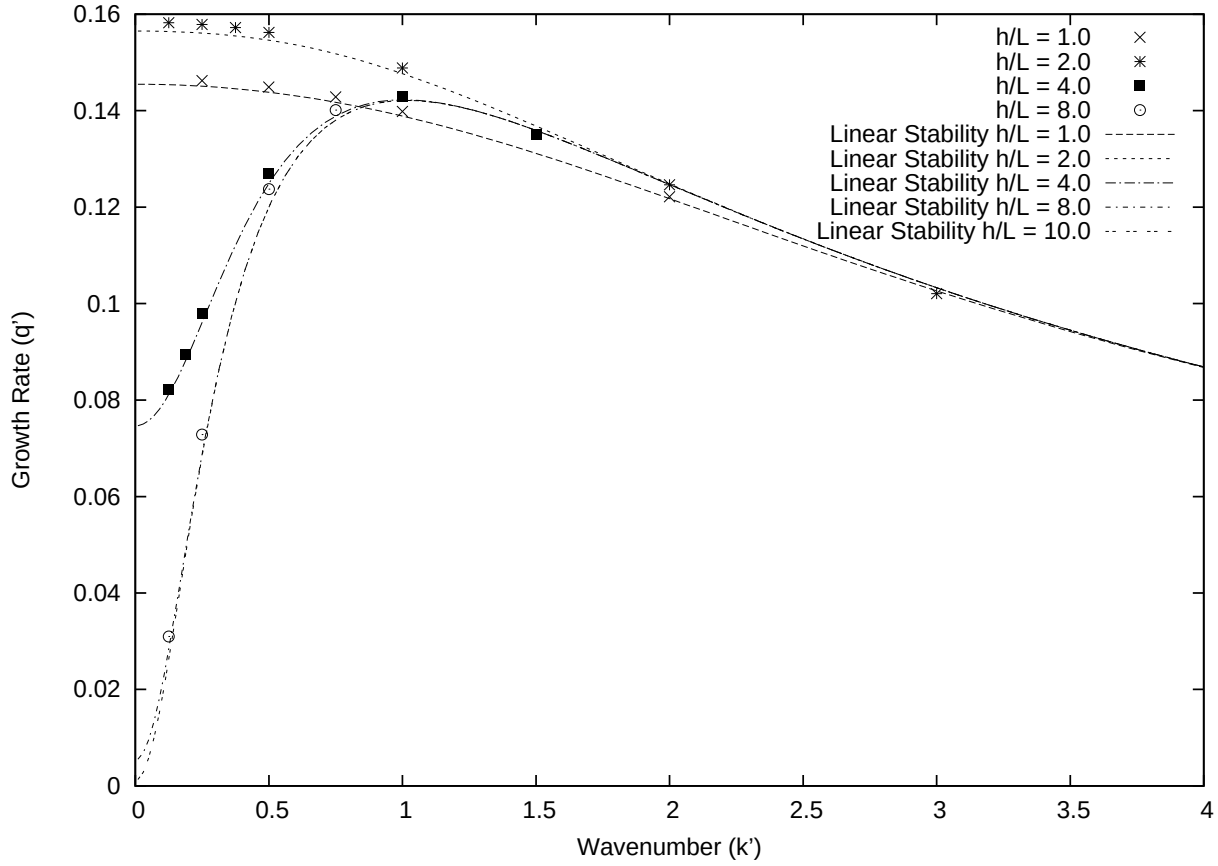

Figure 2.5: Growth rate vs. wavenumber for various values of h/L. Dashed lines are results of Linear Stability analysis. Points are results of numerical calculations. This experiment is a layer over an inviscid halfspace. The layer has exponentially varying viscosity and a stress free top boundary condition. Note that curves for Linear Stability $h/L = 8$ and 10 are co-incident everywhere except close to $k' = 0$.

2.4.2 Viscous Substratum and Constant Density

We also perform experiments using a viscous substratum, by continuing the exponential viscosity scaling to greater depth. When a viscous substratum is added, in this case to depth of $z = -4h$, the form of the growth rate changes slightly (Fig. 2.6A.). For large viscosity variations ($h/L > 8$), growth rate curves again approach those of a calculation of exponential viscosity in two infinite halfspaces, with $q' \to 0$ as $k' \to 0$. When the ratio of h/L drops below

≈ 8, however, the growth rates appear to be a blend of both the stress-free and fixed-top styles as in Figure 2.5, showing characteristics of both. For all ratios of $h/L < 8$ examined, q'_{max} does not occur at a wavenumber smaller than $k' \approx 0.5$. Yet for several cases, in the $\lim_{k'\to 0}$, q' remains finite. This contrasts with the behavior for an inviscid substratum in Figure 2.5, where, for $h/L = 1$ and 2, q'_{max} occurred at $k' = 0$. Additionally, in Figure 2.4 we saw the relation

$$\lim_{k'\to 0} q' \neq 0 \tag{2.10}$$

applied only when the viscosity of the substratum is zero. Now we observe a range of viscosity scalings that meet this condition. Thus, exponential viscosity introduces a relative enhancement of growth rate at long wavelength (small wavenumber). Alternatively, the viscous substratum retards the growth rate overall, with increasing effect as $|k'_{q'max} - k'|$ increases. It also affects the wavenumber of maximum growth rate, for $k'_{q'max}$ varies with h/L, and reaches a minimum for the value $h/L \approx 2$, not as $h/L \to 0$.

For both numerical and analytical results, we extend our substratum to a depth of $-4h$. To show the effect of a finite depth on the dependence of q' on k' we plot, in Figure 2.6B, the linear stability curves for both a case with substratum depth limited to $-4h$ (as in Fig. 2.6A) and the same case with an infinite halfspace substrate to illustrate the differences resulting from this approximation. The divergence between the growthrates for the two structures is limited to small wavenumbers ($k' < 0.25$) and h/L ratios below 4.

As h/L transitions through the intermediate window between the small h/L, stress-free and large h/L, fixed-top end member styles, a plot of $\lim_{k'\to 0} q'$ with the $log(h/L)$ for both the viscous (Figure 2.6) and inviscid substrata (Figure 2.5) displays a smooth transition (Figure 2.7a,b). We show this plot for two non-dimensionalizations; Fig. 2.7a displays dimensionless results with respect to L, and Fig. 2.7b shows them with respect to h. Overall, the difference between the inviscid and viscous cases can be thought of as a result of retardation caused by the viscous substratum. This retarding is concentrated where $h/L < 2$. Both curves (for

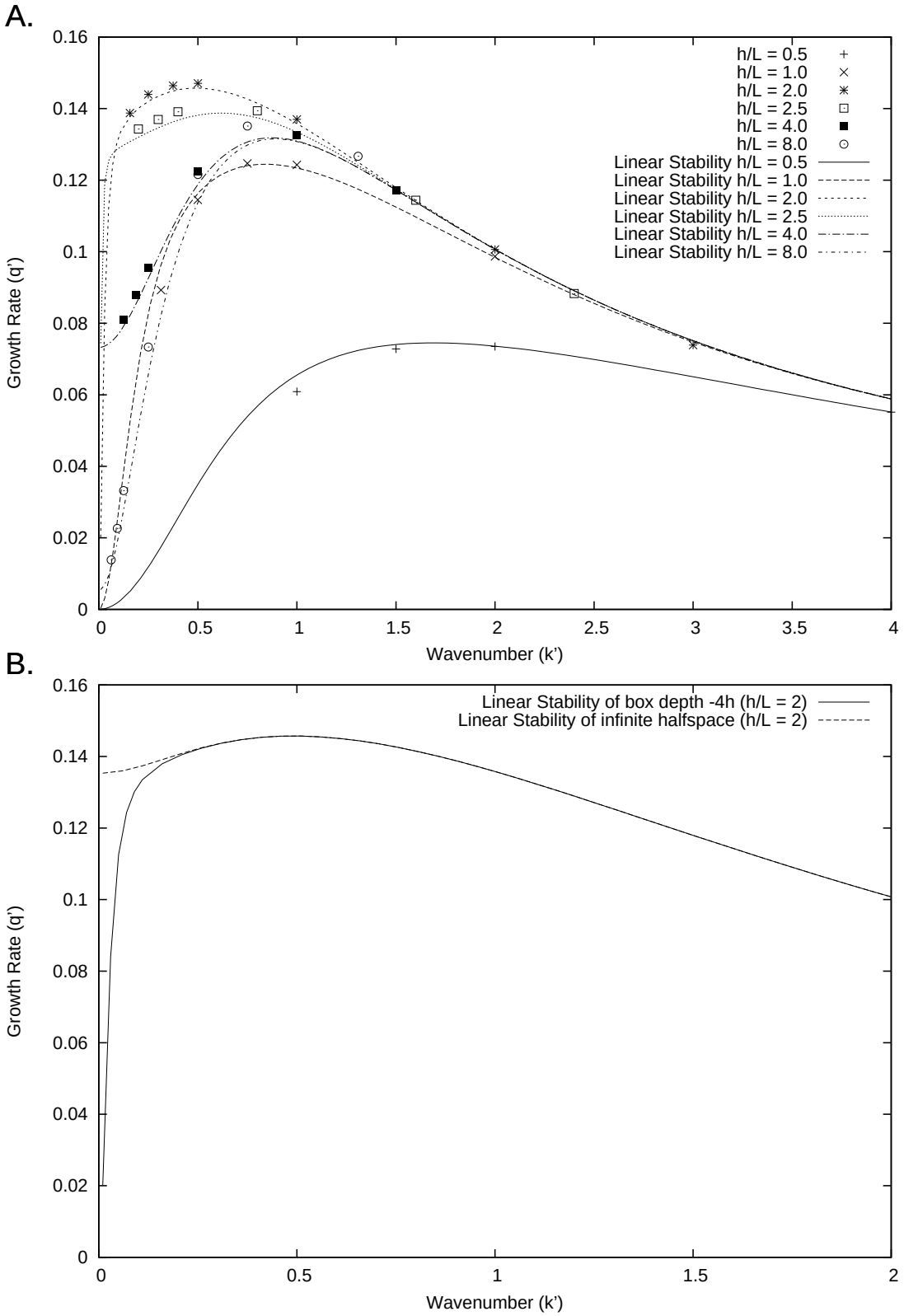

Figure 2.6: A. Growth rate factor vs. wavenumber for an experiment with a free-top and a viscous substratum from $0 < z < -4h$. Both linear stability (lines) and numerical (points) results shown. B. Growth rate factor vs. Wavenumber as above for case of $h/L = 2$ to show the differences resulting from a substratum extending to a depth of $-4h$ depth approximation as opposed to using an infinite halfspace.

both scalings) are similar for the region $h/L >> 1$ as the substratum has little effect due to its relatively low viscosity. In Fig. 2.7a, for values of h/L around 1, we can see that the viscous substratum narrows the band of intermediate growth rate curves, and shifts the peak to a slightly higher h/L value. In Fig. 2.7b, we see that the substratum affects approximately the same h/L range, but with obviously different results. When $h/L << 1$, the growth rate factor scaled by h levels to a value of 0.25 as the viscosity variation approximates a constant value.

For small values of h/L ($h/L < 1$), a non-dimensionalization using h instead of L becomes more sensible, because the growth of perturbations is driven by the density contrast in the layer of thickness h. In such a case (not shown), $q'(k')$ transforms to the solution for constant viscosity, and again, $\lim_{k' \to 0}$, q' is zero as in Figure 2.4.

To understand the long wavelength enhancement of growth rate, we calculate eigenfunctions for the z-component of velocity, w'. Calculating the eigenfunction at infinite wavelength ($k' = 0$) is impossible because the matrix created from applying boundary conditions to the assumed solution form, equation 2.6, collapses to a determinant of zero regardless of growthrate factor; therefore we show a series of eigenfunctions for a fixed value of $k' = 0.1$ and various values of h/L in Figure 2.8. With this series we examine the depth distribution of flow at long wavelength. The unstable layer is from $0 < z' < 1$ and the eigenfunction amplitudes have been normalized so that $w'(0) = 1$. When $h/L = 10$, the eigenfunction in the lower layer is highly oscillatory about zero, indicating that material is being turned over in several small scale sections. For intermediate h/L values, such as $h/L = 1$, the wavelength of the oscillation increases, so that near the layer interface there exists substantial vertical motion. In fact, the curve for $h/L = 10$, the only solution outside the free-top fixed-top transition zone, is the only curve that does not share the same amplitude in the $1 > z' > -1$ region.

Our choice of exponential viscosity in the substrate is one of simplicity. We can compare these growth rate factors to those of the more probable case with constant viscosity in the

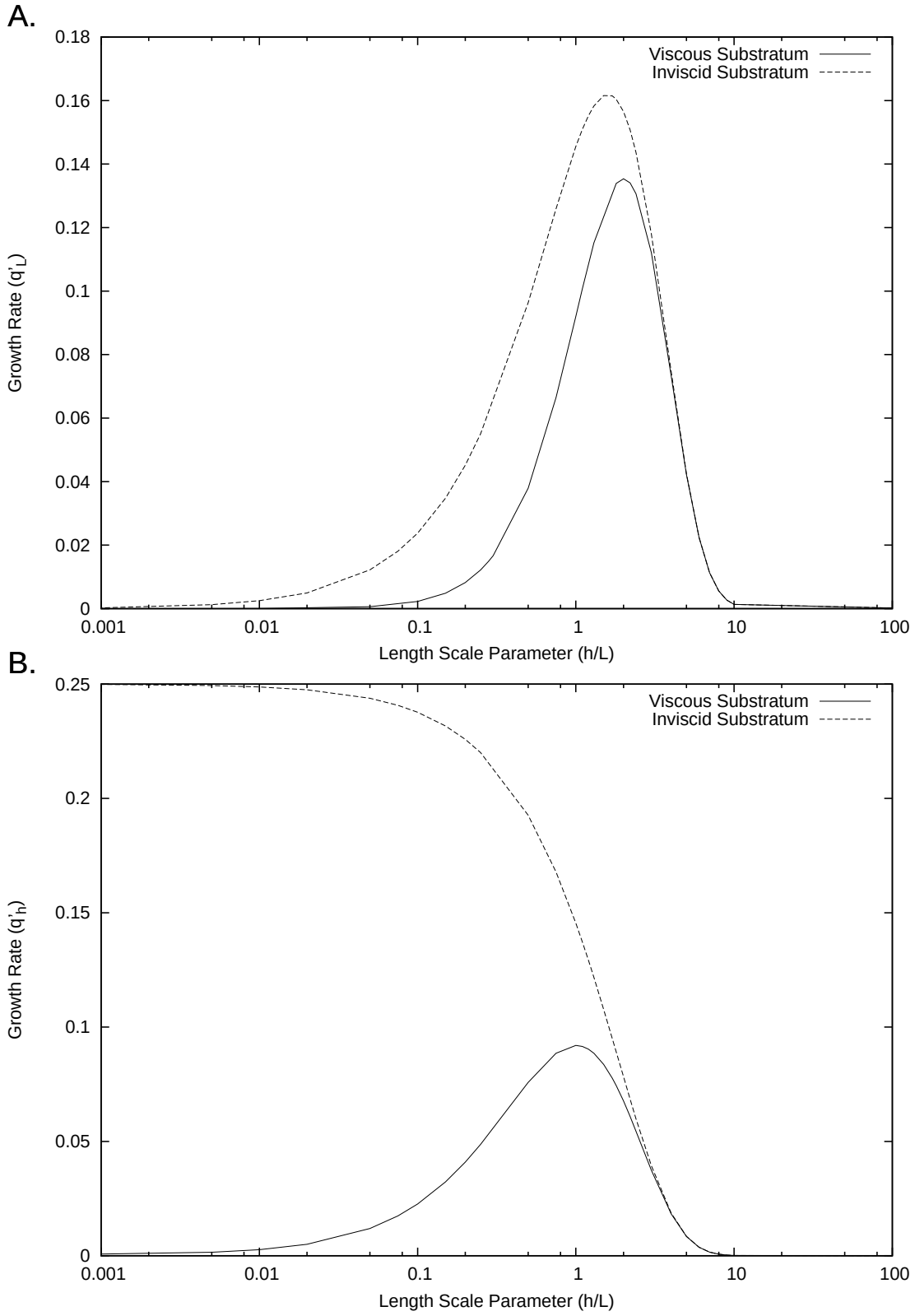

Figure 2.7: Semi-log plots of $\lim_{k' \to 0} q'$ vs. h/L for substrate continuing to negative infinity. A. q' and k' non-dimensionalized by L, for both viscous and inviscid stress free top experiments. Here, $q'_L = q\frac{\eta}{\Delta\rho g L}$. B. Same as A. but q' and k' non-dimensionalized by h, so $q'_h = q\frac{\eta}{\Delta\rho g h}$.

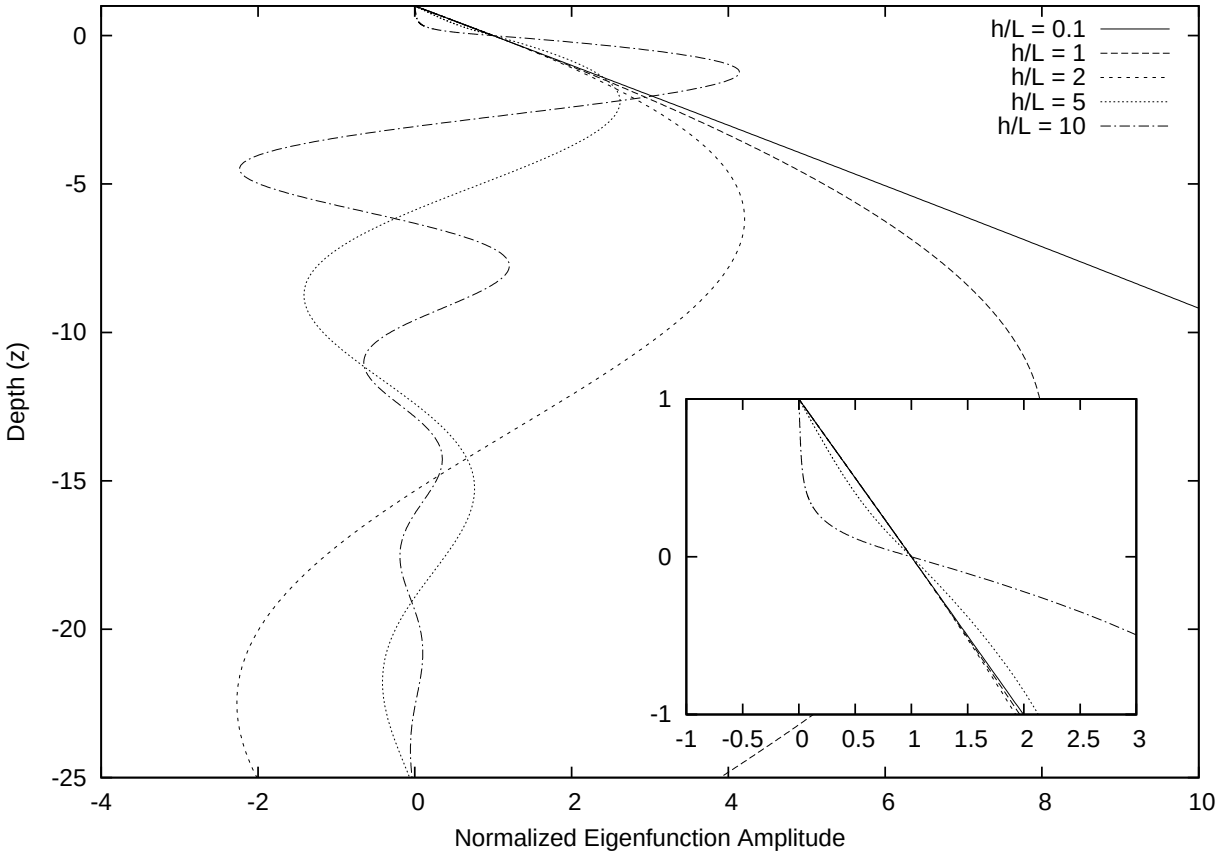

Figure 2.8: Plots of the downward velocity (w') eigenfunction for a fixed values of $k' = 0.1$ and various values of viscosity scaling, h/L. Experiments are for a layer of thickness 1 with bottom boundary at depth 0. The functions are normalized so that the amplitude is 1 at depth 0. Inset is zoom of area around $z = 0$.

substrate ($z' < 0$) for several values of h/L (see Fig. 2.9). Aside from the general differences in growth rate factor amplitude, we see only subtle changes in the small k' regions. A constant viscosity substrate alters growth at very long wavelengths ($k' < 0.4$) so that q' approaches zero at $k' = 0$.

2.4.3 Inviscid Substratum and Linear Varying Density

We also perform experiments with density varying linearly with depth in the layer, shown in Figure 2.10, for which explicit linear stability solutions cannot be obtained analytically. For a fixed top, linear density has been previously shown to decrease growth rates

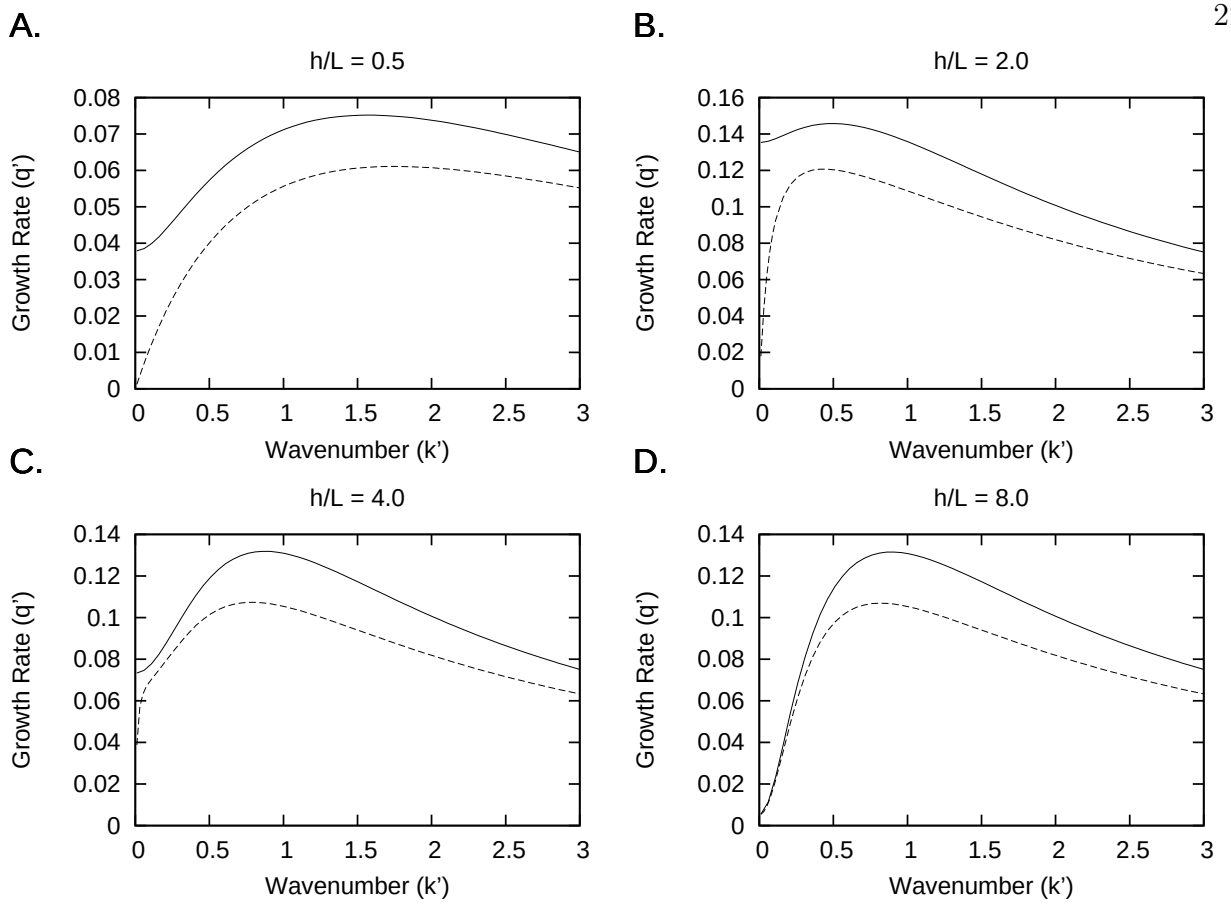

Figure 2.9: Growth rate factor vs. wavenumber from linear stability cases with infinite depth for various h/L values. Solid curves are previous data (Fig. 2.6A) from experiments with exponential viscosity in the substratum. Dashed curves are for constant viscosity in the substratum. A. $h/L = 0.5$ B. $h/L = 2.0$ C. $h/L = 4.0$ D. $h/L = 8.0$

by $\approx 25\%$ (but strongly dependent on h/L) and to shift the maximum growth rate factor to slightly higher wavenumbers (*Conrad and Molnar*, 1997; *Houseman and Molnar*, 1997; *Molnar et al.*, 1998). We examine whether these same effects of linear density apply under a shear-stress free upper boundary condition.

The most striking difference between the cases of linear density and constant density is the smaller growth rate factors for linear density. Comparing these graphs, we observe that q'_{max} for the curve $h/L = 1$ is $\approx 35\%$ of its constant density value. The other q'_{max} values are $\approx 67\%$ of that for constant density for $h/L = 2$ and $\approx 80\%$ for $h/L = 4$ and 8. So, the impact of linear density is much greater when viscosity variation in the layer is low

$(h/L < 2)$.

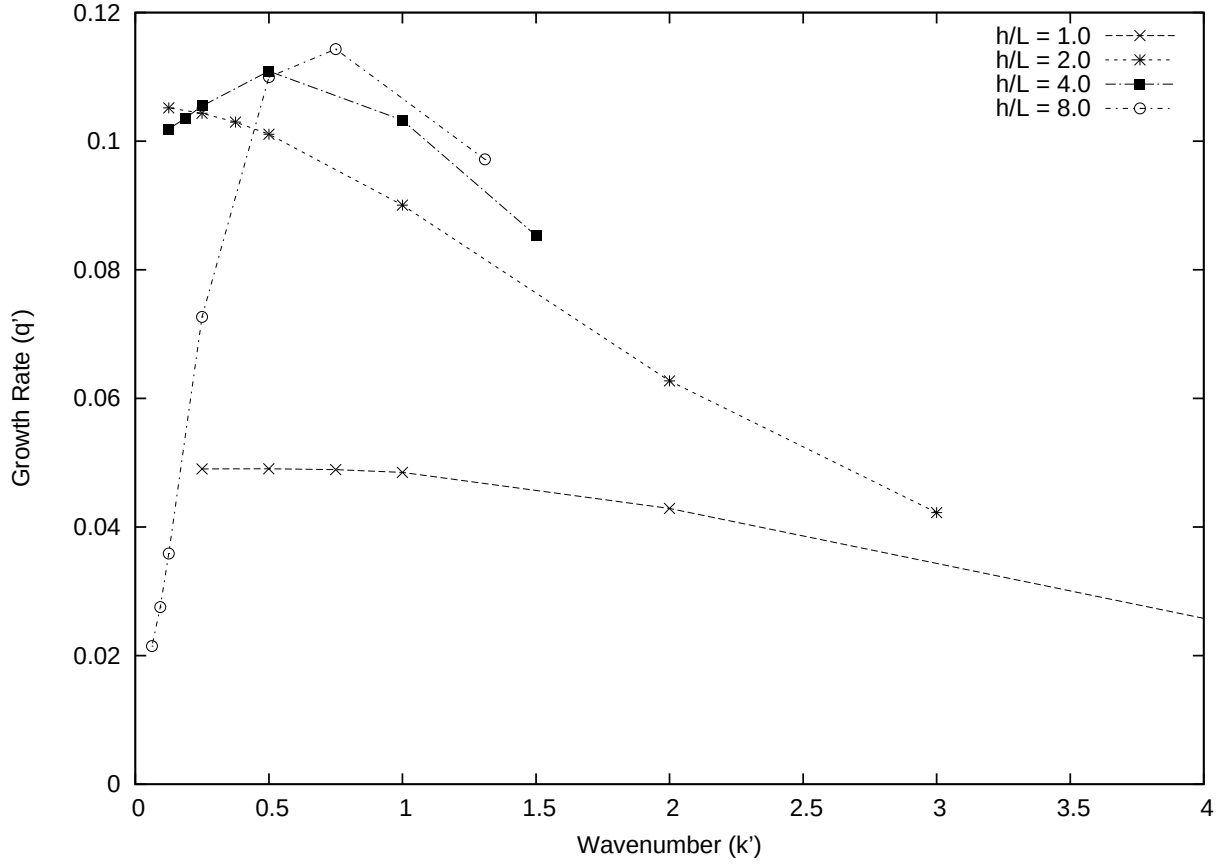

Figure 2.10: Growth rate vs. wavenumber for various values of h/L. Numerical results are shown for experiments with linear varying density, exponential viscosity varying with depth, and a free top boundary condition. These calculations also assume an inviscid constant-density substratum.

Comparing the curves for $h/L = 4$ and 8 in both experiments (Figures 2.5 and 2.10) also shows that linear density shifts the location of q'_{max} to lower wavenumber (longer wavelength). The exact shift (defined as $\Delta k' = (k'_{max\ linear\ density} - k'_{max\ constant\ density})/k'_{max\ constant\ density}$) cannot be found without running calculations at additional k' values, but we estimate $\Delta k' \approx -25\%$. This differs from previous work for a rigid top, as linear density was found to push peak growth rate to higher wavenumber. (*Conrad and Molnar*, 1997; *Molnar et al.*, 1998)

Finally, we notice that for $h/L = 4$, growth rate factors at the longest wavelengths are actually enhanced over their constant density values. Moreover, there is no indication that

$q'_{max} \to 0$ as $k' \to 0$.

2.4.4 Viscous Substratum and Linear Varying Density

Figure 2.11 shows our results for linear density calculations with a viscous substratum, and displays the three main effects described for the inviscid calculations. Compared to constant density, growth rates are reduced overall, with the greatest effect at small h/L values. For $h/L = 8$, q'_{max} is $\approx 85\%$ of the constant density value, and for $h/L = 1$, q'_{max} is $\approx 38\%$ of the constant density value. Second, the location of q'_{max} is shifted to smaller wavenumber by $\Delta k' \approx 25\%$. Finally, the growth rate curves for $h/L = 4$ and 2.5 both show some enhancement at long wavelength. $h/L = 4$ has larger absolute growth rates, and the $h/L = 2.5$ curve shows some flattening at long wavelength.

In these calculations, the viscous substratum exerts the same enhancement of q' at low k' compared with fixed top as for constant density. Although we cannot obtain solutions for linear stability, the numerical results suggest that in the $\lim_{k' \to 0}$, q' will be finite, for a $2 < h/L < 4$.

2.5 Non-Newtonian Exponentially Varying Viscosity with Depth

We perform additional numerical calculations of a layer over an inviscid halfspace using a non-linear viscosity exponent, $n = 3$, in the constitutive equation, Eqn. 3.3. Again, our interest is examining how non-linear viscosity interacts with a shear stress free top boundary to affect the growth rate of the downwelling. We again carried out two sets of experiments, one with constant density in the layer, and another with linearly varying density. As before, each set is performed for various wavenumbers and viscosity scalings. Unfortunately, the non-linear viscosity exponent means that for a scaling of $h/L = 4$ the effective variation of viscosity in the layer becomes $(e^4)^3$. This large variation prevented us from examining larger values of h/L.

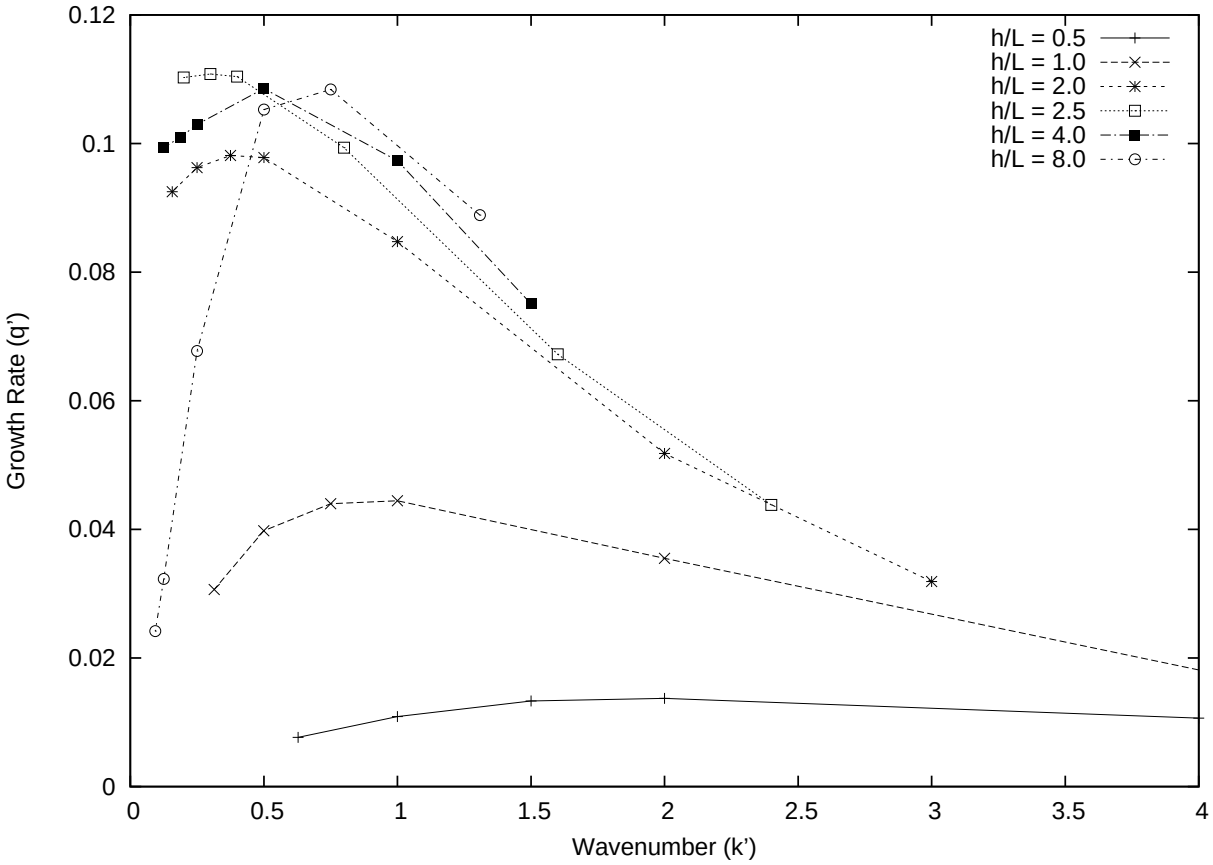

Figure 2.11: Growth rate vs. wavenumber for various values of h/L. Numerical results are shown for experiments with linear varying density, exponential viscosity varying with depth, and a free top boundary condition. These results also have a viscous substratum.

2.5.1 Linearly Varying Density

Our results for linearly varying density with an inviscid substrate are seen in Figure 2.12. Overall, this calculation exhibits some of the same characteristics of similar calculations with Newtonian viscosity (Fig. 2.10). At large wavenumbers ($k' > 2$), growth rates increase monotonically as viscosity variation in the layer increases. These calculations also have smaller ($\approx 50\%$) growth rate factors than their constant density counterparts (not shown), as expected. They also share the finding that q' is finite as $k' \to 0$. What is surprising in these results is that for the for case $h/L = 4$ in Figure 2.12 a local minimum of growth rate factor develops at $k' \approx 0.25$. Further work examining this behavior is forthcoming.

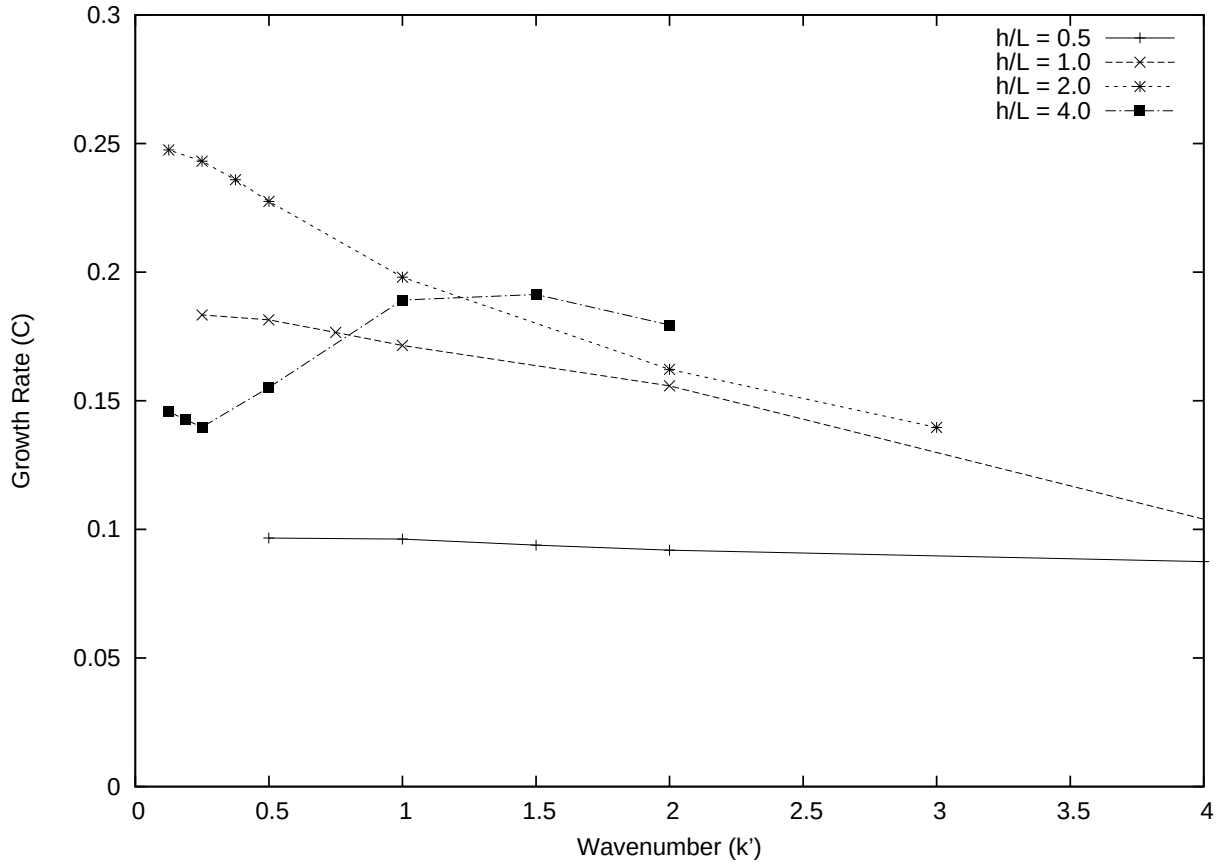

Figure 2.12: Growth Rate vs. wavenumber for cases with non-linear viscosity ($n = 3$) with several h/L viscosity scalings. These calculations have linearly varying density and an inviscid substrate.

2.6 Discussion/Conclusions

The Rayleigh-Taylor calculations show that the overall effect of a shear stress free top boundary condition is to enhance growth rates at long wavelengths, $k' < 0.5$ ($\lambda > 4\pi L$). The degree of enhancement depends also, however, on exponential viscosity variation, linear density variation, and/or the presence of a viscous substratum.

Linearly decreasing density reduces growth rates relative to those for constant density in the layer, as expected. Interestingly, however, linearly decreasing density also enhances long wavelength growth rates for a narrow band of viscosity depth profiles. Specifically, we noticed that when $h/L = 4$, long wavelengths grow faster for linear density than for constant

density (Fig. 2.11). Considering these rheological scalings together, we have retardation that leaves wavenumbers near $k' \approx 0.5$ minimally affected, little decrease in q' at $0.2 < k' < 0.5$, and the shifting of $k'_{q'max}$ toward long wavelengths ($k' \approx 0.5$) as in Figure 2.11, compared to fixed top calculations.

Differences between the free and fixed-top cases vary with h/L and disappear when $h/L > 8$. For instance, for $h/L \approx 2.5$, q'_{max} occurs at wavenumbers of $k'_{free} \approx 0.3$ (Fig. 2.11) and $k'_{fixed} \approx 1.2$ (*Molnar et al.* (1998) Fig. 7) for free and fixed tops, respectively. When $h/L \approx 4$ the difference decreases so that q'_{max} occurs at wavenumbers of $k'_{free} \approx 0.6$ and $k'_{fixed} \approx 0.8$. With a free top, since several growth rate curves flatten for small k' values, but those for the fixed top do not, q'_{max} is less important as it is where q' decreases rapidly with decreasing k', and greater differences between fixed and free tops seem permissible (*Molnar et al.*, 1998).

The implications for the deformation of the mantle lithosphere can be seen in comparison to the Sierra Nevada in California. Two high seismic wave speed anomalies in the mantle underlie the Sierra Nevada. If the two anomalies formed by similar Rayleigh-Taylor processes, they would define a natural wavelength for this mechanism. Before we apply the scaling relations presented above to the Sierra Nevada, let us note that they do not offer unique explanations for the long distance between the Redding and Isabella anomalies, which we presume to mark zones of downwelling in the upper mantle. First, we apply relationships derived for two-dimensional flow to a three-dimensional structure. The locations of the two anomalies at the northern and southern ends of the Sierra Nevada, which itself shows marked east-west variations, implies that the third, east-west dimension could be important. Second, we have assumed that the material is isotropic. Recent work by *Lev and Hager* (2008) shows that anisotropy can affect the wavelength of maximum growth. In particular, resistance to shear on horizontal (or vertical) planes was much less than that on planes dipping at 45°, and the maximum growth rate could increase two to perhaps three times.

As noted, the dimensional wavelength from calculations depends on the choice of h/L,

and we should consider the realistic scaling ratio, h/L, of the Sierra Nevada mantle lithosphere. Using a linear geotherm in the lithosphere,

$$T(z) = T_0 - \beta z, \tag{2.11}$$

(remembering $z = 0$ at the base of the lithosphere) the viscosity can be expressed from olivine laboratory experiments (*Kohlstedt et al.*, 1995) as approximately

$$\eta = \left[\frac{1}{2}A^{-1/n}(\epsilon_{xx})^{1-n/n}exp\left(\frac{E_a}{nRT_0}\right)\right]exp(\gamma z), \tag{2.12}$$

where A is constant and

$$\begin{gathered}\gamma = \frac{E_a\beta}{nRT_0^2} = \frac{E_a}{nRT_0^2}\frac{\Delta T}{h} = \frac{1}{L} \\ \therefore \frac{h}{L} = \frac{E_a\Delta T}{nRT_0^2}\end{gathered} \tag{2.13}$$

(*Conrad and Molnar*, 1997). Parameter descriptions can be found in Table 4.1.

Using reasonable values of activation energy E_a between 400 and 600 kJ/mol K, temperature $1000 < T_0 < 1600$°K ($727 < T_0 < 1327$°C), $370 < \Delta T < 1130$°K , and stress-strain exponent n as 3.5, the ratio h/L for the Sierra Nevada varies from 5 to 9. This places the Sierra Nevada scaling ratio at the upper limit of the range of h/L values from our experiments (*Conrad and Molnar*, 1997; *Kohlstedt et al.*, 1995; *Lachenbruch and Sass*, 1977; *Saltus and Lachenbruch*, 1991).

For example, for $h/L = 6$, and a combined eclogite layer and mantle lithosphere thickness (h) of 200km, would yield a $L \approx 33$km. We remind the reader that although our experiments are 2D plain strain calculations, the Sierra Nevada deformation is certainly 3D, and the effective k' would be a combination of the wavenumbers of disturbances parallel and perpendicular to the range (i.e. $k'_{eff} = \sqrt{k'^2_{\parallel} + k'^2_{\perp}}$) (*Kerr and Lister*, 1988). Thus we can consider as a minimum the Sierra Nevada range parallel natural wavelength, which is approximately 500km. Setting wavelength as $2\pi L/k' = 500km$ implies $k' \approx 0.4$. As noted above, this rapid growth of instability with such a λ seems more permissible with a free top,

because the growth rate factors decrease little for $k' < 0.5$. Thus when viscosity decreases with depth and the top surface of the unstable layer is only weakly constrained longer wavelengths than commonly assumed for Rayleigh-Taylor instabilities should be considered.

2.7 Acknowledgements

This research was supported by the National Science Foundation Grant EAR-0607831. We thank C. Jones and H. Reeg for providing Sierra Nevada tomography results for Fig. 1, and W. Szeliga for helpful discussions. This work benefited from constructive criticisms from two anonymous reviewers.

B	Viscosity coefficient (where constant in the layer)
B_0	Viscosity coefficient at the base of the layer, through which it decreases with depth
β	Geothermal temperature gradient
$\dot{E}$	Second invariant of the strain rate tensor
E_a	Activation energy
g	Gravitational acceleration
h	Thickness of layer
k	Wavenumber of perturbation to the base of the layer
$\Delta k'$	Shift in k'_{max} seen in experiments with linearly varying density
L	Characteristic e-folding depth scale for exponential decrease in viscosity coefficient
p	Pressure
q	Growth rate of Rayleigh-Taylor instability for Newtonian viscosity
R	Gas-law constant
t	Time
T	Temperature
T_0	Temperature at base of layer
ΔT	Temperature difference across layer
u	Horizontal component of velocity
w	Vertical component of velocity
x	Horizontal coordinate
z	Vertical coordinate
$\Delta\rho$	Density difference between the layer and the underlying half-space or subspace
σ_{ij}	Stress component
τ_{ij}	Deviatoric stress component

Table 2.1: Definition of symbols.

Chapter 3

Lithospheric thinning and localization of deformation during Rayleigh–Taylor instability with non-linear rheology and implications for intracontinental magmatism

3.1 Abstract

Thinning of mantle lithosphere due to Rayleigh–Taylor instability can be a mechanism for triggering continental magmatism near active or recently active plate boundaries. We consider whether it is also plausible as a mechanism for intracontinental magmatism, several hundred kilometers from active subduction or rifting. We perform 2D Rayleigh–Taylor experiments and find that a shear-stress free top and non-Newtonian flow permit two types of instability to develop, largely dependent on how the viscosity coefficient varies with depth. For small variation with depth, with the e-folding depth scale (the interval across which the coefficient changes by a factor of e) greater than a third to a half of the thickness of the unstable layer, deformation concentrates at the ends of the layer in localized thinning and thickening zones; the middle part moves horizontally towards the region of thickening as a coherent block undergoing minimal strain. When the viscosity coefficient decreases more rapidly with depth, thinning of the layer is distributed laterally over a wide zone. Between the regions of thickening and thinning, shear strain and vertical gradients in horizontal velocity prevent this area from moving as a coherent block. The rheological exponent, n, that relates strain rate to stress in the constitutive equation controls the degree of localization of the downwelling and upwelling: the width varies as $\approx n^{-1/2}$. In intra-plate settings where

a shear-stress free top condition could be applicable, high-stress crystalline plasticity could provide a mechanism for the narrow zones of thinning and upwelling, which would facilitate decompression related volcanism.

3.2 Introduction

Continental magmatism is a common occurrence in tectonically active regions of subduction or rifting. Subduction zone arc magmatism is produced mainly through chemical interaction between the subducted crust and mantle material (e.g. *Kay*, 1980; *Morris et al.*, 1990). Rifting, on the other hand, thins lithosphere to allow the underlying asthenosphere to melt through adiabatic decompression as it rises (e.g. *McKenzie and Bickle*, 1988). How then do we explain continental magmatism, that occurs several hundred kilometers from plate boundaries (e.g., northern Tibetan plateau, the North China Craton), in the absence of these tectonic processes? Barring heat sources from below, produced perhaps by mantle plumes, or the introduction of a chemical process, we are left to explore another way to thin lithosphere and generate melt (e.g. *Elkins-Tanton*, 2005).

Dynamic, ductile removal of lower lithosphere is one possibility that creates the accommodation space required for the rise of material, and hence either decompression melting or melting from conductive heating of shallower lithosphere. With plausible conditions, the Rayleigh-Taylor instability of the mantle lithosphere when perturbed enough can thin the lithosphere to a significant degree (by tens of percent) to overcome stabilization by thermal diffusion (e.g. *Conrad and Molnar*, 1997; *Gemmer and Houseman*, 2007; *Hoogenboom and Houseman*, 2006; *Molnar et al.*, 1998; *Molnar and Houseman*, 2004). Additionally, if part of the crust has been transformed into eclogite, its density (e.g. *Jull and Keleman*, 2001; *Kay and Kay*, 1993) and low viscosity (*Austrheim*, 1991) allow it to participate in the downwelling/removal of mantle lithosphere (e.g. *Farmer et al.*, 2002). The inclusion of eclogite in a Rayleigh-Taylor process would also contribute to the effective thickness of the unstable layer, which affects the lateral extent of eventual thinning. For instance, the Sierra Nevada

shows evidence of removal of a $40-60$ km thick eclogitic layer in addition to the underlying mantle lithosphere (*Ducea and Saleeby*, 1996). *Jull and Keleman* (2001) found a variety of lower crustal compositions that can develop instabilities in layers only ten kilometers thick on relevant timescales.

With Rayleigh-Taylor instabilities, removed lower lithosphere is replaced with less dense asthenosphere, and the effects of this process are seen with a variety of observations. Geomorphic observations such as regional surface uplift and/or tilting (e.g. *Stock et al.*, 2004; *Unruh*, 1991), seismic observations including low seismic wave speeds (e.g. *Jones et al.*, 1994; *Reeg et al.*, 2007), and geochemically, the appearance of high-potassium magmas can all result from thinned lithosphere (*Farmer et al.*, 2002; *Hoernle et al.*, 2006; *Kay and Kay*, 1993; *Turner et al.*, 1996). Perhaps because of the difficulty of inferring the previous state of the lithosphere through time, these instabilities commonly have been suggested to apply to regions of recent tectonic activity ($< 10Myr$) such as the Sierra Nevada in California (e.g. *Ducea and Saleeby*, 1996; *Lee et al.*, 2001; *Jones et al.*, 2004), sections of the Andes (e.g. *Kay and Kay*, 1993), New Zealand (e.g. *Stern et al.*, 2000, 2006), and the Southeast Carpathians in the Vrancea region (e.g. *Knapp et al.*, 2005).

In each of these locations, the inferred downwelling zone must be compensated by an adjacent zone of lithospheric thinning; for instance the Vrancea downwelling is accompanied by thinning of the mantle lithosphere beneath the Transylvanian basin (*Lorinczi and Houseman*, 2009). Often, in the absence of evidence indicating the location of downwelling flow, removed lithosphere is assumed to have sunk immediately below regions of thin lithosphere. Another characteristic of these regions of thin lithosphere is that they share a regional length scale. The lateral extent of such regions often covers at least 100 km, sufficient for resolution by key observation techniques such as travel time tomography, where densely spaced seismic networks have been deployed (e.g. *Reeg et al.*, 2007).

In many regions that have been affected by previous, subducted slab-related metasomatism, removal of mantle lithosphere has been accompanied by potassic magmatism. Al-

though it is possible for magma to be generated from the sinking of detached, downwelling mantle lithosphere (*Elkins-Tanton*, 2005, 2007), high-potassium instability-generated melts have been more commonly ascribed to thinning of lithosphere (*Elkins-Tanton and Grove*, 2003; *Farmer et al.*, 2002; *Hoernle et al.*, 2006; *Kay and Kay*, 1993; *Lee et al.*, 2001; *Manley et al.*, 2000; *Turner et al.*, 1996). Not all continental potassic magmatism is related to lithosphere instabilities, however (e.g. *Farmer et al.*, 2008), and it is unknown whether potassium and hydroxyl-rich (water rich) zones in the mantle can contribute to conditions needed for lithospheric removal. Still, at present the localization of high-potassium magmas seems the best indicator for lithospheric instabilities that occur on short length scales, or for those that occurred sufficiently far into the past that other indicators may have been lost. Building on earlier work, we investigate how this signature magmatism could be related to the localized thinning of the lithosphere.

Houseman and Molnar (1997) found, using numerical experiments of Rayleigh-Taylor instability of a layer with stress-dependent viscosity and a rigid upper surface, that for long perturbation wavelengths, deformation was more localized above upwelling/downwellings than for shorter wavelengths, or for cases with Newtonian viscosity. In general the wavelength of maximum growth rate is about three times the unstable layer thickness. Thus it would seem that lithospheric thinning need not occur immediately adjacent to downwelling, but could be displaced a distance several times the thickness of the unstable layer. When wavelength is increased for a shear-stress free upper boundary, the wide separation of the upwelling zone from the downwelling implies that thinning of lithosphere, and related magmatism, could occur in narrow groupings hundred of kilometers from the downwelling perhaps in the absence of upper crustal deformation. In some cases, this could be several hundred kilometers from previous zones of subduction and might be described as intra-plate volcanism.

In several continental regions with potassic magmatism hundreds of kilometers from plate boundaries, the link to a tectonic or dynamic mechanism is not obvious. In Tibet,

most of the late Cenozoic potassic volcanism centers lie in the northern parts of the plateau, hundreds of kilometers from the locus of convergence in the Himalaya to the south (*Turner et al.*, 1996). In the eastern Anatolian region of Turkey, the most potassic volcanism is found in the north (in the Erzurum-Kars Plateau region) since ≈ 11 Ma, several hundred kilometers from the site of subduction in the south where Eurasia and Arabia collided (*Keskin*, 2003; *Keskin et al.*, 1998; *Pearce et al.*, 1990). In northeast China lower lithosphere is thought to have been removed beneath the middle of the otherwise undeformed North China Craton, with volcanism spiking around 120 Ma (*Gao et al.*, 2008).

To evaluate the rheological conditions under which a Rayleigh-Taylor instability develops into this alternate style of downwelling with remote thinning of the unstable layer, we use 2D plane-strain numerical calculations of the instability of a dense layer overlying a less dense half-space, subject to an initial harmonic perturbation on its lower boundary. We use a shear stress-free top boundary condition on the layer and examine spatially variable rheological properties. Calculations are carried out until the vertical displacement of the lower surface at least approaches initial layer thickness. If indeed the conditions for this type of instability occur on the Earth, it could indicate a mechanism for volcanism several hundred kilometers from active or previously active plate boundaries.

3.3 Basic Theory of Rayleigh–Taylor instability and Small Slope Approximation

Linearized theory is a common approach used to examine the growth of Rayleigh-Taylor instabilities (e.g. *Conrad and Molnar*, 1997; *Chandrasekhar*, 1961). The approximations used must, of course, eventually fail as perturbations grow to large amplitudes and non-linear terms in the governing equations become large, but the methods capture the initial growth of the instability, provide simplicity to a complex process, and can guide the development of scaling relationships. *Canright and Morris* (1993) developed small slope solutions for the growth of instabilities in a layer with constant rheological properties bounded by shear

stress-free surfaces on the top and bottom of the unstable layer. Using an approach that explicitly includes the non-linear interactions, they were able to describe unstable behavior at amplitudes larger than is possible with the linear approximation. They show the narrowing of deformation zones, and hence the separation of downwelling and upwelling, with increasing stress-strain exponent, n, (see appendix in *Canright and Morris* (1993)). We investigate this behavior further with numerical experiments, but we first examine the limits of the small slope theory.

Canright and Morris (1993) examined three types of initial conditions, but the most appropriate for comparison with our experiments is a constant wavelength sinusoidal perturbation (wavelength λ) to the thickness of the unstable layer. Their solution for the change in layer thickness (δ) with time (t) for non-Newtonian viscosity obeys the following equation:

$$\frac{D\delta}{Dt} = sgn(\delta - d_e(t))\delta \left[\frac{|\delta^2 - d_e^2(t)|}{\delta}\right]^n \tag{3.1}$$

with

$$d_e^2(t) = \frac{\int_0^\lambda \delta\, dx}{\int_0^\lambda 1/\delta\, dx} \quad \text{and} \quad \frac{D\delta}{Dt} = \frac{\partial\delta}{\partial t} + u\frac{\partial\delta}{\partial x} \tag{3.2}$$

where δ is the thickness of the unstable layer and u is the horizontal component of velocity. When we consider the maximum and minimum thickness of the layer, u is zero, so at these positions $D\delta/Dt$ is just the change of thickness with time. *Canright and Morris* (1993) non-dimensionalize quantities by the time scale $\left(\frac{4B}{\Delta\rho g h}\right)^n$ and length scale by h, the initial thickness of the unstable layer. Here, $\Delta\rho$ is the density difference between the layer and lower half-space, and g is gravitational acceleration. B, the viscosity coefficient of the layer (when constant), and n, the rheological exponent are part of the non-linear constitutive relation between deviatoric stress, τ_{ij}, and strain rate, $\dot{\epsilon}_{ij}$, defined in our layer:

$$\tau_{ij} = B_o exp(z/L)\dot{E}^{(1/n-1)}\dot{\epsilon}_{ij}. \tag{3.3}$$

This form includes an exponential depth-dependence of viscosity that we use later, with B_o as the viscosity coefficient at the lower surface, z as the vertical coordinate, set to zero at

the bottom of the layer and increasing upward, and L as the e-folding depth scale for the exponential decrease (the depth interval across which the viscosity changes by a factor of e). Our analysis below depends on the dimensionless viscosity stratification ratio, h/L, which can be easily calculated for an olivine rheology (*Conrad and Molnar*, 1997). Estimates of this ratio for conditions in the Sierra Nevada vary between 5 and 9 (*Harig et al.*, 2008). $\dot{E} = \sqrt{\sum_{i,j} \dot{\epsilon}_{ij}\dot{\epsilon}_{ij}}$ is the second invariant of the strain-rate tensor. This definition follows the convention of *Houseman and Molnar* (1997) and affects the definition of B values.

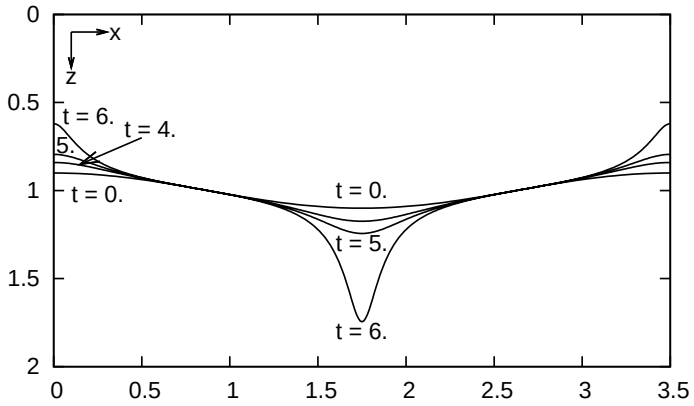

Figure 3.1: Boundary deflection profiles calculated as in *Canright and Morris* (1993) Appendix B. Here a constant density fluid of thickness 1, with power-law exponent of $n = 3$ is perturbed sinusoidally with amplitude 0.1. Dimensionless times $t = 0$, 4, 5, 6 shown. The solution derived by *Canright and Morris* (1993) is independent of the perturbation wavelength.

We present results in an alternative non-dimensionalization, defined by the time scale $\left(\frac{B_e}{\Delta\rho g h}\right)^n$ from Figure 3.2 onward to conform to earlier work (e.g. *Molnar et al.*, 1998). *Canright and Morris* (1993) calculated boundary deformation through time (Figure 3.1), ensuring volume is conserved

$$\int_0^\lambda \left[\frac{\delta^2 - d_e^2(t)}{\delta}\right]^n dx = 0. \tag{3.4}$$

We first validate the approximate theory by using the boundary deformation from our numerical experiments to calculate, using equation 3.1, $D\delta/Dt$ where the downwelling is

maximum at different stages of growth. When we compare these rates to the numerically calculated downward component of dimensionless velocity, w' (Figure 3.2), we notice that the rate of downwelling predicted by the analytical approximation is systematically greater than that produced by the numerical calculation and the difference increases as the instability grows. Alternatively, we can compare the peak deflection vs. time for the two methods by numerical integration of $D\delta/Dt$. Following *Houseman and Molnar* (1997), we compare the growth rates by fitting lines of the form

$$Z'^{(1-n)} = (n-1)\left(\frac{C}{n}\right)^n (t'_b - t') \tag{3.5}$$

where the singular time t'_b represents the time when the downwelling reaches infinite depth (Figure 3.3). This form is derived from simple assumptions including an approximation to the non-linear constitutive relation and that the stresses driving the instability are proportional to its interface deflection (*Houseman and Molnar*, 1997). Here we see that the line fitting $Z'^{(1-n)}$ vs. t' will give C from the slope and t'_b from the time intercept. The small slope approximation and numerical calculation appear to show initial agreement, but with different growth rates C, and correspondingly different estimates of the singular time t'_b.

Inherent in Canright and Morris's derivation is the assumption of small slopes of the boundaries. While the slopes remain small, the layer has a large horizontal length scale compared to its vertical thickness. Away from the ends, horizontal components of velocity dwarf vertical components, and it is assumed these components of velocity are independent of the vertical coordinate. Their analysis ignores shear stress on horizontal planes, τ_{xz}. These assumptions start to fail as amplitudes of deformation become large (in this example, on the order of 10% thickness change), and this failure is likely the main reason for the small divergence between our numerical calculations and their approximate theory. In detail Canright and Morris's analysis is imperfect, but it provides a sensible qualitative image of the process and guides our work below.

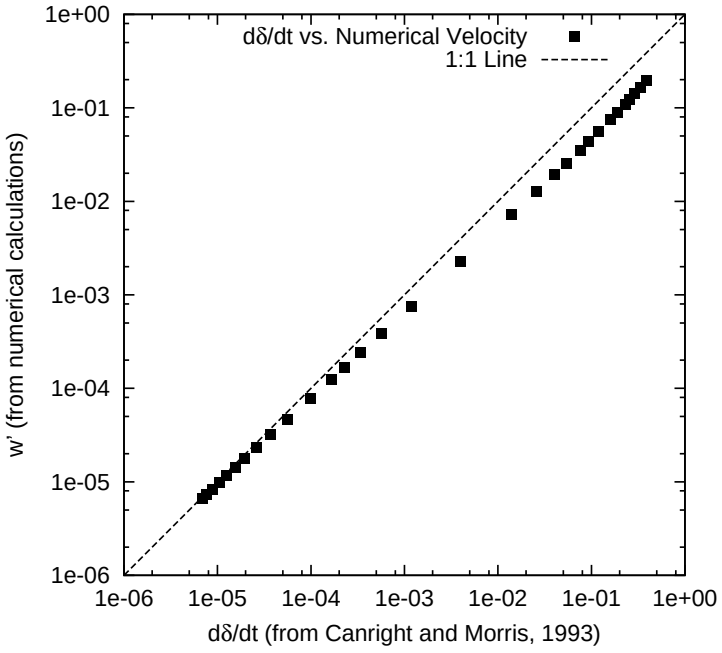

Figure 3.2: log[Dδ/Dt] from Equation 3.1 with δ obtained from finite element solution vs. log[downward component of velocity] from numerical calculations. A 1:1 line is also shown. Cases here use $\lambda/h = 4\pi$.

3.4 Depth varying rheological properties

3.4.1 Constant Density

To complement the small amplitude analysis, we perform 2D plane strain numerical Rayleigh-Taylor instability experiments with depth varying viscosity and categorize the instabilities according to the observed end states. Like *Houseman and Molnar* (1997), we use the finite element program Basil and begin with layers of constant density. We vary the depth-dependence of viscosity and the rheological exponent of the layer. Layer thicknesses are perturbed with a dimensionless wavelength of $\lambda' = \lambda/h = 4\pi$, with amplitude $0.03h$ or $0.04h$, chosen because there is qualitatively little difference in results once wavelength is sufficiently long ($\lambda' > 2\pi$). Our calculations do not include the energy equation, but previous experiments on convective instability including diffusion of heat (*Conrad and Molnar*, 1999),

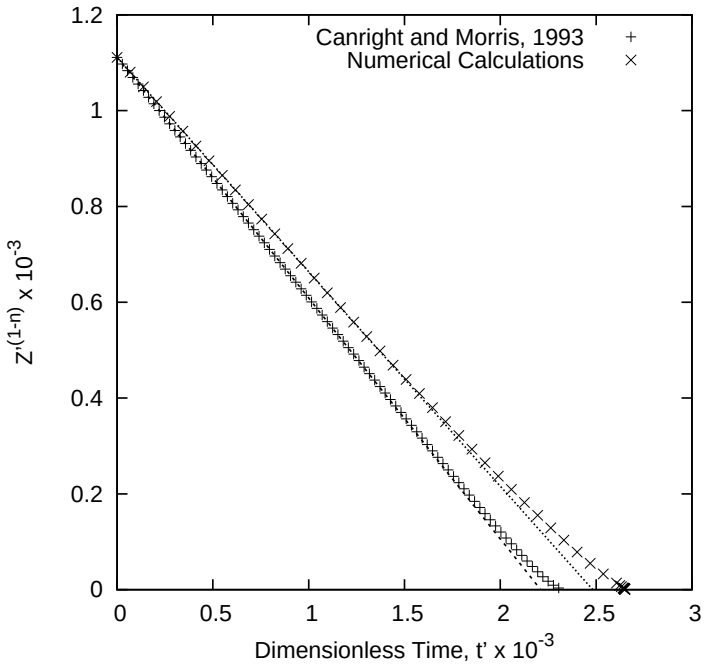

Figure 3.3: $Z'^{(1-n)}$ vs. dimensionless time for the example where $n = 3$. Lines of the form in equation 3.5 are fit to the initial small amplitude deformation portion of the data. The numerical case here uses $\lambda/h = 4\pi$.

confirm the scaling laws of *Houseman and Molnar* (1997).

Holding wavelength constant, instabilities fall within 3 groupings based mainly on the ratio of layer thickness to viscosity length scale, h/L (Figure 3.4). When $h/L \leq 2$, instabilities develop with zones of downwelling and upwelling separated by a broad region where vertical components of velocity are negligible. Within this central region horizontal velocity, U_x, is nearly constant in both x and z directions throughout the run. The entire central region moves as a coherent block towards the downwelling region. Also, as the calculation time nears t_b, maximum vertical deflection and velocity of the downwelling and upwelling are of comparable magnitude.

When $h/L \geq 4$, the large viscosity contrast between the top and bottom of the layer enables deformation to concentrate near the bottom part of the layer and the horizontal

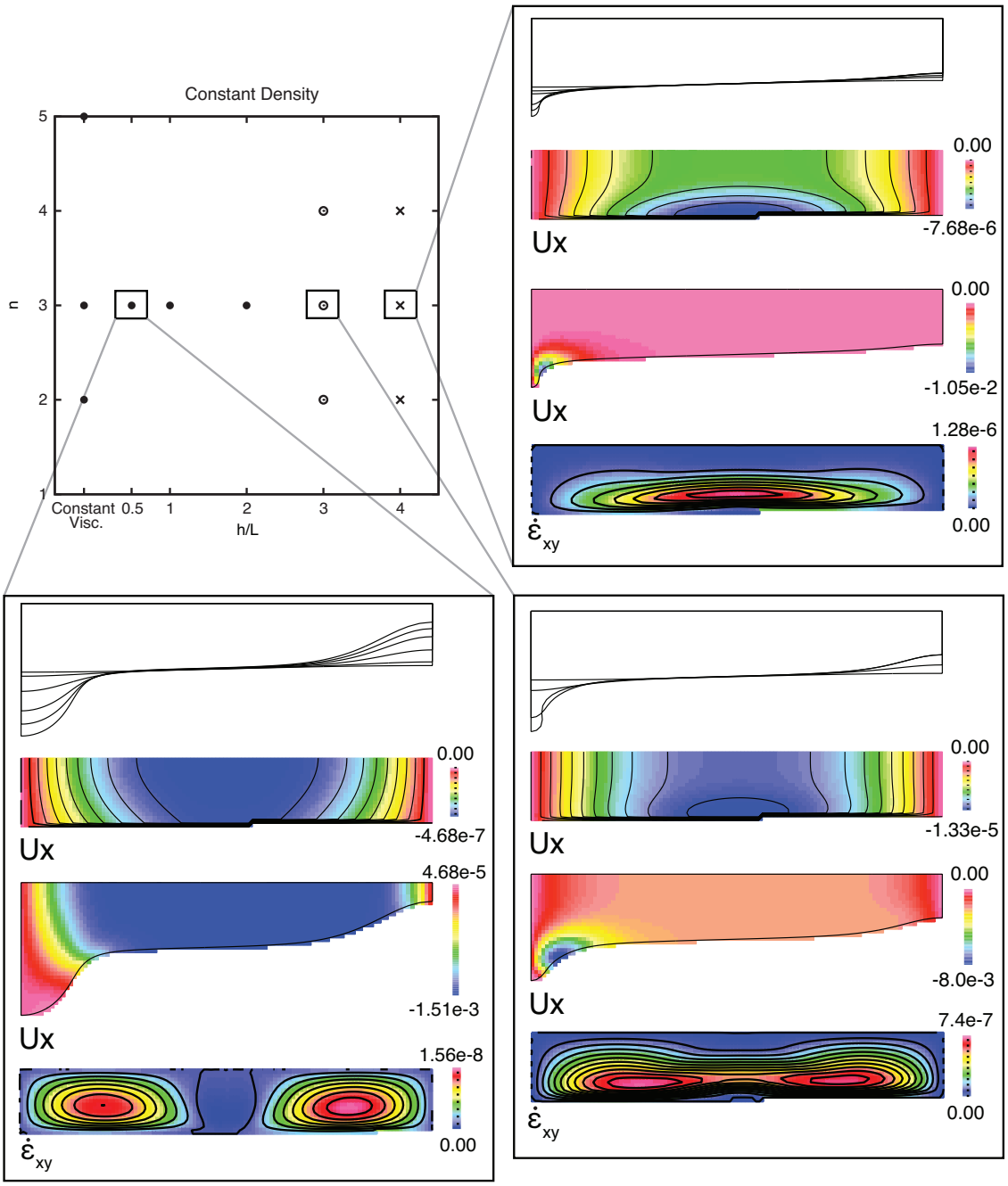

Figure 3.4: Phase diagram for experiments with constant density showing the division of instabilities based on their end state deformation. Instabilities divide into categories depending on viscosity stratification ratio h/L and stress-strain exponent n. In each case, $\lambda/h = 4\pi$. Closed circles are calculations in which center region develops uniform horizontal velocity. X's are calculations that develop significant shear deformation in the lower part of the layer and more distributed thinning. Open circles are transitional cases. One calculation from each group has additional detail showing different aspects of deformation. The first (top) detail shows boundary deformation through time while the second and third details are colored contours of horizontal velocity at the initial and later states. Negative values of horizontal velocity show motion to the left, toward the downwelling. Finally, $\dot{\epsilon}_{xy}$ is shown, indicating whether the dominant initial deformation is horizontal shear near the base of the layer or vertical shear at the ends of the calculation.

component of velocity near the top is minimized. Thus, significant vertical gradients of horizontal velocity now exist within the central region, and shear-strain occurs on horizontal planes in the lower part of the layer. It should be clear that in this case the approximation of negligible shear-stress on these planes, made by *Canright and Morris* (1993) for a layer with constant viscosity, is no longer valid. Furthermore the rates of vertical displacement differ greatly for thickening (downwelling) and thinning (upwelling); these rates differ at short times into the calculation and by increasing amounts as the duration of the calculation approaches the time t'_b. As h/L increases we see that the maximum thinning factor achieved is decreased as extension is distributed over a broader area of the lower lithosphere.

The impact of h/L on vertical gradients of horizontal velocity is easily seen in the examples shown in Figure 3.4. The end member groupings show significantly different shear strain-rate fields, which are indicative of their different later deformation patterns. For the calculation with $h/L = 4$, denoted with an X, we see the shear strain-rate field contains vertically stratified positive values, indicating the field is dominated by $\partial u/\partial z$ as the lower part of the layer moves toward the downwelling. Conversely the case with $h/L = 0.5$ (solid circle) has two separated areas of positive values at the ends of the calculation. Here, $\partial u/\partial z$ is modest and the shear strain-rate maxima are likely a result of positive values of $\partial w/\partial x$ corresponding to the downwelling at one end and the upwelling at the other. These two end-member groups merge in a transition region (Figure 3.4, open circle) where one sees both concentrations of shear strain-rate at the ends of the layer and a vertical gradient of strain-rate in the center region.

3.4.2 Linearly Varying Density with Depth

We also perform experiments with density varying linearly as a function of depth from zero at the base of the layer to two at the top. As before, instabilities grow into different end states depending mainly on the viscosity stratification ratio, h/L (Figure 3.5). The most noticeable difference for linearly varying density is the shift of the transition region from

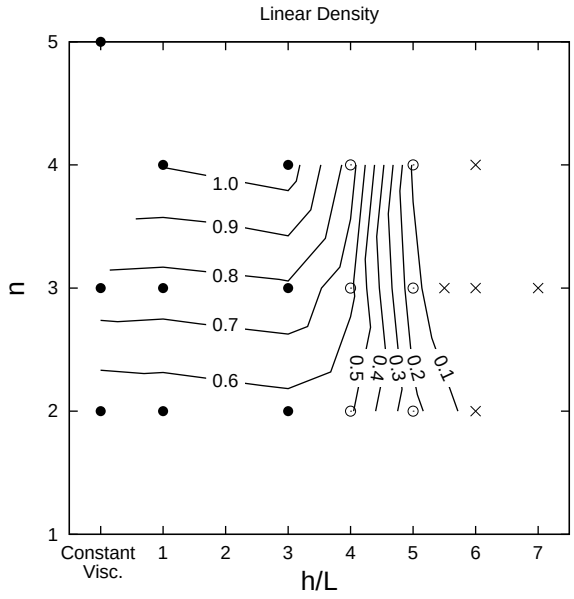

Figure 3.5: Phase diagram for experiments with linearly varying density ($\lambda/h = 4\pi$) showing the division of instabilities into categories depending on viscosity scaling h/L and stress-strain exponent n. Symbols are the same as Figure 3.4. Here we also plot contours of the absolute value of the ratio of upwelling speed to downwelling speed for the time when the downwelling zone has thickened by 40% (to 140% of original thickness).

$2 < h/L < 4$ in constant density to $3 < h/L < 6$ with linearly decreasing density anomaly. Of course, this assessment of the width of the transition zone, based on the horizontal speed, is subjective. As a more objective measure we calculate the absolute value of the ratio of maximum upwelling speed to maximum downwelling speed at a time when the downwelling zone has thickened by 40% (or is 140% of original thickness). The contours in Figure 3.5 allow a more precise definition of the transition zone limited by vertical contours at large h/L and horizontal contours at small h/L. The contours also roughly indicate the maximum thinning we should expect; ratios near one indicate the layer approaches the upper limit of thinning to zero thickness.

We note that h/L and n have different effects on the final deformation of the layer, with the rheological exponent controlling the final large amplitude super-exponential growth. If two cases have similar velocity ratios, a lower n means the final stages of drip formation

will be less abrupt and the layer can continue to thin. Alternatively, when a case with large n reaches t_b the downwelling will develop much faster than further thinning.

For example cases with $n = 2$, and $h/L = 6$ or 3 we examine the growth of the upwelling and downwelling (Figure 3.6) to see where they diverge. When the upwelling is localized (Fig. 3.6A), the maximum upwelling and downwelling deflections are well approximated with the $Z'^{(1-n)}$ fits even as they approach the singular time t'_b. When thinning is distributed over a wider region (Fig. 3.6B) the downwelling deflection deviates from its best fit and approaches the time t'_b much sooner than estimated from the fit. The upwelling deflection, however, continues to follow the power-law growth trend established early in the calculation.

3.4.3 Variation with Stress Exponent, n, and Viscosity scaling, h/L

To evaluate the effects of different exponents in the constitutive relationship, n, we examine cases with constant viscosity coefficient ($L \to \infty$) for which separated upwellings and downwellings occur. Although initially perturbed with a harmonic variation in the thickness of the unstable layer, these cases quickly transition to localized thinning and downwellings. As *Canright and Morris* (1993) found, once λ' is large enough, the form of deformation should vary with wavelength only as a simple scaling (or stretching). The cases examined here were perturbed with $\lambda' = 4\pi$, which should be considered for dimensionalization. To quantify the transition to localized deformation we examine the half-width of the upwelling zone, which we define as the position of the local maximum of the slope of the base of the layer (Figure 3.7). These positions are calculated for each time step using the first order finite difference between the lower surface nodes, but are plotted versus vertical displacement at the center of the upwelling (as opposed to vs. time) since each experiment uses a different timescale. With increasing n, the width of the upwelling zone decreases, further localizing deformation, as predicted by *Canright and Morris* (1993). The steps in the horizontal positions in Figure 3.7 can be attributed, we believe, to times when maximum slope moves from one boundary node to another.

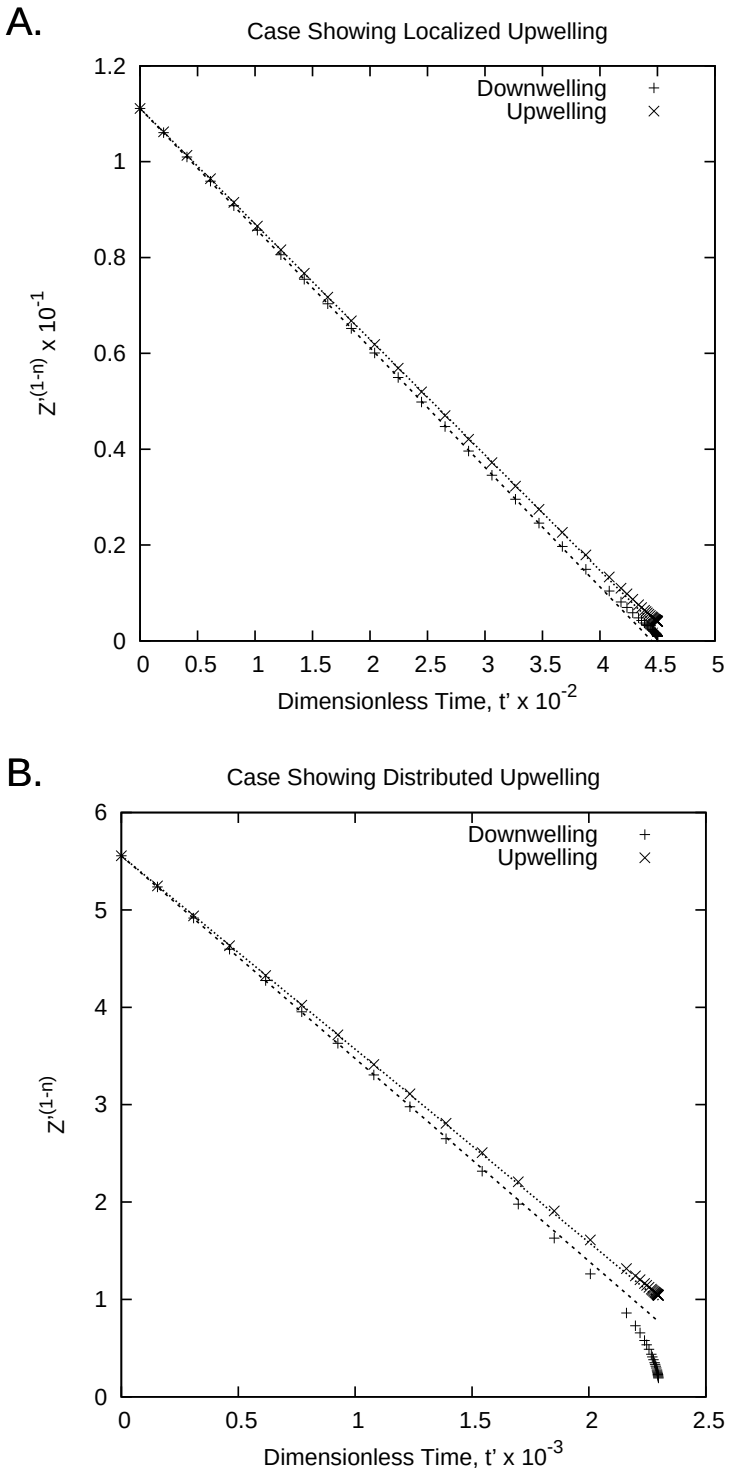

Figure 3.6: $Z'^{(1-n)}$ vs. t' for both upwellings and downwellings for cases with $\lambda/h = 4\pi$, $n = 2$, and density decreasing linearly with depth. A. shows a case with localized upwelling, with $h/L = 3$ and B. shows a case with $h/L = 6$ and distributed upwelling. Best fit lines are drawn from Equation 3.5.

England et al. (1985) examined the length scales of continental deformation for different plate boundary settings. With some simplification, they solved for the velocity field in a thin viscous sheet perpendicular to a convergent or divergent margin. They found that this component of velocity decreases with distance from the margin as $e^{-\sqrt{n}\pi y/\lambda}$. In this case, λ was the wavelength of their boundary perturbation. Our 2D calculation, with a center region that moves uniformly away from the upwelling boundary, is similar in setting to the convergent/divergent boundary considered by *England et al.* (1985). The main difference here is that the velocity parallel to the vertical symmetry plane is not zero.

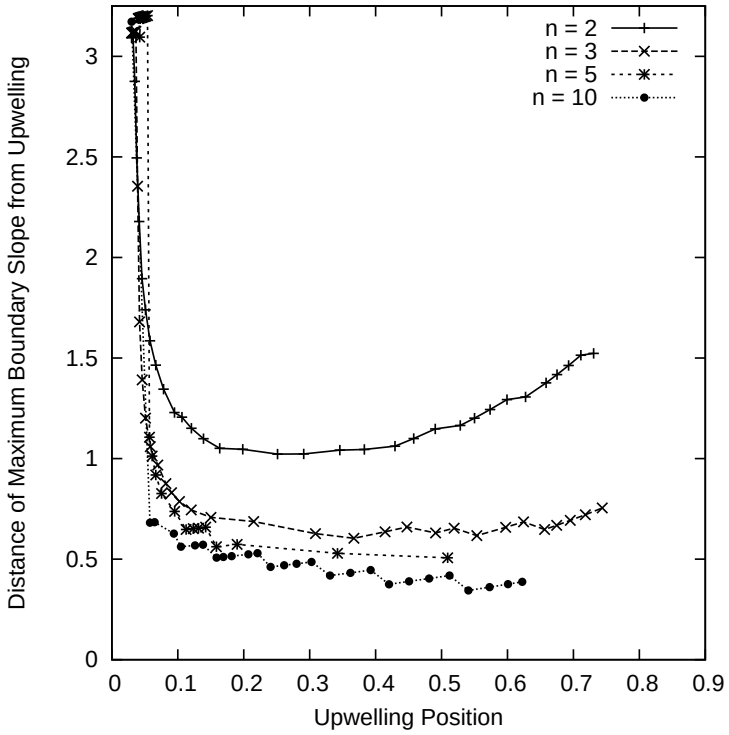

Figure 3.7: A comparison of the horizontal position of the local maximum in lower boundary slope for the upwelling plotted against maximum vertical upwelling position, as each instability develops. Vertical position can be considered a proxy of the timescale across experiments because the vertical position increases monotonically with each calculation step. Each case has constant viscosity coefficient and constant density in the layer, with $\lambda/h = 4\pi$. The local maximum in lower boundary slope initially begins at π due to the imposed perturbation and quickly becomes more localized at the upwelling zone.

We estimate where each upwelling width stabilizes in Figure 3.7, noting the variability

or uncertainty in our estimate, and plot them versus rheological exponent in Figure 3.8. The width of the upwelling zone roughly follows the relation

$$\text{width} \approx 1.25 n^{-1/2}, \tag{3.6}$$

scaled by the perturbation wavelength.

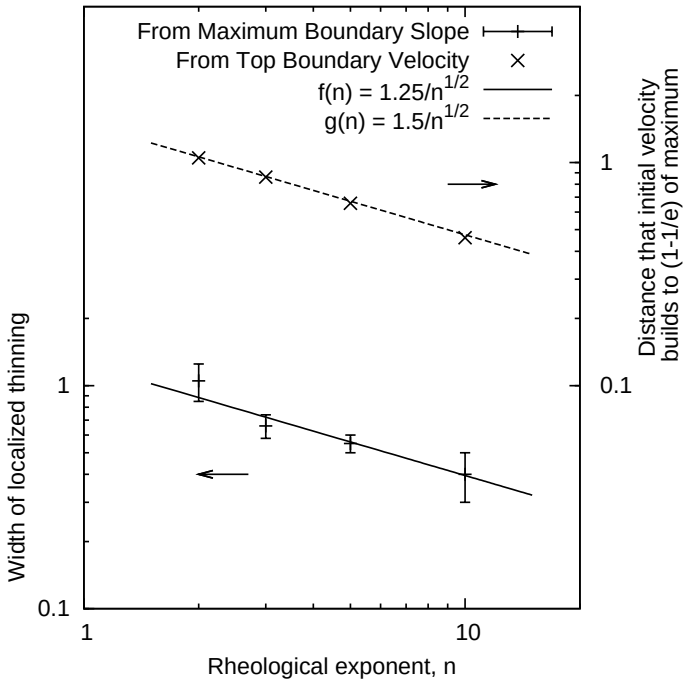

Figure 3.8: Estimates of the width of the localized upwelling region vs. rheological exponent n, estimated from the maximum slope of the bottom boundary (lower line, left hand scale). Widths and uncertainties are estimated from Figure 3.7. In the upper part of the graph we plot the distance over which horizontal velocity on the top boundary decays away from the symmetry plane vs. rheological exponent n. These data use the right hand y-axis.

We also examine the velocity profile, u, along the top shear stress free surface at the initial time step. We find that, although it is not a simple exponential function, the distance required for the maximum horizontal velocity to build to $(1 - 1/e)$ of the maximum very closely follows the relation $\approx 1.5 * n^{-1/2}$ (also Figure 3.8). It seems that although our calculations include greater complexity than those of *England et al.* (1985), the underlying dependence on the square root of the rheological exponent, n, still applies when the medium

adequately approximates a half-space perpendicular to the symmetry plane (in our case when $\lambda > \pi$).

Variation of the width of the upwelling with viscosity stratification ratio, h/L, is examined in Figure 3.9. Here the rheological exponent $n = 3$ for each case. The width of the upwelling region shows little dependence on h/L except when $h/L \geq 4$ (when broad distributed thinning occurs). Since we might expect h/L values for lower lithosphere to vary between 5 and 9, this shows that when the high-temperature stress-strain exponent of $n = 3.5$ for olivine is used for the entire lithosphere, localized thinning would be unlikely.

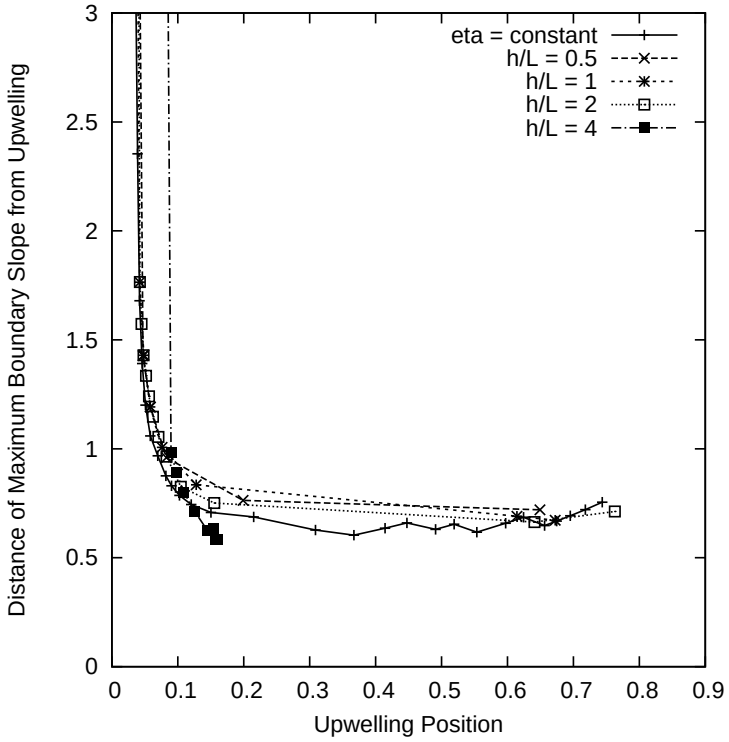

Figure 3.9: We plot, as in Figure 3.7 the upwelling zone width versus upwelling deformation for cases with $n = 3$. Each case has constant viscosity coefficient and constant density in the layer, with $\lambda/h = 4\pi$. Those cases that develop with separated upwellings and downwellings, $h/L < 4$, show little variation with length scale of viscosity variation. The case of $h/L = 4$ does not develop with separated upwellings and downwellings, and upwelling deformation remains minimal compared to downwelling deformation (54% of layer thickness in this case).

3.5 Discussion

3.5.1 Large Scale Lower Lithosphere Removal

The zone of plate-like deformation occurs when $h/L < 3$ and is below the range of values we might expect in typical lower lithosphere, which can range from roughly 5 to 9 (*Harig et al.*, 2008). The h/L ratio of the power law rheology of olivine is determined approximately as

$$\frac{h}{L} = \frac{E_a \Delta T}{nRT_0^2} \tag{3.7}$$

where E_a is activation energy which can vary between 430 and 540 kJ/mol (*Karato and Wu*, 1993), ΔT is the temperature variation across the layer, n is the stress-strain constitutive exponent often fixed at 3.5 (based on creep measurements of dry olivine), R is the gas constant (8.314472 J K^{-1} mol^{-1}), and T_0 is the temperature at the base of the layer (*Harig et al.*, 2008). With this rheology, $h/L < 3$ requires either unreasonably warm Moho ($T \approx 900°C$ for a mantle potential temperature of $T_0 = 1300°C$, $\Delta T = 400°C$) or a transition to the low-temperature high-stress creep regime which results in a greater effective value of n (*Evans and Goetze*, 1979; *Goetze*, 1978).

At high stresses the power law constitutive equation for olivine breaks down to an exponential relation between stress difference and strain rate experimentally given by *Goetze* (1978) and *Evans and Goetze* (1979) as

$$\dot{\epsilon}_{11} = \dot{\epsilon}_0 exp\left[-\frac{H_a}{RT}\left(1 - \frac{\sigma_{11} - \sigma_{33}}{\sigma_0}\right)^2\right]. \tag{3.8}$$

Here $\dot{\epsilon}_{11}$ is the longitudinal strain in a uni-axial strain rate experiment, and $\sigma_{11} - \sigma_{33}$ is the difference between longitudinal compressive stress and confining pressure. *Molnar and Jones* (2004) rewrite this in the constitutive form of Equation 3.3 as

$$\tau_{ij} = \frac{\dot{\epsilon}_{ij}}{\dot{E}\sqrt{3}}\sigma_0\left[1 - \left(\frac{RT}{H_a} ln \frac{\sqrt{3}\dot{\epsilon}_0}{2\dot{E}}\right)^{1/2}\right]. \tag{3.9}$$

The quantities $\dot{\epsilon}_0$, σ_0, and H_a are experimentally determined, and given by *Goetze* (1978) to be $\epsilon_0 = 5.7 * 10^{11}$ s^{-1}, $\sigma_0 = 8.5$ GPa, and $H_a = 536$ kJ/mol, and other symbols are as in Table 1. In this form, *Molnar and Jones* (2004) compared the high stress effective viscosity coefficient to that from the power law relation, Equation 3.3. They determined that for geologically relevant strain rates, $10^{-13} - 10^{-15}$ s^{-1}, this high stress law would apply in the upper portions of the mantle lithosphere where temperatures are below $\approx 800 - 1000°C$ (*Goetze*, 1978; *Molnar and Jones*, 2004; *Tsenn and Carter*, 1987). This high stress law may also be well approximated using a power law with $n \geq 10$ for which stresses are rather insensitive to strain rates (e.g. *Dayem et al.*, 2009). Using $n = 10$ in equation 3.7 means that h/L becomes about 3, whereas for $n = 3.5$ it is about 8. If n is effectively 10, as it would be if dominated by the low-temperature flow law, then upper portions of the mantle lithosphere have the potential to be dynamically removed by this mechanism, along with the lower portions of the layer.

The assumption of a zero shear stress condition at the base of the crust represents one possible end member boundary condition, and can be justified geologically in several ways. One could argue that the lower crust should be weak compared to the upper mantle when it is sufficiently warm. Evidence of an eclogitic layer at the base of the crust could also suggest this boundary condition (e.g. *Harig et al.*, 2008) as eclogite is thought to deform at lower viscosities than granulite (e.g. *Austrheim*, 1991). Finally, a quartz-rich crust also has the potential to flow at relatively low shear stress at typical Moho temperatures (e.g. *Brace and Kohlstedt*, 1980; *Sibson*, 1977, 1982). Even at high pressures these flow stresses for quartz remain below a few MPa and microstructures suggest the stresses do not even reach this threshold to transition to dislocation creep (*Stöckhert and Renner*, 1998).

3.5.2 Intracontinental Magmatism

With a shear stress-free upper boundary, rheological exponent $n \geq 2$, and $\lambda' \geq 6$ downwellings and upwellings are separated by a central region that has relatively low internal

strain rate and near uniform horizontal velocity, and that moves as almost a coherent block. This suggests that localized thinning could be offset several hundred kilometers from the zone of downwelling.

Although potassic magmas can result from various triggers, they may link to lithospheric instabilities in several plate boundary regions. In the Sierra Nevada, broad high–potassium magmatism is one of several observations that indicate removal of lower lithosphere (in this case within 100 km of inferred downwelling). These volcanics of varying type (e.g. *Farmer et al.*, 2002) are inferred to have lithospheric mantle sources that have been metasomatized in a previous arc magmatism setting, as opposed to a depleted mantle source (e.g. *Turner et al.*, 1996). The convective removal of lower lithosphere allowed the lithospheric mantle to melt where thinned, either adiabatically in upward flow (e.g. *Elkins-Tanton and Grove*, 2003) or by simple conductive heating of shallow lithosphere exposed to hot asthenosphere (e.g. *Farmer et al.*, 2002), causing an abrupt pulse of magmatism at ca. 3.5 Ma.

Generally, since the metasomatism of lower lithosphere is preserved for as long as temperatures in the lithosphere remain below the solidus, these magmas are also possible away from current or geologically recent subduction zones, in settings that could have had subduction influences further back in time (*Elkins-Tanton*, 2005, 2007). For instance, much of the western United States can be assumed to have been hydrated by low angle subduction in the early Cenozoic (*Farmer et al.*, 2008). This potassic magmatism may also follow dry adiabatic melting of asthenosphere if the downwelling lithosphere releases hydrous volatiles as it sinks to greater pressures (*Elkins-Tanton*, 2005, 2007; *Elkins-Tanton and Hager*, 2000).

Melting in the localized upwelling zone should be controlled by the deflection of the lithosphere-asthenosphere boundary (Figure 3.4), the width of which depends on the rheological exponent, n (Figure 3.8). This melting ought not occur throughout the entire column of mantle lithosphere. While material near the top of the column would move upward adiabatically, its initially low temperature would prevent it from reaching its solidus, and hence

melting.

The localization of the upwelling zone when h/L is less than about three implies that when a shear-stress free surface might be applicable, magmatism could play an even more important role than considered previously. Firstly, thinning, and hence magmatism, need not occur near plate boundaries, where large stresses and strains can easily create the perturbation necessary to induce gravitational instability. Magmatism instead may appear several hundred kilometers into the continental plate. There, increased lithospheric thicknesses may hide surface indicators of thinning or extension such as rapid change of surface elevations or rifting. Second, magmatism may be more diagnostically important at smaller horizontal length scales than can be resolved with other techniques such as travel-time tomography or receiver function analysis. It may be that shorter scale, unresolved lithospheric instabilities occur, requiring densely spaced seismic networks for detection (*Yang and Forsyth*, 2006). In this case, the high–potassium magmatism may be the best evidence with which to begin an investigation of lithospheric removal induced by convective or Rayleigh-Taylor instability.

3.6 Conclusions

When the dimensionless wavelength of the perturbation, λ' (ratio of perturbation wavelength to layer thickness), is greater than approximately six, and shear-stress on the upper surface is negligible, a power law rheology causes 2D Rayleigh-Taylor instability to separate into two forms, controlled by viscosity, density, and stress-strain exponent. For low viscosity stratification ratios, $h/L \leq 2$ (for constant density) or $h/L \leq 3$ (for depth-dependent density), deformation concentrates at the ends of the unstable layer as localized upwelling and downwelling. The middle part of the layer moves horizontally towards the downwelling as a coherent block. Throughout the growth of the instability, the upwelling and downwelling grow at comparable rates.

As h/L increases, the similarities between upwelling and downwelling diverge. The vertical viscosity variation permits vertical gradients in horizontal velocity and prevents the

middle area from ever moving as a coherent block. Upwelling deformation is distributed over a broader area of the lower lithosphere and total thinning remains small as downwelling peaks.

The transition zone for intermediate values of h/L reflects a combination of these two end states. The initial growth of the instabilities mirrors those with separated upwellings and downwellings, which grow at similar rates, and a middle zone with subtle vertical gradients in horizontal velocity. Final stages of growth are similar to cases with large h/L, with downwelling growing rapidly and upwelling becoming more diffuse. This transition type appears at slightly higher viscosity stratification ratios with the introduction of depth varying density.

The estimated width of the maximum upwelling zone is controlled by the rheological exponent in the constitutive equation, and varies as $\approx n^{-1/2}$. The decay in horizontal velocity away from the side boundaries of our layer also indicates a $\approx n^{-1/2}$ relation. Together they compare well to earlier studies of deformation length scales for a half-space deformed by boundary stresses (*England et al.*, 1985).

We suggest the low viscosity stratification ratio required for plate-like deformation ($h/L < 3$) is plausible when considering the high-stress low-temperature creep regime. Approximating this regime with a $n > 10$ power law rheology can reduce the effective h/L to the $h/L < 3$ range. Without the high-stress regime, low h/L ratios are less realistic, and high values of B at low temperatures would prevent upper portions of the mantle lithosphere being removed when dynamical instability occurs. The Sierra Nevada, however, provides a counter example; estimates of the lithosphere's thermal structure prior to 10 Ma indicate removal of tens of kilometers of material colder than $900°C$ (e.g. *Molnar and Jones*, 2004) has occurred.

3.7 Acknowledgments

This research was supported by the National Science Foundation Grant EAR-0607831, a CIRES Graduate Student Research Fellowship to C. Harig, and a W. O. Thompson Fund grant to C. Harig from the Dept. of Geological Sciences. We thank G. L. Farmer for helpful discussions and thank L. T. Elkins-Tanton and an anonymous reviewer for thoughtful and constructive reviews. Figures created with the GMT software (*Wessel and Smith*, 1998) and the open source software gnuplot.

B	Viscosity coefficient (where constant in the layer)
B_0	Viscosity coefficient at the base of the layer, through which it decreases with depth
d_e	Equilibrium thickness of the unstable layer defined by *Canright and Morris* (1993) as the thickness that has no tendency to grow or shrink
$\dot{E}$	Second invariant of the strain rate tensor
E_a	Activation energy
g	Gravitational acceleration
H_a	Experimentally determined activation energy constant (535 kJ/mol) in the high stress constitutive equation
h	Initial thickness of layer
L	Characteristic e-folding depth scale for exponential decrease in viscosity coefficient
n	Rheological exponent in the stress-strain constitutive equation
p	Pressure
R	Gas-law constant
t	Time
t_b	Time when downwelling detaches from upper surface
T	Temperature
T_0	Temperature at base of layer
ΔT	Temperature difference across layer
u	Horizontal component of velocity
w	Vertical component of velocity
x	Horizontal coordinate
z	Vertical coordinate set to zero at the bottom interface of the layer and positive upward in our numerical cases
δ	Thickness of layer as function of time, from *Canright and Morris* (1993)
λ	Wavelength of perturbation to layer
ρ	Density
$\Delta\rho$	Density difference between the layer and the underlying half-space or subspace
ϵ_{ij}	Strain component
$\dot{\epsilon}_{ij}$	Strain rate component
$\dot{\epsilon}_0$	Experimentally determined strain rate constant ($5.7 * 10^{11}$ s^{-1}) in the high stress constitutive equation
σ_{ij}	Stress component
σ_0	Experimentally determined stress constant (8.5 GPa) in the high stress constitutive equation
τ_{ij}	Deviatoric stress component

Table 3.1: Definition of symbols.

Chapter 4

Constraints on upper mantle viscosity from the flow-induced pressure gradient across the Australian continental keel

4.1 Abstract

The thickness of continental lithosphere varies considerably from tectonically active to cratonic regions, where it can be as thick as 250–300 km. Embedded in the upper mantle like a ship, when driven to move by a velocity imposed at the surface, a continental keel is expected to induce a pressure gradient in the mantle. We hypothesize that the viscosity of the asthenosphere or the shear coupling between lower lithosphere and asthenosphere should control this pressure effect and thus the resulting dynamic topography. We perform three-dimensional finite-element calculations to examine the effects of forcing a continental keel by an imposed surface velocity, with the Australian region as a case study. When the upper mantle is strong, but still weaker than the lower mantle, positive dynamic topography is created around the leading edge, and negative dynamic topography around the trailing edge of the keel, which is measurable by positive and negative geoid anomalies, respectively. For a weak upper mantle the effect is much reduced.

We analyze geoidal and gravity anomalies in the Australian region by spatiospectral localization using Slepian functions. The method allows us to remove a best-fit estimate of the geographically localized low spherical-harmonic degree contributions. Regional geoid anomalies thus filtered are on the order of ± 10 m across the Australian continent, with a spatial pattern similar to that predicted by the models. The comparison of modeled and

observed geoid anomalies places constraints on mantle viscosity structure. Models with a two-layer mantle cannot sufficiently constrain the ratio of viscosity between the upper and lower mantle. The addition of a third, weak, upper-mantle layer — an asthenosphere — amplifies the effects of keels. Our three-layer models, with lower-mantle viscosity of 3×10^{22} Pa s, suggest that the upper mantle (asthenosphere) is 300 times weaker than the lower mantle, while the transition zone (400–670 km depths) has a viscosity varying between 10^{21} and 10^{22} Pa s.

4.2 Introduction

Our understanding of Earth's deformation and dynamics fundamentally depends on the rheology of the mantle. The viscosity structure of the mantle has been inferred mainly by studying the response to disappearing glacial surface loads over the past 10^5 years (e.g. *Cathles*, 1975; *Peltier*, 1976; *Wu and Peltier*, 1983; *Yuen and Sabadini*, 1985; *Nakada and Lambeck*, 1989; *Lambeck et al.*, 1990; *Mitrovica*, 1996; *Simons and Hager*, 1997; *Mitrovica et al.*, 2007) and by examining geophysical signals from models of mantle convection, such as long-wavelength geoid anomalies and surface plate velocities (e.g. *Hager*, 1984; *Ricard et al.*, 1984; *Hager and Richards*, 1989; *King and Masters*, 1992; *Forte and Peltier*, 1994). Results from these methods have not always been consistent. Analyses of convection-related observables have routinely suggested that the upper mantle is less viscous than the lower mantle by a factor of at least 30, and perhaps as much as 300. On the other hand, studies of glacial-isostatic adjustment sometimes argue for less than a factor of 10 variation (*Peltier*, 1998). Jointly inverting several types of data has provided additional detail (e.g. *Mitrovica and Forte*, 2004), but the mantle's viscosity structure remains incompletely resolved. This is mainly due to the poor vertical resolution of the post-glacial rebound data (*Paulson et al.*, 2007a,b). Here, we consider whether pressure gradients across continental keels can be used to place a meaningful constraint on the viscosity of the upper mantle.

The thickness of the continental lithosphere varies considerably from tectonically active

to stable cratonic regions (*Artemieva*, 2009). Determining the depths of continental keels has been an area of much study and debate over the past several decades (*King*, 2005), with estimates historically ranging from 175 to 400 km. Observations of surface heat flux, for example, suggest a thick Archean lithosphere (e.g., *Rudnick et al.*, 1998), though nowhere exceeding 250 km (e.g., *Ballard and Pollack*, 1987; *Nyblade and Pollack*, 1993; *Jaupart et al.*, 1998). Analyses of mantle xenoliths, if indeed representative of a conductive geotherm, have led to thickness estimates in the lower end of the range, 150–200 km (*Rudnick et al.*, 1998). Measurements of electrical conductivity show that differences between oceanic and Archean cratonic regions are limited to depths shallower than 250 km (*Hirth et al.*, 2000). Seismically, lithosphere is typically considered to extend to depths where shear-wave speeds are significantly faster than the global average speed (usually >1.5–2%) (*Masters et al.*, 1996; *Mégnin and Romanowicz*, 2000; *Simons and van der Hilst*, 2002; *Ritsema et al.*, 2004). While some types of data are known to be influenced by anisotropy in the upper mantle (*Ekström and Dziewonski*, 1998; *Gung et al.*, 2003), most recent seismic estimates generally limit lithospheric thickness to at most 300–350 km (*Artemieva*, 2009). Overall, across disciplines, the continental-keel thickness estimates are in the range of 200–300 km. In particular, Australia, our region of interest, consistently yields some of the highest estimates of any craton, with fast seismic wave speed anomalies persistent to depths of 250–300 km in models of V_{SV}, the vertically-polarized shear-wave speed (e.g. *Debayle and Kennett*, 2000a; *Simons et al.*, 2002; *Ritsema et al.*, 2004).

The base of the lithosphere has much significance to geodynamics since, as a mechanical lower boundary, it separates the rocks which remain coherent parts of the lithosphere over geologic time from those below that are part of the convecting mantle (*Turcotte and Oxburgh*, 1967). It is for this reason that such thick continental keels are expected to translate with plate motion over long time scales; an observation that is corroborated by the global correlation of continental crustal age with lithospheric thickness at long wavelengths (*Simons and van der Hilst*, 2002). Furthermore, continental keels influence the coupling between mantle

and lithosphere, thus affecting net rotation of lithosphere (*Zhong*, 2001; *Becker*, 2006, 2008) as well as regional lithospheric deformation (*Conrad and Lithgow-Bertelloni*, 2006).

The motion of continental keels through the upper mantle, which is relatively less viscous, can be expected to induce pressure perturbations in the mantle moving around them (*Ricard et al.*, 1988). Such pressure gradients will mainly be controlled by the viscosity and thickness of the asthenospheric channel below the lithosphere. If the viscosity of this channel is low relative to the rest of the mantle the pressure gradient should cause return flow beneath the keel with little effect on dynamic topography at the Earth's surface. However at higher asthenospheric viscosities the return flow should be reduced in favor of a signal in the surface topography and hence gravity anomalies or the geoid. *Ricard et al.* (1988) used an approximate mode-coupling method to estimate these geoidal anomalies in the tens of meters.

In this study we constrain the viscosity of the upper mantle by comparing modeled dynamic geoid anomalies to observations. As these signals are proportional to the magnitude of velocity change across the mantle, we focus on the Australian continent, with its relatively large surface velocities. We analyze the regional geoidal anomalies by spatiospectral localization using Slepian functions. Our results will also be applicable to understanding the development of seismic anisotropy beneath continental cratons and the orientation of the lithospheric stress field surrounding them.

4.3 Analytical Treatment

To illuminate the physics, we first consider a simplified problem in two dimensions (2D) that can be solved analytically by neglecting flow in the third dimension, normal to surface motion. We examine the flow at two locations: in the far-field, in which a lithosphere of uniform thickness moves over a layered viscosity structure, and the flow beneath a keel, where a much thicker lithosphere moves over the same layers. In both of these locations we would expect only horizontal flow. Therefore, from conservation of mass, the amount of

horizontal flow at these locations should balance each other. This takes the form of the flux balance

$$\int_K u(z)\,dz = \int_F u(z)\,dz, \tag{4.1}$$

where the material flux across a vertical plane is the integral of the horizontal velocity function u over depth. Horizontal and vertical coordinates are represented by x and z, and the subscript K indicates the location under the keel, while F indicates the far-field (Table 4.1). This is also illustrated in the cartoon Figure 4.1A, where the arrows representing the amount of mass flow change with depth but sum to the same amount in each region. Since the motion of the lithosphere is constant, the flow in the underlying mantle must balance the excess mass transported in regions of thick lithosphere (i.e. keel regions). In one-dimensional channel flow (*Turcotte and Schubert*, 2002), the equation of motion can be written as

$$\frac{\partial \tau}{\partial z} = \frac{\partial p}{\partial x} \quad \text{or} \quad \eta \frac{\partial^2 u}{\partial z^2} = \frac{\partial p}{\partial x}, \tag{4.2}$$

where τ is the shear stress and p the pressure. The viscosity, η, is assumed to be constant in each layer. By integration we obtain an equation for the velocity, u, as a function of depth, which is subsequently solved for by applying the boundary conditions. These are: constant velocity at the surface, and fixed zero velocity at the bottom. In the far-field case of surface-driven motion, $\partial p/\partial x$ can be considered as zero, and we have linear velocity functions with velocity everywhere in the same direction as the top surface. Underneath the keel, a horizontal pressure gradient is allowed and can be solved for when balancing the material flux.

We simplify our solutions by non-dimensionalizing pressure and coordinates by the relevant length, mass, and time scales. For layers with constant viscosity we use

$$p' = \frac{p}{\left(\dfrac{u_0 \eta_{LM}}{h_0}\right)} \quad \text{and} \quad x' = \frac{x}{h_0}, \tag{4.3}$$

where p' is dimensionless pressure, x' is dimensionless horizontal coordinate, u_0 is the hori-

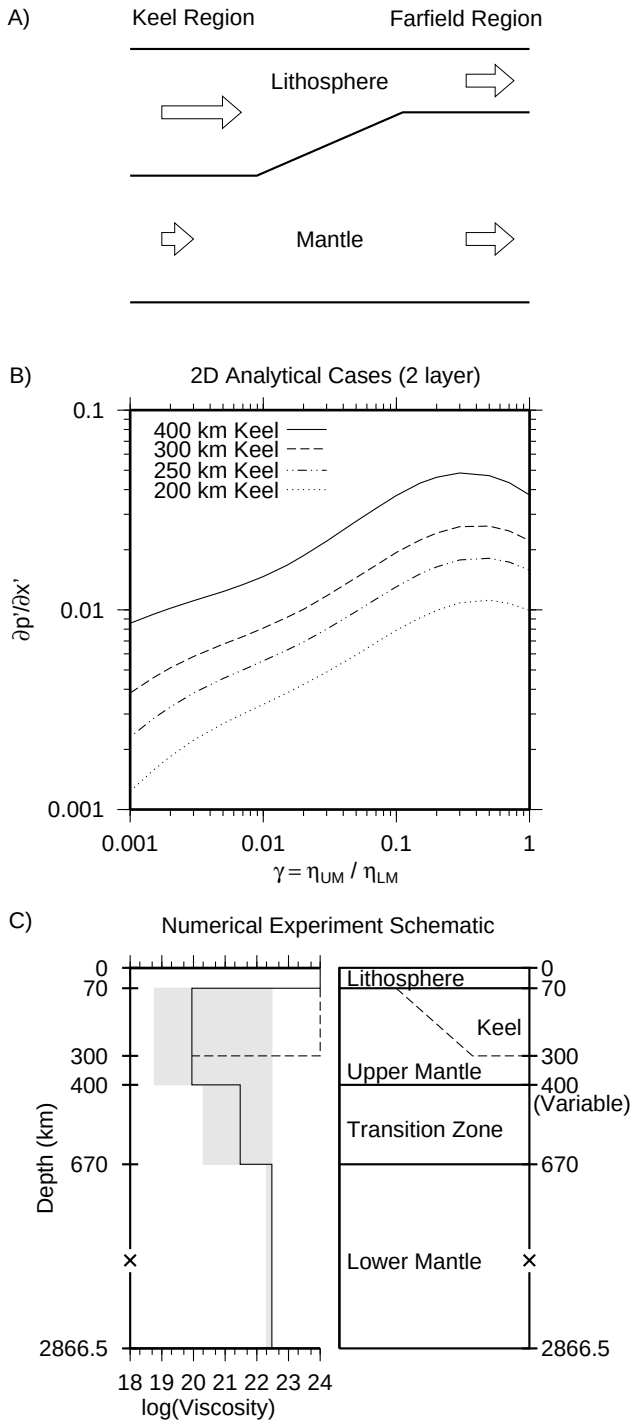

Figure 4.1: A) Cartoon illustrating the mass-balance argument in the analytical treatment in Section 4.3. Arrows represent the amount of mass transported in each region. Since the lithosphere moves with constant motion, the flow in the underlying mantle must balance the excess mass transported in regions of thick lithosphere (i.e., the keel region). B) Dimensionless pressure gradients from the two-layer analytical solution (eq. 4.6), for various keel thicknesses and γ, the ratio of upper mantle to lower-mantle viscosities. C) Numerical experiment schematic. The left shows viscosity variation with depth. Solid line is the preferred model, dashed line shows keel viscosity. Grey shades show variations of viscosity considered. The right shows assumed layering. Maximum keel depth is 300 km. Upper mantle-transition zone boundary is varied to set channel thickness between the keel and transition zone.

zontal velocity at the surface, η_{LM} is the viscosity of the lower mantle, and h_0 is the thickness of the upper mantle in the non-keel region. Values such as the thickness of the upper mantle channel below the keel, h, and the thickness of the lower mantle, d, nondimensionalize to $h' = h/h_0$ and $d' = d/h_0$. We also use $k = h_0 - h$ as the thickness difference between the keel and the surrounding lithosphere, written dimensionless as $k' = (h_0 - h)/h_0$.

For a uniformly-viscous mantle the keel-induced pressure gradient is a well-known result, which varies as the cube of the channel thickness, h, written as

$$\frac{\partial p}{\partial x} = 6u_0\eta\frac{k}{h^3} \quad \text{or} \quad \frac{\partial p'}{\partial x'} = 6\frac{k'}{h'^3}. \tag{4.4}$$

This is similar to eq. (6–22) by *Turcotte and Schubert* (2002), except that we allow for a non-zero far-field flux equal to that of uniformly-thick lithosphere.

When the mantle has multiple viscous layers, the dependence on the thickness of the weakest layer is more complex. For a two-layered mantle, velocity is solved for in each layer, and then the dimensionless pressure gradient can be written as

$$\frac{\partial p'}{\partial x'} = \frac{\gamma\left(\dfrac{h'^2 - \gamma d'^2}{\gamma d' + h'}\right) - \gamma\left(\dfrac{1 - \gamma d'^2}{\gamma d' + 1}\right)}{\dfrac{1}{2}(h'^2 - \gamma d')\left[\dfrac{\gamma(-2d'h' - d'^2) - h'^2}{\gamma d' + h'}\right] + A}, \tag{4.5}$$

$$A = -\frac{1}{3}\gamma d'^2(2d' + 3h') + \frac{h'^3}{3}. \tag{4.6}$$

Here, $\gamma = \eta_{UM}/\eta_{LM}$ is the ratio of the viscosities of both layers. Setting the thickness of the lower mantle, d', to zero reduces eq. 4.6 to eq. 4.4. Assuming that the thicknesses of the upper and lower mantle are fixed with the boundary at 670 km depth, we plot the pressure gradient versus γ, the ratio of upper-mantle to lower-mantle viscosities, for several keel thicknesses (Figure 4.1B). As expected, a thicker continental keel results in larger dimensionless pressure gradients. More interesting, however, is the variation with γ. As γ is decreased from one (uniform-viscosity mantle), pressure gradients initially increase even though upper-mantle viscosity is lower. Pressure gradients eventually peak, and decrease with decreasing γ.

We also considered a three-layered mantle with a fixed 300 km thick keel and another division around 400 km depth. While this system is more complex, the cases we checked showed a weak upper mantle may result in increased pressure gradients and thus increased dynamic topography, as in the two-layered case.

The analytical model illuminates the problem of flow-generated dynamic topography in the following ways. First, the addition of a weak layer in the upper mantle can enhance the effect of continental keels and increase pressure gradients. Second, the magnitude of surface velocity exerts strong control over dynamic topography since it directly scales the pressure gradient, as per eq. 4.3: the higher the surface velocity, the more dynamic topography can be generated in the system.

While idealized, a 2D analytical treatment of the problem easily illustrates our hypothesis: that continental keels induce both horizontal variations in mantle velocity and pressure that are controlled by the details of the viscosity structure. We continue this analysis with more realistic three-dimensional (3D) calculations, focusing on the unique gravity signals resulting from the dynamic topography. The absence or presence of these signals in Earth's observed gravity field then allow us to bound the plausible viscosity structure below.

4.4 Numerical Experiment Setup

Our keel models are kept relatively simple, since we intend to examine the first-order effects of their motion only. We begin by assuming boundary-driven flow, and neglect mantle and crustal buoyancy forces. This Stokes flow problem is governed by two of the conservation equations of viscous fluids, those for mass and momentum, represented in dimensionless form as

$$\boldsymbol{\nabla} \cdot \mathbf{v} = 0, \tag{4.7}$$

$$-\boldsymbol{\nabla} p + \boldsymbol{\nabla} \cdot [\eta(\boldsymbol{\nabla}\mathbf{v} + \boldsymbol{\nabla}^{\mathrm{T}}\mathbf{v})] = 0, \tag{4.8}$$

where $\mathbf{v}, p, \eta$ are the velocity vector, pressure, and viscosity, respectively.

These equations are solved with the parallel finite-element code CitcomCU (*Moresi and Gurnis*, 1996; *Zhong*, 2006). We design our model space in regional spherical geometry to span depths from the surface to the core-mantle boundary (CMB), and to cover a 120° by 120° area. Typical resolution for each case is 192, 192, and 104 elements in longitude, latitude, and radial direction respectively, giving 0.625° per element of horizontal resolution. Vertical resolution is enhanced in the upper mantle at the expense of lower-mantle resolution to properly resolve the expected large vertical gradients in horizontal velocity. The upper mantle (between 70 and 670 km depth) has 10 km per element of radial resolution, while the lower mantle and lithosphere above 70 km depth have 57.8 km and 14 km per element of radial resolution, respectively. We specify the thickness of lithosphere at every column of elements and center the keel in our model space at 60° longitude, 0° latitude. The surface velocity is then fixed to result from an Euler-pole rotation with an axis at 90° latitude with rotation magnitude of 1 cm/yr. We use a fixed boundary condition on the bottom, which will be discussed further later. On the sides of our box that are parallel to the flow direction we use reflecting boundary conditions. On the sides perpendicular to flow, we use periodic boundary conditions which allow free through-flow with identical velocity on either side. Thus the combined velocity solutions for the side boundaries are mass-preserving. Perturbations to the pressure field caused by the keel motion result in dynamic topography at the surface. We analyze the gravity anomalies associated with this dynamic topography and make comparisons to the observed field.

Since dynamic topography directly scales with the magnitude of surface velocity for the Newtonian rheology used in our calculations, we focus our study on the Australian continent, which is the fastest-moving continental plate. When imposing surface velocity we use the azimuth of plate motion at the center (130° E, 25° S) of Australia's lithospheric keel from the HS3-NUVEL1A model, which is 1.81° East of North (*Gripp and Gordon*, 2002) and, later, scale the results by the surface-velocity magnitude of 8.267 cm/yr. The prescribed surface boundary conditions are the driving force in our calculations and may do work on

the calculation medium (e.g. *Han and Gurnis*, 1999). If this work induces significant stresses at the surface it may influence the dynamic topography of our calculations. We performed calculations with various lithospheric viscosities (including the keel) between 10 and 500 times that of the lower mantle. As long as the lithosphere is sufficiently more viscous than the upper mantle, there was very little difference in the resulting surface stresses, hence dynamic topography and geoid, indicating that stresses at the surface are caused by the pressure perturbations in the upper mantle associated with keel structure. Also, our use of periodic inflow/outflow boundary conditions likely minimizes this effect. While our calculations use surface motions over a passive mantle, mantle flow beneath a fixed keel could produce similar pressure gradients. The important quantity is the net shear between the surface and the underlying mantle which could be influenced by buoyancy-driven flow, such as subduction. Accordingly we examined mantle flow beneath Australia from a global mantle-flow model driven by both plate motion and mantle buoyancy (see *Zhang et al.* (2010)) to investigate whether the velocity boundary conditions assumed at the top and bottom are valid. While this is discussed further in Section 4.6.4, the results are broadly consistent with what we assume in this regard.

We use the upper-mantle shear-velocity tomography model CUB2.0 (*Shapiro and Ritzwoller*, 2002) to create lithospheric keel-thickness distributions for our calculations (Figure 4.2A). Since the Australian continent is surrounded by relatively young oceanic lithosphere (*Müller et al.*, 2008), lithospheric thickness is set to a minimum of 70 km. At each increasing depth we use a +2% cut-off shear-wave velocity-perturbation contour with respect to the ak135 reference model (*Kennett et al.*, 1995) to estimate the extent of the continental keel. As mentioned earlier, estimates for the thickness of continental cratonic lithosphere from seismic tomography depend on the type of data used. The CUB2.0 model was created via a Monte-Carlo inversion of global surface-wave dispersion data using both Rayleigh and Love waves. *Shapiro and Ritzwoller* (2002) specifically allow for radial anisotropy in their inversion, down to a depth of 250 km. Where possible, we use the best-fitting V_{SV} estimate,

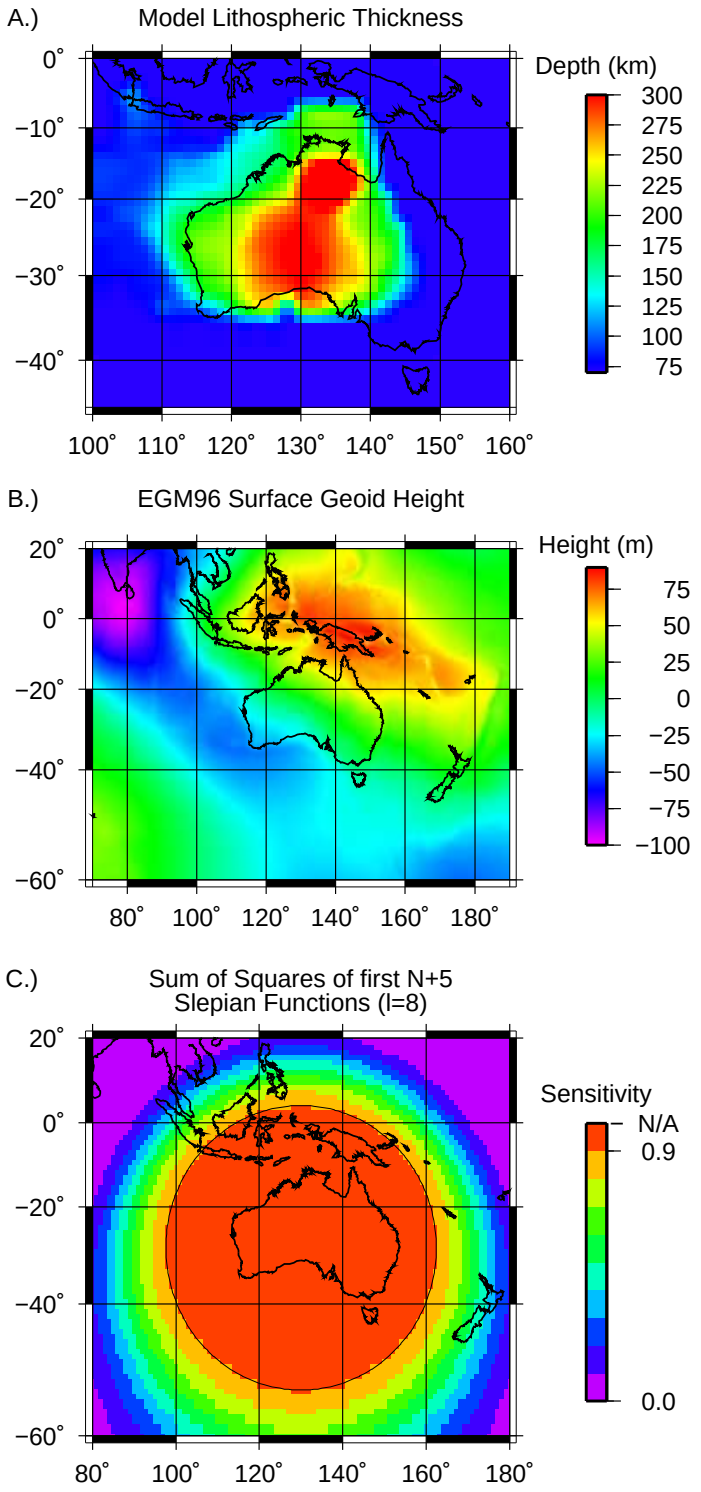

Figure 4.2: A.) Plot of keel depth from the tomography model CUB2.0 (*Shapiro and Ritzwoller*, 2002). We map the +2% shear-wave speed perturbation from initial model ak135 using V_{SV} and set a maximum lithosphere depth of 300 km depth. B.) Colored EGM96 geoid height without the degree $l = 2$ zonal spherical harmonic coefficient. C.) Plot of the sum of squares $\sum_{\alpha=1}^{N+5} g_\alpha^2$ of the first $N + 5$ eigenfunctions localized within a 30° circular region centered in western Australia for the bandwidth $L = 0$–8. The colored field shows the sensitivity of our filter to the region of interest. Overlain is the 90% contour of this sensitivity.

which is consistently smaller than the V_{SH} estimate. Below this depth their data is unable to constrain radial anisotropy and the estimated isotropic shear-wave speed, V_S, is used. We limit the thickness of the lithosphere to 300 km since greater thicknesses are not supported by the majority of tomographic upper-mantle models.

Our models use layered viscosity structures according to the schematic shown in Figure 4.1C. Mantle viscosities are constant with depth within each layer and are rendered dimensionless by a reference value of 2×10^{21} Pa s. Lithospheric viscosity and keel viscosity, are set to a constant significantly higher than the mantle (e.g. 10^{24} Pa s). We begin with a two-layered mantle with viscosity contrast at 670 km and vary the ratio of viscosities of the lower and upper mantle. Calculations are then performed with a three-layered mantle with divisions at 670 km and 400 km depth. Finally, our experiments also vary the thickness of the asthenospheric channel from 50 to 150 km to examine the trade-off between channel viscosity and thickness.

4.5 Analysis of Gravity

We seek to compare the dynamic geoid anomalies in our calculations to Earth's observed geoid in an effort to constrain the viscosity structure of the upper mantle. This task is neither simple nor straightforward. The Earth's gravitational potential at a given surface point receives contributions from the mass distribution at all depths beneath and around it. In the Australasian region (Figure 4.2B) we would therefore expect the geoid (*Lemoine et al.*, 1998) to reflect the mass redistribution processes that occur in the surrounding subduction zones (*McAdoo*, 1981), and processes in the lower mantle (*Hager and Richards*, 1989), in addition to the dynamic signal that we must thus attempt to isolate. Fortunately, we expect our dynamic signals to be localized both spatially and spectrally. By examining equivalently localized contributions to Earth's gravitational-potential field we can distinguish possible dynamic signals from these other regional contributions.

The usual spherical-harmonic representation of potential fields links spatial and spec-

tral information through global spherical basis functions which have perfect frequency selectivity but none in space (e.g. *Freeden and Michel*, 1999). In order to isolate a spatially localized contribution to the signal, spectral and spatial concentration must be balanced somehow.

For instance, *Simons and Hager* (1997) developed a procedure that constrains regional contributions to global spherical-harmonic spectra to examine the rebound of the Canadian shield after removal of its ice sheet. They constructed isotropic bandlimited windowing functions on domains with circular symmetry from zonal spherical harmonics, according to a sensible but non-optimal (see, e.g., *Wieczorek and Simons*, 2005) concentration criterion. After their pioneering work, *Simons et al.* (2006) showed how to derive a family of optimally concentrated basis functions on domains with arbitrarily irregular boundaries. As their construction uses *all* of the available spherical harmonics Y_{lm}, of integer degree $l = 0, \ldots, L$, and order $m = -l, \ldots, l$, the "Slepian" basis, g_α, $\alpha = 1, \ldots, (L+1)^2$, as it has come to be known, is a perfect alternative to the spherical harmonics. Indeed, any scalar geophysical function, $s(\hat{\mathbf{r}})$, that is bandlimited to degree L and lives (without loss of generality) on the surface of the unit sphere can be represented completely equivalently in either basis,

$$s(\hat{\mathbf{r}}) = \sum_{l=0}^{L} \sum_{m=-l}^{l} s_{lm}\, Y_{lm}(\hat{\mathbf{r}}) = \sum_{\alpha=1}^{(L+1)^2} s_\alpha\, g_\alpha(\hat{\mathbf{r}}). \tag{4.9}$$

The Slepian functions, g_α, which are bandlimited to some degree L, are always constructed with reference to a particular spatial region of interest, R, of area A, on the surface of the unit sphere, Ω. The criterion for concentration to the region of interest is quadratic: the Slepian functions are those that maximize their energy locally for the available bandwidth, following

$$\lambda = \frac{\int_R g_\alpha^2(\hat{\mathbf{r}})\, d\Omega}{\int_\Omega g_\alpha^2(\hat{\mathbf{r}})\, d\Omega} \quad = \quad \text{maximum}, \tag{4.10}$$

and where $1 > \lambda > 0$. Practically, they are given by the spherical-harmonic expansion

$$g_\alpha(\hat{\mathbf{r}}) = \sum_{l=0}^{L} \sum_{m=-l}^{l} g_{\alpha\, lm} Y_{lm}(\hat{\mathbf{r}}), \tag{4.11}$$

where the coefficients, $g_{\alpha\, lm}$, are obtained by solving the eigenvalue equation

$$\sum_{l'=0}^{L} \sum_{m'=-l'}^{l'} D_{lm,l'm'} g_{l'm'} = \lambda\, g_{lm}. \tag{4.12}$$

The four-dimensional object whose elements $D_{lm,l'm'}$ are products of spherical harmonics, integrated over the region R, is called the localization "kernel" (*Simons et al.*, 2006).

The eigenvalues of this problem, $\lambda_1, \lambda_2, \ldots, \lambda_{(L+1)^2}$, sum to a space-bandwidth product termed the "spherical Shannon number", N. Typically, N is a good estimate of the number of significant eigenvalues, and thus of the number of well-concentrated functions for the problem at hand. As a result, an expansion of the signal in terms of its first N Slepian functions provides a high-quality regional approximation to the signal in the region (*Simons and Dahlen*, 2006), at the bandwidth level L. Since

$$N = (L+1)^2 \frac{A}{4\pi}, \tag{4.13}$$

where $A/(4\pi)$ is the fractional area of localization, the effective dimension of the Slepian basis is much reduced compared to the $(L+1)^2$ terms in the spherical-harmonic expansion. The Slepian functions are efficient for the study of geographically localized geophysical signals, which are sparse in this basis (*Simons et al.*, 2009),

$$s(\hat{\mathbf{r}}) \approx \sum_{\alpha=1}^{N} s_\alpha\, g_\alpha(\hat{\mathbf{r}}) \quad \text{for} \quad \hat{\mathbf{r}} \in R. \tag{4.14}$$

The geoid in the region of Australia (Figure 4.2B) is dominated by two striking features: a broad and large-amplitude positive anomaly to the north near Indonesia and the Western Pacific, and an equally broad and large-amplitude negative anomaly south of India trending to the southeast. Both anomalies are rather long-wavelength features, and can be attributed to the history of subduction and lower-mantle structure in the area (e.g. *Hager and Richards*,

1989; *Ricard et al.*, 1993). A simple estimate for the size of a dynamic keel-related (i.e. model-generated) signal would be roughly the size of the keel itself. Therefore, we shall determine spatiospectrally localized functions to remove the longer-wavelength contributions to the regional geoid in and around Australia both in the observations and in our model domain, thereby hopefully preserving the signal. By removing the long-wavelength geoid contributions and ascribing what remains to the keel movement we run the risk of incurring bias from an unexpected contribution to the geoid in our analysis. However, the unique spatial pattern in our modeled geoid and its agreement with the filtered observed geoid supports our modelling approach.

We elect to use our functions to remove bandwidths below $L = 8$. This roughly corresponds to the wavelength of our keel outline and our experience has shown that it acceptably balances removing broad, regional geoid features with the preservation of sufficient model signal for analysis. We separate the observations into a low-degree and a high-degree part in both the spherical-harmonic and the Slepian basis of bandwidth L, as

$$
\begin{aligned}
s(\hat{\mathbf{r}}) &= \sum_{l=0}^{L_{\max}} \sum_{m=-l}^{l} s_{lm}\, Y_{lm}(\hat{\mathbf{r}}), && (4.15)\\
&= \sum_{l=0}^{L} \sum_{m=-l}^{l} s_{lm}\, Y_{lm}(\hat{\mathbf{r}}) + \sum_{l=L+1}^{L_{\max}} \sum_{m=-l}^{l} s_{lm}\, Y_{lm}(\hat{\mathbf{r}}), && (4.16)\\
&= \sum_{\alpha=1}^{(L+1)^2} s_\alpha\, g_\alpha(\hat{\mathbf{r}}) + \sum_{l=L+1}^{L_{\max}} \sum_{m=-l}^{l} s_{lm}\, Y_{lm}(\hat{\mathbf{r}}). && (4.17)\\
&= \sum_{\alpha=1}^{N} s_\alpha\, g_\alpha(\hat{\mathbf{r}}) + \sum_{\alpha=N+1}^{(L+1)^2} s_\alpha\, g_\alpha(\hat{\mathbf{r}}) + \sum_{l=L+1}^{L_{\max}} \sum_{m=-l}^{l} s_{lm}\, Y_{lm}(\hat{\mathbf{r}}). && (4.18)
\end{aligned}
$$

Compared to the original expansion (4.15), eq. (4.18) represents the signal with the low-degree components separated into local (the first term) and nonlocal (the second term) contributions. The first term in eq. (4.18) can thus be omitted in order to remove the local contributions to the low-degree signal.

If we sum the squares of all of the Slepian functions the value N/A is reached everywhere on the unit sphere (*Simons et al.*, 2006); by performing the partial sum of the first N

terms we obtain

$$\sum_{\alpha=1}^{N} g_\alpha^2(\hat{\mathbf{r}}) \approx \frac{N}{A} \quad \text{for} \quad \hat{\mathbf{r}} \in R. \tag{4.19}$$

By plotting the sum of the first several squared Slepian eigenfunctions we can determine where the truncated expansion is most sensitive and thus most successful at subtracting regional contributions. We will target our attention to the area where the analysis reaches 90% of its maximum sensitivity by this measure. In practice, this means that we shall take the first $N + 5$ basis functions to guarantee the efficient removal of low-degree signal from the region of interest (Figure 4.2C).

When the geoid is bandlimited to increasingly higher spherical-harmonic degrees, f shorter-wavelength signals begin to dominate the field. Around Australia, the sharp density contrast between the continental lithosphere and oceanic lithosphere that is over 100 Ma old results in prominent geoid anomalies along the coastline in the shorter-wavelength geoid field. We apply a simple, approximate, correction for these anomalies, derived by *Haxby and Turcotte* (1978). This correction assumes that topography and bathymetry follow Airy isostatic compensation, and therefore it expresses the change in the moment of the density distribution that is expected when the thickness of crust varies. We apply this correction to the geoid from the EGM96 model (*Lemoine et al.*, 1998) prior to the Slepian filtering technique.

We illustrate the application of our method in Figure 4.3 using data from EGM96. The Slepian functions we use will be designed to fit the localized power at the low degrees of the geoid. They are bandlimited to $L = 8$ and are concentrated within a region of interest of colatitudinal radius $\Theta = 30^\circ$ centered on colatitude $\theta_0 = 115^\circ$ and longitude $\phi = 130^\circ$ (i.e., the center of the Australian keel). The corresponding rounded Shannon number $N = 5$. The panels in the top row (Figures 4.3A–C) display various versions of the EGM96 geoid height that are simply truncated, namely after removal of the degrees l through 2, through 8, and

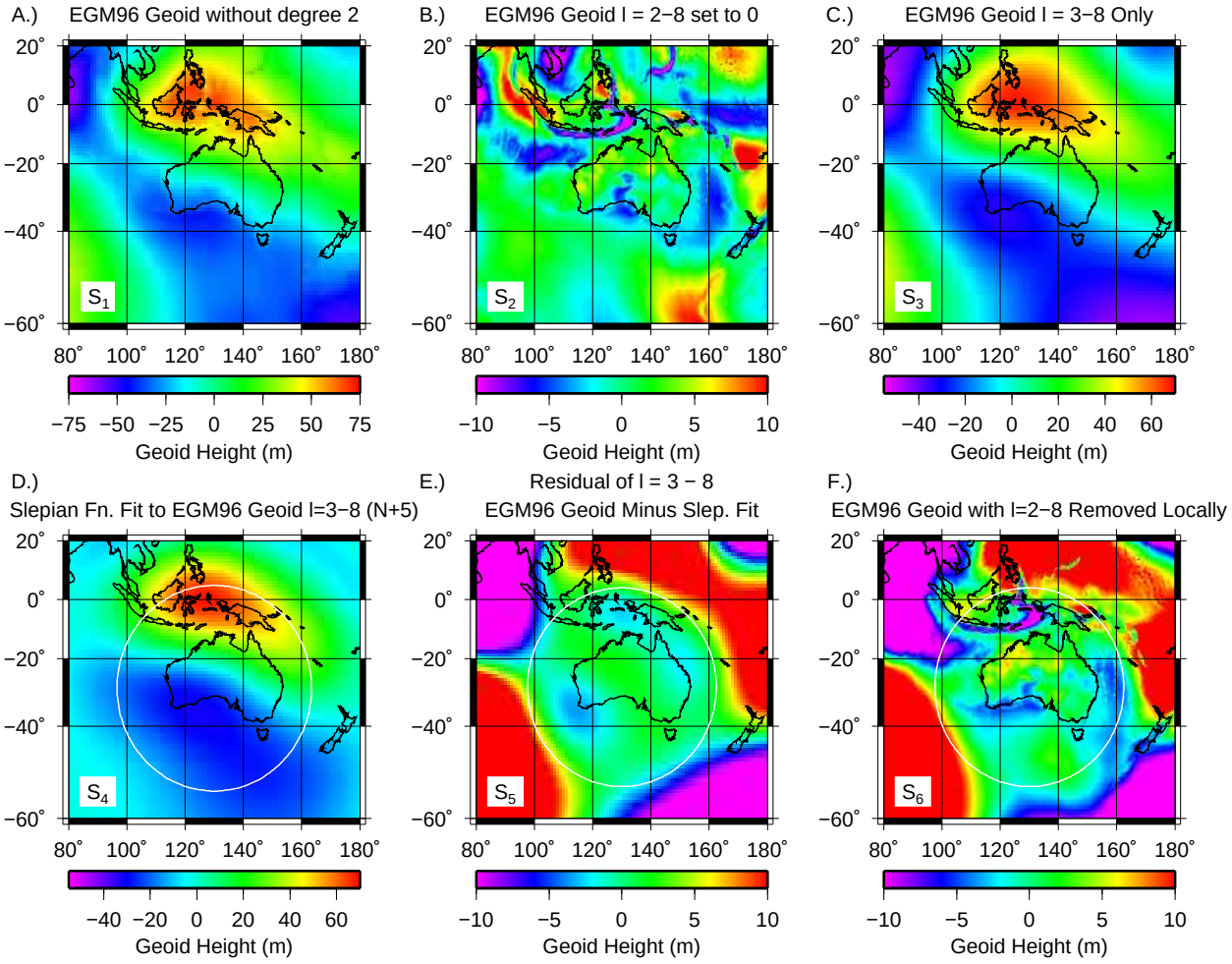

Figure 4.3: Example of Slepian filtering technique for a low maximum bandwidth of $L = 8$. The top row of panels (A–C) displays spectrally truncated versions of the EGM96 geoid height. The bottom row of panels (D–F) shows the filtering process. (A) The complete EGM96 geoid undulation with degree $l = 2$ removed. (B) The geoid with all coefficients from $l = 2$ through $l = 8$ set to zero. (C) The geoid between $l = 3$–8. In this example, our functions are designed to fit the localized power of these low degrees. (D) The fit of the first $N + 5$ Slepian eigenfunctions to the low-degree EGM96 geoid (panel C), concentrated within a 30° circular region (outlined in white) centered over western Australia. (E) The residual after subtracting the Slepian fit from the low-degree EGM96 geoid. Overlain in white is the 90% contour of sensitivity from Figure 4.2C. (F) The results of subtracting the low-degree Slepian fit from the full EGM96 geoid (panel A). Panels B, E, and F are shown with the same color scale, as are panels C and D.

between 9–360, respectively, i.e.

$$s_1 = \sum_{l=3}^{360} \sum_{m=-l}^{l} s_{lm}\, Y_{lm}, \tag{4.20}$$

$$s_2 = \sum_{l=9}^{360} \sum_{m=-l}^{l} s_{lm}\, Y_{lm}, \text{ and} \tag{4.21}$$

$$s_3 = \sum_{l=3}^{8} \sum_{m=-l}^{l} s_{lm}\, Y_{lm}. \tag{4.22}$$

For reference we note that s_1, in Figure 4.3A, is a fair approximation to the Earth's non-hydrostatic geoid.

In the course of our analysis we found that reconstructing the low-degree geoid with a Slepian basis of more than N terms was necessary to obtain good fits to the modeled data. Therefore, Figure 4.2C and the bottom row of panels, Figures 4.3D–F, use $N + 5 = 10$ basis functions to remove the local signal. Including these extra functions does not significantly affect the trade-off between spatial and spectral localization. In the bottom row of panels of Figure 4.3 we show the filtering process by first showing, in Figure 4.3D, the fit of the first $N + 5$ Slepian eigenfunctions to the low-degree EGM96 geoid (i.e., s_3 shown in Figure 4.3C), with the circular region of concentration, the 90% contour of sensitivity that is also shown in Figure 4.2C, outlined in white. Figure 4.3E displays what remains after subtracting the Slepian fit from the low-degree EGM96 geoid, s_3 shown in Figure 4.3C. Finally, Figure 4.3F shows the results of subtracting the low-degree Slepian fit (i.e., Figure 4.3D) from the full EGM96 geoid shown in Figure 4.3A. In other words, we are plotting

$$s_4 = \sum_{\alpha=1}^{10} s_\alpha\, g_\alpha, \tag{4.23}$$

$$s_5 = \sum_{\alpha=11}^{81} s_\alpha\, g_\alpha = s_3 - s_4, \text{ and} \tag{4.24}$$

$$s_6 = \sum_{\alpha=11}^{81} s_\alpha\, g_\alpha + \sum_{l=9}^{360} \sum_{m=-l}^{l} s_{lm}\, Y_{lm} = s_1 - s_4. \tag{4.25}$$

A comparison of s_2 and s_6 in Figure 4.3B and 4.3F, which are shown using the same color scale, shows the changes due to the regional subtraction of low-degree signal. These changes

include some subtle changes in geoid height such as slightly broader and larger positive anomalies in northwestern Australia, and broader negative anomalies along the southwestern coast of Australia. This comparison shows the difference between what would be the "traditional" all-spectral and the optimized "Slepian" spatio-spectral approach to removing the regional low-degree contributions to the geoid.

In conclusion, spatiospectral filtering allows us to examine the geoid in and around Australia without being biased by power in the $0 \rightarrow L$ degree range that mostly arises from regions outside of Australia. The resulting geoid anomalies from this analysis in the Australian region show a distinct feature with negative and positive anomalies of amplitude of $\sim$10 m in the southern and northern parts of Australia, respectively (Figure 4.3F). Such regional geoid anomalies are used in this study to constrain mantle viscosity structure.

4.6 3D Numerical Results

We performed calculations using the keel shown in Figure 4.2A and varied the viscosity of the asthenosphere. From the vertical normal-stress field we calculate the dynamic topography at the surface (Figure 4.4A) and at the core-mantle boundary, which is then used to calculate surface geoid anomalies (Figure 4.4B). As upper-mantle viscosity is varied, the spatial patterns of topography and the geoid remain roughly the same while the magnitude fluctuates. At the leading edge of the keel, vertical normal stresses cause positive dynamic topography at the surface while near the trailing edge of the keel the reverse is true, with negative dynamic topography at the surface. The resulting geoid anomaly is also positive at the leading edge of the keel and negative at the trailing edge. Some asymmetry also results due to the shape of the lithospheric keel.

While the example model outputs shown in Figure 4.4A–B have yet to be filtered, a similar pattern is seen to occur in the observed geoid after locally removing long wavelengths (Figure 4.3F). In both modeled and observed fields, broad positive geoid anomalies occur along the coast of northwestern Australia, and broad negative anomalies along the south-

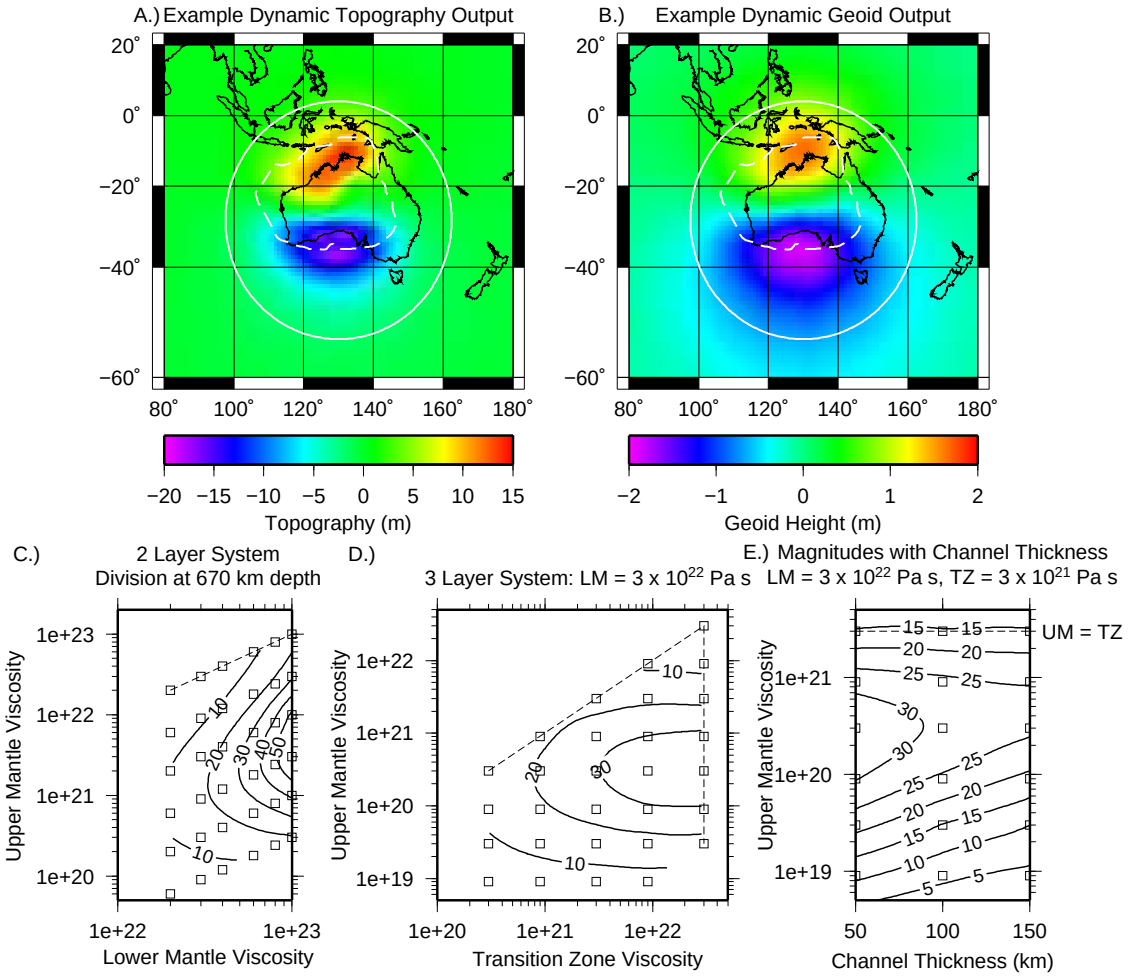

Figure 4.4: Examples of model output. (A) Example dynamic topography at the surface for a calculation with $\eta_{LM} = 3 \times 10^{22}$ Pa s, $\eta_{TZ} = 3 \times 10^{21}$ Pa s, and $\eta_{UM} = 3 \times 10^{20}$ Pa s. The colored topography anomalies are scaled to a surface velocity of 1 cm/yr. The surface velocity vector is aligned with the plate motion vector at azimuth 1.81° from North. In solid white we show the 90% contour of filter sensitivity from Figure 4.2C. In dashed white we show the outline of the Australian keel (where thickness >100 km) determined from the CUB2.0 model. (B) Example dynamic geoid anomalies at the surface from the same calculation, also scaled to 1 cm/yr of surface motion. (C–E) Contoured magnitudes of unfiltered model geoid anomalies in m, scaled to the Australian surface motion of 8.267 cm/yr. Magnitude simply represents the difference between peak minimum and maximum anomaly (i.e., no pattern information, about 3.6 m in B). Hollow squares show model individual runs. (C) Magnitudes in a two-layered mantle with division at 670 km depth. (D) Magnitudes in a three-layered mantle with divisions at 670 km and 400 km depth. Here the viscosity of the lower mantle is fixed at 3×10^{22} Pa s. Diagonal dashed line is where the upper mantle and transition zone have equal viscosity, equivalent to a two-layered mantle divided at 670 km depth. Vertical dashed line is where the transition zone and lower mantle have equal viscosity, equivalent to a two-layered mantle divided at 400 km depth. (E) Contoured magnitudes of unfiltered model geoid anomalies in m for different channel thicknesses. Lower-mantle and transition-zone viscosities are fixed at 3×10^{22} Pa s and 3×10^{21} Pa s, respectively. Horizontal dashed line shows where the upper mantle and transition zone are isoviscous.

western coast. We explore this behavior further later, but this initial observation provides context for some of our model results.

4.6.1 Two-Layered Mantle

The primary descriptor of our model results is the magnitude of the dynamic geoid anomaly. In a two-layer mantle with a division at 670 km depth (Figure 4.4C), the anomaly magnitudes vary with the thickness and viscosity of the channel below the keel. When the viscosity of the entire mantle is uniform (Figure 4.4C, dashed line), the channel below the keel is effectively very thick, and the magnitude of the dynamic geoid anomaly (Figure 4.4C) is relatively small (contours indicate the maximum geoid anomalies reached). As upper-mantle viscosity decreases, this channel effectively gets thinner as deformation concentrates in the upper mantle, and the geoid anomaly increases. This increase continues until the viscosity contrast reaches approximately 1:33 (third row of squares below dashed line). Eventually the low viscosity of the upper mantle is the dominant property, reducing stress and geoid magnitudes. This is similar to what we observed from the simple analytical models plotted in Figure 4.1B.

4.6.2 Three-Layered Mantle

In a three-layered mantle, the general results from two-layer models remain valid. For a constant lower-mantle viscosity (3×10^{22} Pa s in Figure 4.4D), when upper-mantle (<400 km depth) viscosity is reduced relative to the transition zone (between 400 and 670 km depth), geoid anomalies initially increase as more flow is concentrated in the upper mantle. As upper-mantle viscosity is decreased further, the dynamic geoid anomalies are eventually reduced as the low viscosity reduces stress magnitudes. The effect of the weak channel is also apparent here more explicitly. In Figure 4.4D, the diagonal dashed line is for an upper mantle and transition zone that have equal viscosities, which corresponds again to a two-layer system with division at 670 km depth. Alternatively, the vertical dashed line denotes

cases where the transition zone and lower mantle are isoviscous. This represents a two-layer system with division at 400 km depth. Cases near the division at 400 km generally result in larger anomaly magnitudes, except for two regions: (1) when mantle viscosity is nearly uniform (Figure 4.4D, top right) the channel is thick enough to dominate subtle changes in viscosity structure; (2) when the viscosity of the weakest layer is low (Figure 4.4D, bottom), stress magnitudes are low enough that changing channel thickness results in an insignificant change to anomaly magnitude.

4.6.3 Channel Flow

Arguably, the controlling parameter of this process is not the absolute depth of the continental keel, but the thickness of the asthenospheric channel. Different keel thicknesses can combine with regional variations in the depths of upper-mantle discontinuities to change the thickness of the asthenospheric channel below it (e.g. *Gilbert et al.*, 2001).

Accordingly, we performed calculations varying the thickness and viscosity of this channel (Figure 4.4E). Once again, we contour the maximum resulting geoid anomalies. Channel thickness is varied by adjusting the depth to the asthenosphere-transition zone viscosity contrast to examine cases with 50 km, 100 km, and 150 km between this boundary and the keel bottom, while keeping the keel thickness at 300 km. Generally, an increase in channel thickness results in a smaller geoid anomaly, as expected. This change is smaller than one might expect, however, from a single-layer model (eq. 4.4), or even a two-layered mantle (eq. 4.6; Figure 4.1), where pressure gradients are nonlinearly (e.g., cubically in uniform-viscosity mantle models) related to channel thickness. Instead, in 3D it seems likely that this nonlinearity is offset by flow that passes relatively unconstrained around the sides of the keel region.

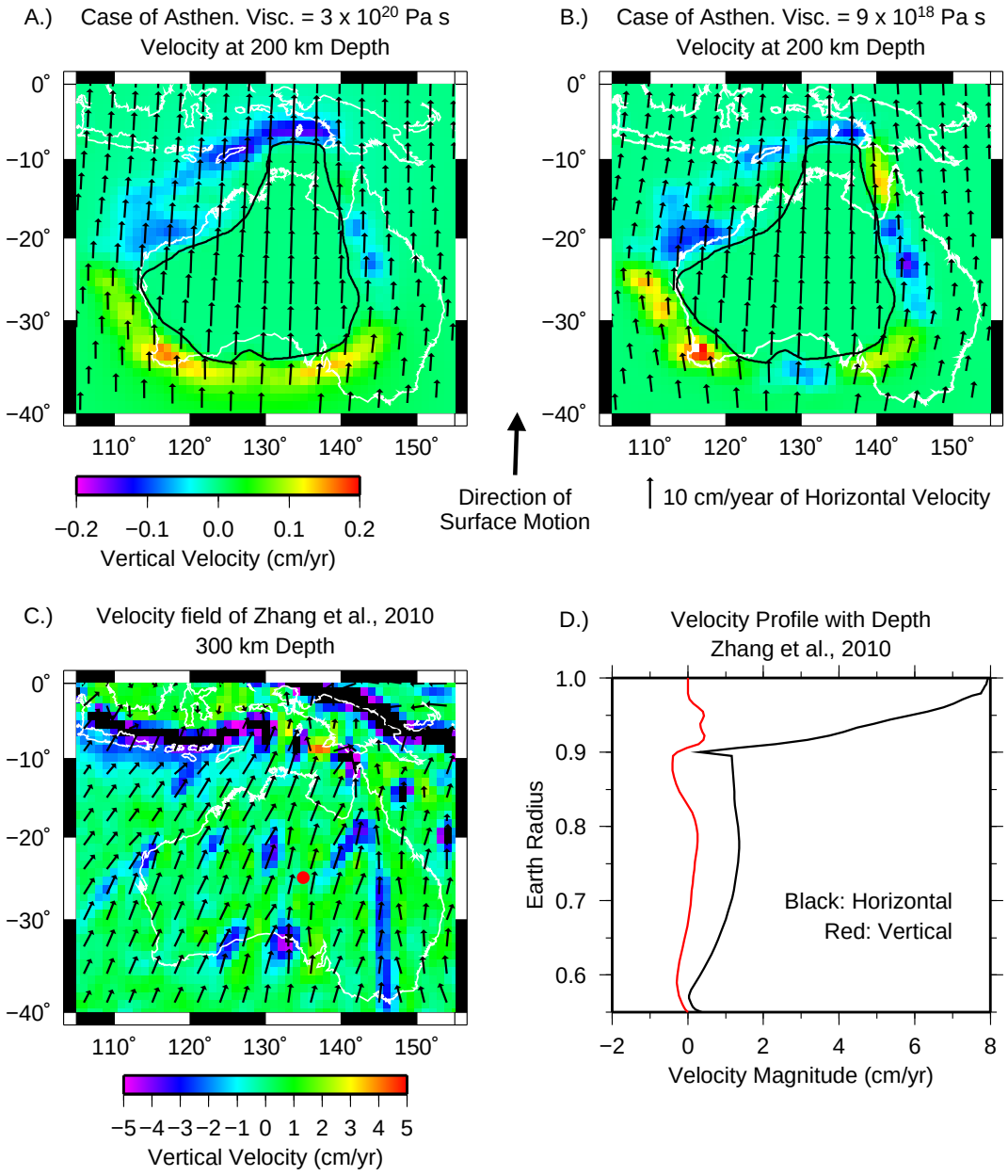

Figure 4.5: (A–B) Mantle velocity at 200 km depth for two model cases. Vectors show horizontal velocity. Colors show vertical velocity, with positive values out of the page. The 10 cm/yr scale vector for horizontal motion is valid for panels A–C. Coastlines are outlined in white. In both cases, $\eta_{LM} = 3 \times 10^{22}$ Pa s and $\eta_{TZ} = 3 \times 10^{21}$ Pa s. The depths shown are at 200 km, and the black shape outlines the Australian continental lithosphere at this depth. (A) A case with asthenospheric viscosity $\eta = 3 \times 10^{21}$ Pa s. (B) A case with asthenosphere viscosity $\eta = 9 \times 10^{18}$ Pa s. (C) Similar velocity slice at 300 km depth from a global mantle flow model of *Zhang et al.* (2010). Note the different scale for vertical velocity; magnitudes less than −5 cm/yr are black. (D) Vertical profile of velocity with depth for point in C indicated by red dot (135° E, 25° S).

4.6.4 Flow Field

As a continental keel moves through a less viscous upper mantle we might expect the mantle to deform horizontally around the sides of the keel (*Fouch et al.*, 2000) or vertically, beneath the keel. The largest expected control on this deformation is the viscosity of the asthenosphere, and hence, in Figure 4.5, we show horizontal (vectors) and vertical velocity (colors) at a depth in the asthenosphere for two of our cases, one with moderate and one with low asthenosphere viscosity. Surprisingly, both cases are fairly similar.

The case with moderate asthenospheric viscosity ($\eta = 3 \times 10^{20}$ Pa s) displays very little variation of velocity with latitude (Figure 4.5A). This case also shows downgoing velocities at the leading, and rising velocities at the trailing edge of the keel, indicating that material predominantly flows beneath the keel rather than horizontally around it.

While the case with lower asthenospheric viscosity ($\eta = 9 \times 10^{18}$ Pa s) does show variation in the plane (Figure 4.5B), with velocity vectors deflected around the keel, these discrepancies do not exceed ten degrees from the azimuth of surface motion. This second case also has vertical velocities that are similar to those in the first case, but with somewhat more variability. It is not until asthenospheric viscosity is decreased even further that flow directions start to significantly deviate from the direction of plate motion.

Since flow in the mantle could affect the net flow across the keel, or perhaps vertically beneath it, we examine the velocity field beneath Australia from a global mantle convection model (*Zhang et al.*, 2010, case FS1). The model, shown for the present day in planform in Figure 4.5C and in profile in Figure 4.5D, is the result of a time-dependent calculation and includes both prescribed surface plate-motion history and mantle buoyancy forces. The modeled horizontal motion in the mantle is broadly consistent with our own model assumptions: motion in the mantle, particularly in the high-viscosity lower mantle, is low relative to the motion at the surface and is a good representation of the net shear across the mantle. North of Australia, the vertical motion in the upper mantle is dominated by the subduction

zones that have velocity magnitudes near −8 cm/yr. Under Australia there are several small-scale downwellings below the lithosphere, which are likely due to sub-lithospheric small-scale convection aided by large plate motion (e.g. *van Hunen et al.*, 2005). Both types of vertical motion could influence the keel-induced pressure gradient, and should therefore be taken into account when making interpretations.

4.7 Geoid Comparison with Observations

To constrain the upper-mantle viscosity structure we compare the dynamic geoid from our model calculations to the Earth's observed geoid. Since our data are localized spatially as well as spectrally, and because Earth's gravitational potential receives many different contributions across the spatial and spectral domains we apply the Slepian filtering technique discussed in Section 4.5 to both model and observations before comparing them.

4.7.1 Two-Layered Mantle

We begin by comparing geoids from our two-layer models with the observed geoid. We calculate the misfit by finding the 2D absolute value of the error per measurement as

$$\text{Misfit} = \frac{1}{n}\sum_{i=1}^{n} |\text{obs}_i - \text{model}_i| \tag{4.26}$$

where obs_i is an observed geoid measurement at a specific location, model_i is a model geoid measurement at the same location, and n is the total number of values compared (which is identical in every case studied). Misfit is calculated within a subregion that includes our largest-amplitude model geoid anomalies (Figure 4.6A, dashed rectangle), excluding areas where model anomalies are low. This area covers both continental and oceanic parts of the Australian region. If we were to examine a null model, eq. 4.26 will produce a misfit that represents the inherent power of the observed field, approximately 3 m. For our cases, models with misfit values below this fit the observed field better than a null model.

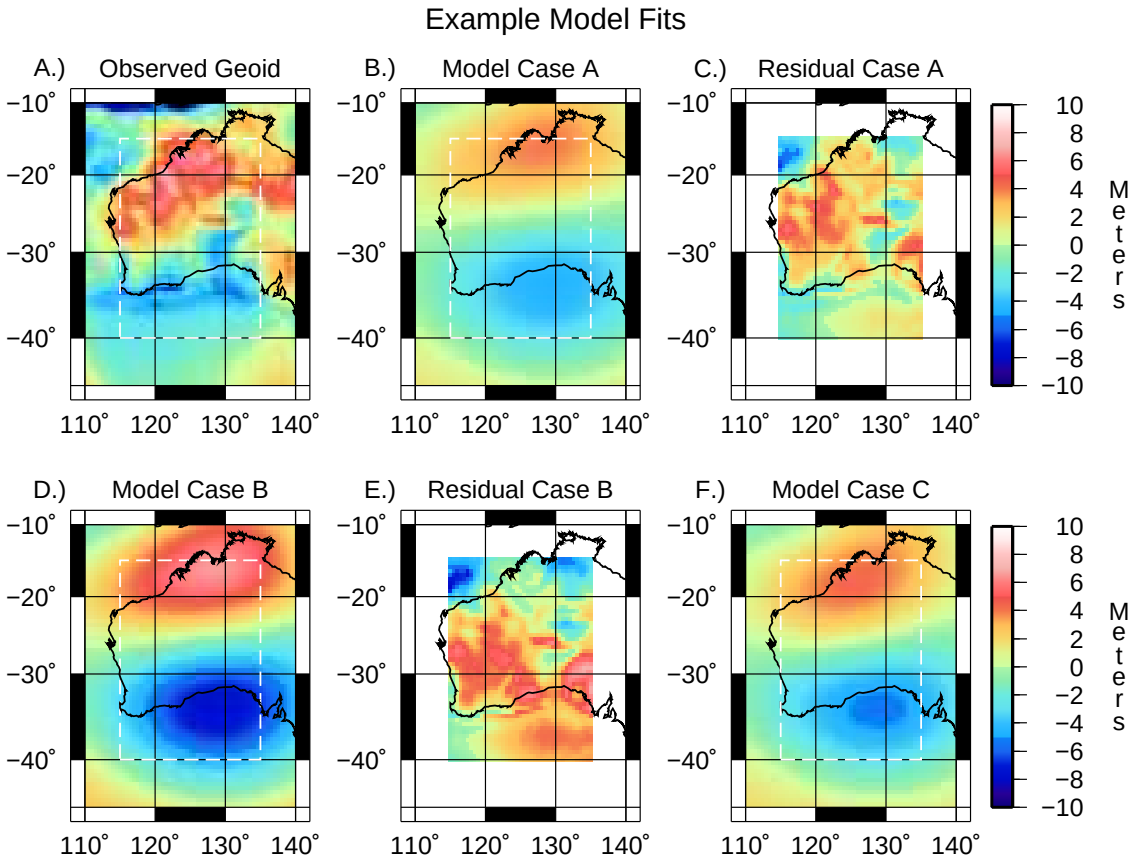

Figure 4.6: Example model fits. Example cases are denoted by red squares in Figure 4.7. Model cases A and B are for a two-layered mantle, while case C is from a three-layered mantle. Model cases are subtracted from the observed geoid field within the dashed white box, yielding the plots of residuals. The dashed white box also marks the area used for calculating misfit. All geoid fields are plotted using the same ±10 m scale. (A) Filtered observed geoid field. (B) Filtered model geoid from case A, for a two-layered mantle. (C) Residual for case A. (D) Filtered model geoid from case B, for a two-layered mantle. (E) Residual for case B. (F) Filtered model geoid from case C, for a three-layered mantle. This example is similar to case A, and a residual is not shown.

When inspecting misfit for a two-layered mantle (Figure 4.7A), three scenarios emerge. First, a model that produces minimal dynamic geoid anomalies, such as a uniform mantle of viscosity 2×10^{22} Pa s, will produce a misfit around 3 m. Second, a model that reproduces the observed field results in a minimum misfit. This can be seen in model case A in Figures 4.6B–C, whose residuals remain fairly uniform from north to south and have small amplitudes. Finally, a model that produces very large geoid anomalies will overshoot the apparent signal

in the observed field (model case B in Figures 4.6D–E). While the average magnitude of this misfit is of the same order as that from a model with null signal, upon inspection it is clear that the positive-negative north-south signature of the residual has reversed.

The misfit for a two-layered mantle reaches an absolute minimum when the lower-mantle viscosity $\eta_{LM} = 5.3 \times 10^{22}$ Pa s and the upper-mantle viscosity is about 20 times smaller, $\eta_{UM} = 2.75 \times 10^{21}$ Pa s. It is clear from Figure 4.7A, though, that there is a broad region with misfits near the minimum where models can be considered acceptable. The trade-off between effective channel thickness and upper-mantle viscosity implies that models with viscosity increases from the upper to the lower mantle with ratios between 3 and 300 could be considered supported by the data. In a two-layered mantle, the viscosity jump between the upper and lower mantle cannot therefore be sufficiently constrained.

4.7.2 Three-Layered Mantle

In a three-layered mantle, we fix lower-mantle viscosity and plot how misfit varies for different viscosities of the upper mantle and transition zone (Figures 4.7B–C). As described earlier, when a weak upper-mantle layer is introduced, dynamic geoid anomalies can increase. Here, this means that we should expect more variation in the pattern of misfit depending on the viscosity structure.

When lower-mantle viscosity is 2×10^{22} Pa s (Figure 4.7B), the dynamic geoid anomalies generally have low magnitudes. The minimum misfit suggests a structure that maximizes the dynamic geoid signal. Thus a structure with an upper-mantle viscosity of 1–2×10^{20} Pa s (about 100 times weaker than the lower mantle) and a transition-zone viscosity of 3–10 $\times$ 10^{21} Pa s is preferred.

At lower-mantle viscosities higher than 2×10^{22} Pa s, overall anomaly magnitudes increase, e.g. to the values already shown in Figure 4.4D, and the misfit pattern becomes more intricate (Figure 4.7C). Regions of lowest misfit generally occur when $\eta_{UM} < 10^{20}$ Pa s. For the cases shown where $\eta_{LM} = 3 \times 10^{22}$ Pa s, the absolute minimum misfit occurs when

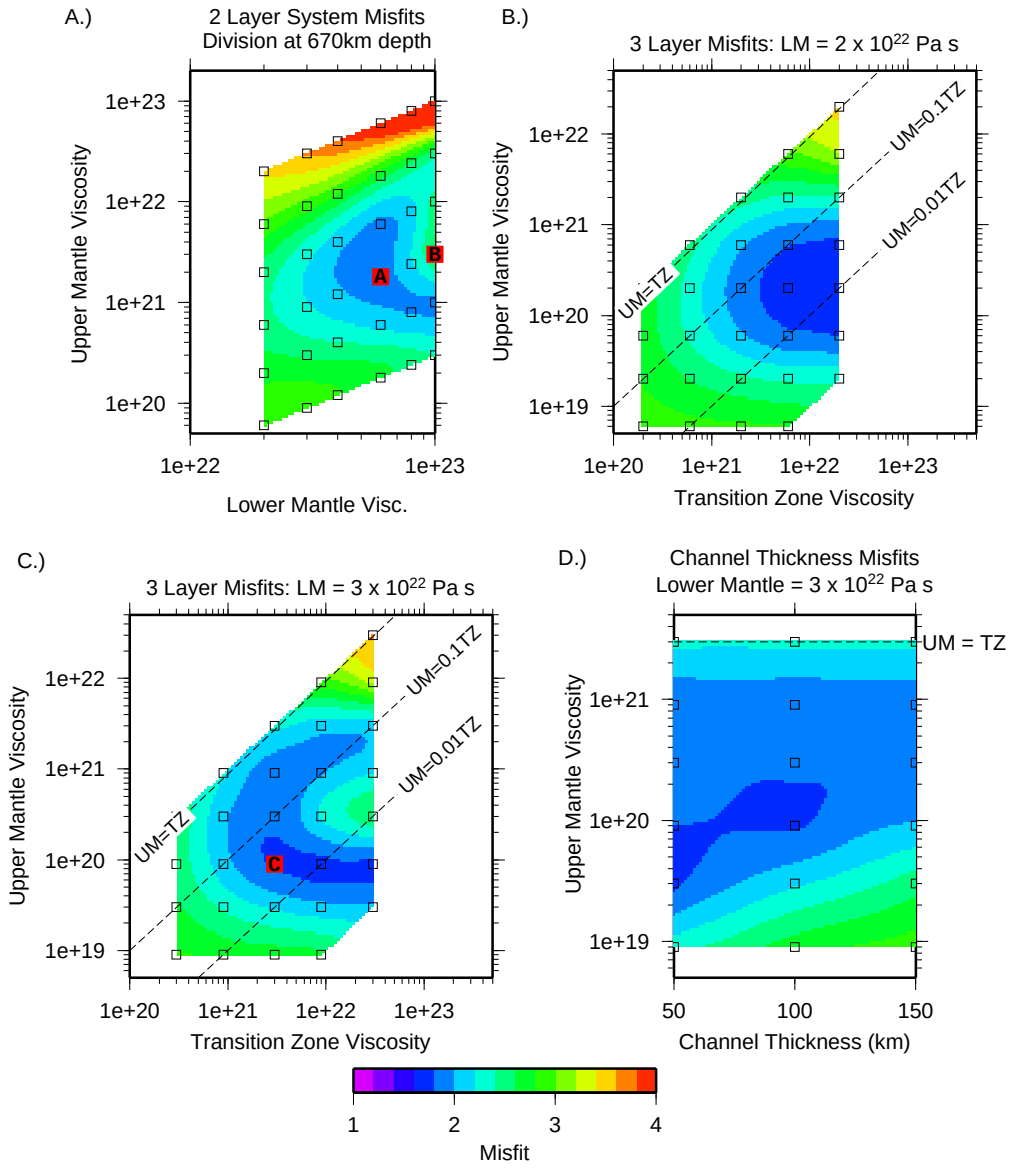

Figure 4.7: Color-shaded images of misfit between filtered model cases and observed geoid. Hollow squares identify model runs. The background observed geoid field has a mean power of about 3.1 m. Therefore the misfit between the observed field and a model with no (zero) geoid anomaly would be about 3.1 m. This occurs when upper-mantle viscosity is very low ($<10^{19}$ Pa s). Other instances of misfit about 3.1 m occur when model signal is roughly twice the power (i.e. the model signal overshoots the observed signal, resulting in a residual with power equivalent to the original observed field). A.) Model misfits for a two-layered mantle with division at 670 km depth. Red squares A and B denote cases shown in Figure 4.6. B.) Model misfits for a three-layer mantle with lower-mantle viscosity held fixed at 2×10^{22} Pa s. C.) Model misfits for a three-layer mantle with lower mantle viscosity fixed at 3×10^{22} Pa s. Red square denotes case C shown in Figure 4.6. D.) Model misfits for a three-layered mantle for varying channel thicknesses. Channel thickness is determined by varying the depth to the upper mantle-transition zone viscosity discontinuity. Lower-mantle and transition-zone viscosities are fixed at 3×10^{22} Pa s and 3×10^{21} Pa s, respectively. Dashed line indicates where the upper mantle and transition zone are isoviscous.

$\eta_{TZ} = 2.7 \times 10^{22}$ Pa s and $\eta_{UM} = 7.9 \times 10^{19}$ Pa s, but the region of misfits near this minimum is in fact quite broad. If we examine only the cases with misfits <1.8 m (the darkest shades of blue in Figure 4.7C), we can make some interesting further observations about the best-fitting viscosity structure. In each of these cases there is a factor of ∼300 between the viscosities of the lower and upper mantle. Meanwhile, the viscosity of the transition zone varies over an order of magnitude, indicating that it is less important once the upper mantle is sufficiently weak. We show such a model case with three layers that has a low misfit (<1.8 m, see Figure 4.7C) in Figure 4.6F (model case C). While the pattern of the model signals remains fairly consistent between the two and three-layered cases, the changes in amplitude cause the best fits to shift to lower upper-mantle viscosities.

Finally, we examine the effects of the thickness of the asthenospheric channel on the model geoid using a set of calculations in which asthenospheric viscosity and channel thickness are varied while transition-zone and lower-mantle viscosities are fixed at 3×10^{21} Pa s and 3×10^{22} Pa s, respectively (Figure 4.7D). The misfit in these models is less sensitive to asthenospheric channel thickness than one might expect from the single-layer analysis (eq. 4.4). This confirms the finding that lateral flow of mantle material around the sides of lithospheric keels plays a role in the upper mantle.

4.8 Discussion

4.8.1 Constraints on Mantle Viscosity Structure

Two classic methods to study mantle viscosity make use of observations associated with post-glacial rebound, and long-wavelength geoid anomalies. Generally, in studies of post-glacial rebound, the Earth's response to surface loads is modeled and fit to observations such as relative sea-level histories (*Peltier*, 1976; *Wu and Peltier*, 1982; *Mitrovica*, 1996; *Simons and Hager*, 1997; *Peltier*, 1998; *Mitrovica et al.*, 2007) or time-varying gravity anomalies from the Gravity Recovery and Climate Experiment (GRACE) (*Paulson et al.*, 2007a; *Tamisiea*

et al., 2007). In some long-wavelength studies, geoid anomalies from the mantle's internal density variations, which depend on the viscosity structure, are compared to the observed geoid (e.g. *Hager and Richards*, 1989). While studies of long-wavelength geoid anomalies have suggested a lower mantle that is significantly more viscous than the upper mantle (e.g. *Hager*, 1984; *Ricard et al.*, 1984; *Hager and Richards*, 1989), the results of post-glacial rebound studies are not always consistent among themselves, with some suggesting a more uniform mantle viscosity (e.g. *Peltier*, 1998), and others also arguing for a lower mantle that is significantly stronger than the upper mantle (e.g. *Lambeck et al.*, 1990; *Han and Wahr*, 1995; *Simons and Hager*, 1997; *Mitrovica and Forte*, 2004). Using relative sea-level change and GRACE time-varying gravity data, *Paulson et al.* (2007a,b) recently showed that the inconsistency among the post-glacial rebound studies owes to the poor depth resolution of the observations. In particular, *Paulson et al.* (2007a) showed that if the mantle is divided into two layers with division at 670 km depth, viscosity models that have $\sim 5 \times 10^{19}$ Pa s and $\sim 5 \times 10^{22}$ Pa s for the upper and lower mantle, respectively, produce fits to both data types that are similar to those of a viscosity model with 5.3×10^{20} Pa s for the upper and 2.3×10^{21} Pa s for the lower mantle.

The main objective of this study has been to seek additional constraints on upper-mantle viscosity by examining the gravity anomalies caused by the pressure difference associated with moving Australian continental lithosphere, a thick keel plowing through the mantle. Our study therefore represents a new method to constrain the viscosity structure of the mantle. We found that modeled geoid anomalies caused by a moving continental lithosphere with a keel show remarkable similarities to the observations, with negative and positive geoid anomalies in southern and northern Australia, respectively. Assuming that such geoid anomalies are indeed caused by the pressure difference induced by the keel's motion, we have shown that geoid anomalies, when properly filtered to account for localized, long-wavelength effects, can provide useful constraints on mantle viscosity.

If the mantle is divided at 670 km depth into two layers, the geoid in Australia is

best explained by a mantle viscosity structure with 2.75×10^{21} Pa s and 5.3×10^{22} Pa s for the upper mantle, and lower mantle, respectively — a factor of 20 increase. However, this viscosity structure does not appear to be consistent with the relative sea-level and GRACE data as shown by *Paulson et al.* (2007a). This difficulty can be resolved by introducing an additional layer or weak asthenosphere from the base of the lithosphere to 400 km depth. We found that such a weak asthenosphere tends to amplify the effects of a continental keel. With our three-layer models, and fixing lower-mantle viscosity to values between 2–3×10^{22} Pa s, we found that upper-mantle viscosity (i.e., above 400 km depth) needs to be $\sim 10^{20}$ Pa s, or $\sim$300 times weaker than the lower mantle, in order to reproduce the geoid anomalies in Australia. Interestingly, this viscosity structure is generally permissible by the relative sea-level and GRACE data, as shown by *Paulson et al.* (2007a). However, our result depends on the magnitude of lower-mantle viscosity. If the lower mantle is too weak (10^{22} Pa s or less), the geoid produced by the keel is too small to explain the observations. Therefore, our study suggests that future geodynamics studies (e.g. on mantle structure, heat transfer, and mantle mixing) and mantle rheology should consider the possibility of relatively high lower-mantle viscosity of 2–3×10^{22} Pa s.

Recently, *Conrad and Behn* (2010) used seismic anisotropy and lithospheric net rotation to constrain model viscosities for the asthenosphere (down to 300 km depth in their models) and the transition zone (between 300 km and 670 km depths) to be 0.5–1×10^{20} Pa s and 0.5–1×10^{21} Pa s, respectively, while the lower-mantle viscosity is fixed at 5×10^{22} Pa s. Considering the difference between our models in dividing the viscosity layers, the viscosities for the upper mantle above 670 km depth from our study are quite similar to those of *Conrad and Behn* (2010). However, these authors did not explore the dependence of their models on lower-mantle viscosity.

4.8.2 Relevance to Other Continental Keels

The first-order controls on upper-mantle pressure gradients in our calculations are the viscosity structure of the mantle and the magnitude of surface velocity. In addition to these primary controls, a set of secondary factors can influence the dynamic topography at the surface to a lesser extent. Our calculations are for a fixed keel size. If the length of the keel is increased (in the direction of surface motion) then the distance between positive and negative dynamic topography will increase, and more power of the geoid anomaly will be at longer wavelengths. If the keel's width is increased (perpendicular to surface motion) then dynamic anomalies widen as well. In this instance magnitudes of dynamic topography will also be larger since a wider keel displaces more mantle as it moves.

One of the unique features of the Australian keel is its asymmetry in the direction of surface motion (Figure 4.2A). From the thickest part of the lithosphere (at about 130° longitude) to the east, the lithosphere quickly thins, coincidently with the decrease in crustal age (*Simons and van der Hilst*, 2002). To the west this transition is more gradual and tends to follow the boundary between continental and oceanic crust (along the western coast). The effect of this asymmetry is most easily seen in the positive dynamic topography at the leading edge of the keel (Figure 4.4A). Such a shape in other keels could result in unique dynamic geoid anomalies. A unique geoidal pattern would help distinguish pressure-induced anomalies from other processes that could be acting on keel edges such as small-scale or edge-driven convection (e.g. *King and Ritsema*, 2000; *Conrad et al.*, 2010).

Several cratonic regions, such as North America, western Africa, and Siberia (*Artemieva*, 2009), have lithospheric keels as thick as Australia (>250 km). If keel-induced pressure effects could be observed for these regions this could provide additional constraints on mantle viscosity. Each of these regions has relatively slow surface motion that could make it difficult, however, to detect dynamic signals as we did in our analysis. We performed our analysis for Australia because its large surface motion makes it the most likely to show these effects.

The keels in western Africa and Siberia have surface speeds below about 2 cm/yr (*Gripp and Gordon*, 2002), so to first order the geoidal anomalies would have much reduced magnitude. While also having low surface speeds of roughly 3 cm/yr, the North American keel could still have detectable anomalies due to its larger keel size.

4.8.3 Seismic Anisotropy

Viscous deformation in the upper mantle is dominated by the rheology of its most dominant mineral, olivine (*Karato and Wu*, 1993). This deformation aligns elastically anisotropic olivine crystals (e.g. *Verma*, 1960) in a lattice-preferred orientation (*McKenzie*, 1979; *Ribe*, 1989) in the upper mantle, an effect that is regularly studied seismologically (e.g. *Hess*, 1964; *Forsyth*, 1975; *Long and Silver*, 2009). Because of this relationship, observations of seismic anisotropy can be used to constrain geodynamic models of mantle flow (e.g. *Conrad et al.*, 2007). In practice, complexities such as the strain history (e.g. *Ribe*, 1992), "frozen" lithospheric anisotropy (e.g. *Silver*, 1996; *Savage*, 1999; *Silver et al.*, 2001), the presence of water (*Jung and Karato*, 2001), grain-boundary effects (e.g. *Zhang and Karato*, 1995), and so on, mean that such constraints are fraught with uncertainty (e.g. *Savage*, 1999; *Kaminski and Ribe*, 2001; *Becker et al.*, 2006). However, the first-order approach of inferring from the direction of seismic anisotropy the direction of mantle flow has been fruitful, elucidating, for example, patterns of flow around hot spots or underneath oceanic plates (e.g. *Becker et al.*, 2003; *Behn et al.*, 2004; *Walker et al.*, 2005).

Our own results for Australia can be brought to bear on this relationship, by examining our instantaneous flow-field velocities in the context of published regional studies of seismic anisotropy, recently summarized by *Fouch and Rondenay* (2006). Generally, body-wave measurements made at seismic stations correlate with the large-scale structure at the surface, suggesting strong lithospheric anisotropy (*Fouch and Rondenay*, 2006). Surface-wave analyses, which provide better constraints on the variation of anisotropy with depth, have been conducted throughout the Australian continent in the past decade (e.g. *Debayle*,

1999; *Debayle and Kennett*, 2000a,b; *Simons et al.*, 2002, 2003; *Debayle et al.*, 2005). Australia and North America have both been found to have significant (about 2%) azimuthal anisotropy at or below 200 km depth (e.g. *Debayle et al.*, 2005; *Marone and Romanowicz*, 2007). This deep anisotropy (below 150 km) mostly correlates with present-day plate motion (e.g. *Simons et al.*, 2002; *Simons and van der Hilst*, 2003; *Debayle et al.*, 2005).

As mentioned earlier, we might expect mantle flow to deflect around a continental keel. Based on the pattern of observed shear-wave splitting measurements, *Fouch et al.* (2000) have suggested this is the case in North America. At depths of 150 km, *Debayle and Kennett* (2000a) found that anisotropy in western and central Australia aligns with north-south plate motion while eastern Australia displays azimuthal anisotropy that appears to follow the craton boundary. However, deformation akin to that suggested by the anisotropy does not occur in our models unless asthenospheric viscosity is very low ($<9\times10^{18}$ Pa s). Our results agree with the large majority of anisotropy measurements at these depths that align in the direction of surface plate motion (e.g. *Debayle and Kennett*, 2000b; *Simons et al.*, 2003; *Debayle et al.*, 2005), and suggests that return flow occurring beneath the keel is important.

4.9 Conclusions

When continental keels are driven by imposed surface motion, pressure perturbations cause positive dynamic topography at the leading edge, and negative dynamic topography around the trailing edge of the keel. Depending on the viscosity structure of the mantle, this dynamic topography can be on the order of $\pm$100 m and the corresponding geoid anomalies can be on the order of $\pm$10 m.

When filtered to remove localized long-wavelength anomalies using a technique developed using Slepian functions, the Australian geoid clearly displays the expected pattern, with positive and negative anomalies of about 10 m amplitude at the leading and trailing edges of the craton, respectively. Our model results agree with the observations: assuming

that the signal is indeed caused by the dynamic motion of the keel, we are able to obtain constraints on the mantle viscosity structure below the continent.

Dynamic topography produced by motion of a continental keel depends strongly on the effective thickness and viscosity of the asthenosphere, where most of the horizontal motion occurs. For a two-layered mantle with a division at 670 km, decreasing upper-mantle viscosity can increase dynamic topography if viscosities are large enough. The minimum misfit between the modeled and observed geoid occurs when $\eta_{LM} = 5.3 \times 10^{22}$ Pa s and $\eta_{UM} = 2.75 \times 10^{21}$ Pa s. However, these viscosities appear too large compared with post-glacial rebound studies. This suggests that radial mantle viscosity variations are not fully captured by two-layer models.

In a three-layer mantle, misfit patterns become more complex as lower-mantle viscosity is increased. For a lower-mantle viscosity $\eta_{LM} = 3 \times 10^{22}$ Pa s, the minimum misfit occurs when the upper-mantle viscosity $\eta_{UM} = 7\text{–}10 \times 10^{19}$ Pa s, a factor of about 300 smaller than that of the lower mantle, while the transition-zone viscosity η_{TZ} may vary between 10^{21}–10^{22} Pa s. Such a viscosity structure is not inconsistent with post-glacial rebound studies. Since our results are sensititive to lower-mantle viscosity, they also suggest that a relatively high lower-mantle viscosity should be considered in future geodynamic studies.

4.10 Acknowledgments

This research was supported by the David and Lucile Packard Foundation and the National Science Foundation. We thank Nan Zhang for providing the data presented in Figures 4.5C–D. Helpful reviews by Clint Conrad and Scott King improved the clarity and quality of this work. Figures were created with the GMT software (*Wessel and Smith*, 1998). The Slepian analysis routines are available on `www.frederik.net`.

A	Area of geographical region of interest
$D_{lm,l'm'}$	Spatiospectral localization kernel
d	Thickness of the lower mantle
d'	Dimensionless thickness of the lower mantle
F	Location far from keel for analytical treatment
g_α	Slepian basis function on the unit sphere
$g_{\alpha\,lm}$	Spherical-harmonic coefficients of the Slepian function g_α
h_0	Thickness of the upper mantle
h	Thickness of the low-viscosity channel
h'	Dimensionless thickness of the low-viscosity channel
K	Location under keel for analytical treatment
k	Thickness difference between keel and surrounding lithosphere, $(h_0 - h)$
k'	Dimensionless thickness difference between keel and surrounding lithosphere
L	Degree of bandlimit of geophysical signal
$L_{\max}$	Maximum degree of expansion of geophysical signal
l	Degree of spherical harmonic
m	Order of spherical harmonic
N	Spherical Shannon number
n	Number of observations compared in misfit calculation
p	Pressure
p'	Dimensionless pressure
R	Spatial region of interest
s	Scalar geophysical function on the unit sphere
s_{lm}	Spherical-harmonic coefficients of the function s
s_α	Slepian-basis coefficients of the function s
u	Horizontal component of velocity
$\mathbf{v}$	Velocity vector
x	Horizontal coordinate
x'	Dimensionless horizontal coordinate
Y_{lm}	Spherical harmonic on the unit sphere
z	Vertical coordinate
η	Viscosity (Newtonian)
η_{UM}	Viscosity of the upper mantle
η_{TZ}	Viscosity of the transition zone
η_{LM}	Viscosity of the lower mantle
γ	Ratio of viscosities between mantle layers
λ	Slepian eigenvalues, or the fraction of signal energy concentrated locally
Ω	Unit sphere
ϕ	Longitude
τ	Shear stress
Θ	Colatitudinal radius of the region of interest
θ_0	Colatitude

Table 4.1: Definition of symbols used in this study.

Chapter 5

Viscous bending of subducted slabs

5.1 Introduction

At subduction zones oceanic lithosphere sinks into the mantle, recycling the material created previously at spreading centers. The frequent seismicity and magmatism at subduction zones have illuminated the shape of most subducting plates (*England et al.*, 2004). In some regions, such as Peru, central Chile, and Mexico, subducted plates descend into the Earth at shallow angles of less than 15 degrees. In other subduction zones, such as New Hebrides and Marianas, plates descend more steeply at dip angles greater than 60 degrees. It is clear that this dip angle of subduction is closely related to the deformation at the surface (e.g. *Barazangi and Isacks*, 1976; *Jordan et al.*, 1983; *Allmendinger et al.*, 1997), as shallow angle subduction zones are often used to explain mountain building events and volcanic patterns, such as currently in the central Andes and during Laramide time in the western United States. Less clear, however, are the reasons behind shallow or steeply dipping plate shapes (*Lallemand et al.*, 2005).

A widely used model for understanding subduction has been to assume that plate geometry is the result of steady state processes. Deformation and stresses within the mantle can then be inferred as an application of fluid mechanics corner flow (i.e., a kinematic model) (*McKenzie*, 1969; *Batchelor*, 2000). Many authors have used this method to study the dips of subducting plates (e.g. *Tovish et al.*, 1978; *Stevenson and Turner*, 1977). In kinematic models, the subducting plate is considered rigid and the negative pressure in the corner on

the arc side of the trench (and positive pressure in the corner on the oceanic side of the trench) resulting from the flow field functions as an applied torque acting to shallow the slab. These torques can be balanced by the negative buoyancy of the slab to determine which dips are stable to motion (*Tovish et al.*, 1978; *Stevenson and Turner*, 1977). This corner flow model has also been used to study the stresses in the wedge and at the base of the overriding lithosphere (*McKenzie*, 1969), seismic anisotropy resulting from flow within the mantle wedge (*McKenzie*, 1979; *Kneller et al.*, 2005), and the implied temperature field as it relates to melting (e.g. *Spiegelman and McKenzie*, 1987; *Davies and Stevenson*, 1992). Significantly, this subduction model is often used as a basis for data interpretation.

Although kinematic models of subduction are very informative of the basic physics, the assumption of a steady state subduction process is likely inappropriate when many studies indicate time dependent slab behavior (e.g. *Tao and O'Connell*, 1993; *Becker et al.*, 1999; *Billen and Hirth*, 2007; *Billen*, 2008) and more complex mantle flow in subduction zones than the corner flow solution indicates (e.g. *Russo and Silver*, 1994; *Smith et al.*, 2001; *Long and Silver*, 2008; *Jadamec and Billen*, 2010). Experiments and models that consider subduction as a dynamic time dependent process account for the internal deformation and buoyancy of slabs (e.g. *Ribe*, 2001), and are hence more complete. In dynamic subduction models it has long been clear that slabs tend to sink downward (e.g. *Sleep*, 1975) and accounting for shallow dipping slabs is difficult. Dynamic studies examining very shallow or flat subduction usually appeal to outside factors, such as subduction of less dense oceanic plateaus, positively buoyant aseismic ridges, or changes in overriding plate motion, to account for these dip angles (e.g. *Jarrard*, 1986; *Zhong and Gurnis*, 1995; *Christensen*, 1996; *Liu et al.*, 2010).

In this paper we address the relationship between kinematic and dynamic subduction models. We examine the inconsistencies between these models concerning the dip of subducting slabs. Using a torque balance for viscously deforming slabs we examine the stresses acting on the slab and test an approximation that they deform by bending of a thin viscous sheet to loads applied to the slab surface. We compare this approximation to numerical

results, and discuss the implications for maintaining the dip angle of subducted slabs.

5.2 Model Setup

We examine Stokes flow in a 2D incompressible medium. This process is governed by two of the conservation equations of viscous fluids, those for the mass and momentum,

$$\boldsymbol{\nabla} \cdot \mathbf{v} = 0, \tag{5.1}$$

$$-\boldsymbol{\nabla} P + \boldsymbol{\nabla} \cdot [\eta(\boldsymbol{\nabla}\mathbf{v} + \boldsymbol{\nabla}^{\mathrm{T}}\mathbf{v})] = \delta\rho g \hat{\mathbf{z}} \tag{5.2}$$

where $\mathbf{v}, P$, and η are the velocity, pressure, and viscosity, respectively. $\delta\rho$ is the dimensionless density difference ($\delta\rho = \Delta\rho/\rho_0$ where $\Delta\rho$ is dimensional density and ρ_0 is our reference value of density), g is gravitational acceleration, and $\hat{\mathbf{z}}$ is the vertical unit vector. The governing equations are solved with the finite element code Citcom (*Moresi et al.*, 1996). Model geometry and resolution are case dependent and are described further below. Velocities presented below are rendered dimensionless as $\tilde{w} = w\frac{\eta_m}{\delta\rho g D^2}$, where η_m is the viscosity of the mantle, and D is the depth of the model box that is also used to nondimensionalize spatial coordinates (D is chosen to be 2000 km later in this paper when the results are presented in dimensional numbers).

In this paper we analyze calculations from both kinematic models, which use velocity boundary conditions, and dynamic models, which use different boundary conditions and negative buoyancy within the slab. We also perform a simpler set of dynamic cases with Citcom to compare to a viscous bending approximation. The boundary conditions vary between cases, and are described further in the results section.

The inherent assumption of steady state corner flow in subduction zones is likely inaccurate. When this assumption is used to infer other quantities such as preferential subduction dip, it can imply other inaccurate assumptions. For instance, balancing the torques on a subducted slab while requiring only slab parallel velocity essentially approximates the slab

as perfectly rigid. A dynamic approach would be to approximate a subducted slab consistent with its viscous rheology, and then make inferences about the flow field which is not necessarily slab parallel.

For our later comparisons we use an approximation where the slab deforms by viscous bending from loads applied to its surface. By comparing this bending model with numerical models from Citcom we can examine the conditions when slab bending is applicable to subduction, and understand an intermediate step between kinematic models and very realistic dynamic models. In viscous bending the slab, which is fixed at one end with zero velocity normal to its surface, deforms dynamically balancing the internal buoyancy with stresses on its surface, such as from the pressure in the arc corner (*Houseman and Gubbins*, 1997). Our bending model is a special case of the problem examined by *Ribe* (2001). The author derived the coupled bending and stretching deformation of a thin viscous sheet from arbitrary loads. When the thin sheet has zero curvature, as in our calculations, the governing equations (equations 4.11a,b and more specifically for buoyancy equations 7.6a,b in *Ribe* (2001)) are no longer coupled between bending and stretching modes. They reduce to a much simpler form, which we rewrite the slab normal component as

$$\frac{\eta h^3}{3}\frac{\partial^4 w'}{\partial x'^4} = P^- - P^+ + \sigma^+_{z'z'} - \sigma^-_{z'z'} - hg\delta\rho\cos\alpha, \tag{5.3}$$

where η is slab viscosity, h is slab thickness, w' is slab normal velocity, x' is distance along slab, and α is slab dip. This biharmonic equation represents the motion of the slab normal to its surface, $w'(x)$, as it deforms by shearing on planes normal to its surface, from the loads on the right hand side. $P^{\pm}$ is the pressure above (+) and below (−) the slab, $\sigma^{\pm}_{z'z'}$ is the viscous deviatoric normal stress on the slab surface, and $hg\delta\rho\cos\alpha$ is the buoyancy, all of which are loads applied to the slab and are functions of x'. We use primes to distinguish the coordinate system where x' is parallel to the slab surface and z' is perpendicular to the slab surface. The viscous deviatoric stress normal to the slab surface is calculated by multiplying

the slab normal $\mathbf{n} = [\sin(\alpha), \cos(\alpha)]$ with the stress tensor as

$$\sigma_{z'z'} = 2n_x n_z \sigma_{xz} + n_x n_x \sigma_{xx} + n_z n_z \sigma_{zz}. \tag{5.4}$$

We solve equation 5.3 for w' at regularly spaced intervals along the slab by using a forward finite difference method. In the bending problem the slab has one fixed end and one free end. When solving equation 5.3 we use the boundary conditions that velocity and its slope are zero at the fixed end ($w' = \partial w'/\partial x' = 0$ at $x = 0$) and the moment and shear are zero at the free end ($\partial^2 w'/\partial x'^2 = \partial^3 w'/\partial x'^3 = 0$ at $x = L$, the slab end). For a uniform load problem (i.e., the right hand side of equation 5.3 is constant), our code reproduces the analytical solutions by *Turcotte and Schubert* (2002). Here we wish to point out that our slab bending problem differs from that considered by *Conrad and Hager* (1999) in that we are interested in bending of the entire slab and its control on slab dip, while *Conrad and Hager* (1999) were interested in slab bending at shallow depths and its controls on plate motion (also *Becker et al.* (1999)).

We perform comparable calculations in Citcom, to compare to the approximation, using an altered nodal mesh to solve the Stokes problem near the slab more accurately. In the lower portion of the model domain, below the subducting slab, the mesh is regularly spaced and element boundaries form right angles. In the upper part of the model domain, at the depths of subducted slab, we use a slanted nodal mesh similar to *Zhong and Gurnis* (1995). The region within and immediately surrounding the slab has a mesh with a constant angle of slant and regular spacing. Outside of this region the slant of the mesh incrementally adjusts so that element boundaries are perpendicular at the sides of the model domain. With this setup, the surfaces of the subducting slab lie on rows of mesh nodes allowing for accurate determination of slab buoyancy, viscous stresses, and pressure on the slab surfaces. Slabs are fixed to the top boundary of the model domain, which has a velocity boundary condition set to zero. The remaining box boundaries are shear stress free conditions (sliding).

To compare our Citcom results to the bending model, we sample the dynamic pressure and viscous deviatoric stress loads above and below the slab from our Citcom calculations and use them in equation 5.3. Negative pressure above the slab and positive pressure below the slab act as 'shallowing' loads while the negative buoyancy within the slab acts to steepen its dip. This sense is reversed for viscous stresses. These combined loads in equation 5.3 give a slab normal velocity which can be compared to the normal velocity from our numerical results. We use straight slabs that are 1000km in length, and vary the thickness, dip, and viscosity contrast between the slab and ambient mantle.

5.3 Results

5.3.1 Kinematic Conditions vs. Buoyancy Driven Flow

We initially compute a kinematic reference case of cornerflow in a subduction wedge, using Citcom and compare the results to previous numerical results and analytical solutions (figure 5.1). Our case design is similar to the benchmark cases of *van Keken et al.* (2007), and addresses the ability of Citcom's iterative solver method to solve kinematically constrained problems. Several differences, however, preclude a direct comparison of reported pressure and pressure derivative values.

The model domain consists of the area in figure 5.1a to the right of the slab interface (line from (0,1) to (1,0)). Within this space we use a mesh with 192 elements by 192 elements. This results in a non-square nodal mesh with finer resolution at $z = 0$ than at $z = 1$, but allows the slab interface to align along element boundaries. The boundary conditions for the wedge are as in the cornerflow solution of *Batchelor* (2000). The top surface at $z = 1$ has a fixed (equal to zero) velocity boundary condition. The slab interface, which dips at 45 degrees, descends with a slab parallel dimensionless speed of one. The remaining boundaries of the wedge have velocities prescribed from the *Batchelor* (2000) solution (i.e, prescribed velocities along all the boundaries). We then solve the instantaneous Stokes solution within

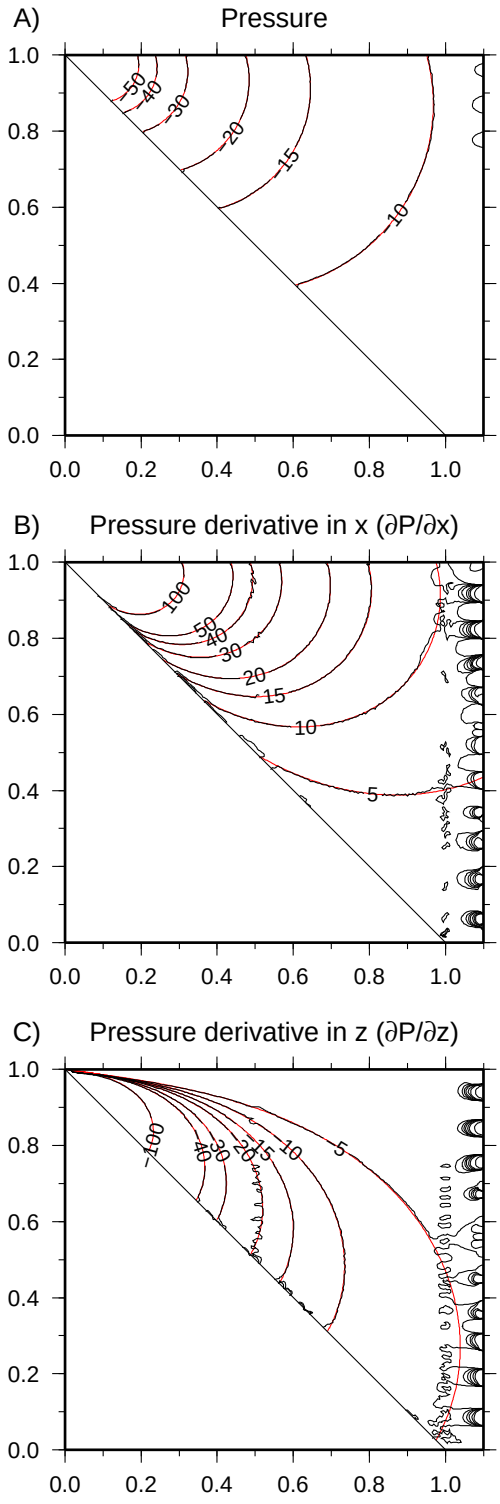

Figure 5.1: Model results (black lines) and analytical solutions (red lines) for (A) pressure, (B) pressure derivatives in the x direction, and (C) pressure derivatives in the z direction of a benchmark case with prescribed velocity boundary conditions. Additional unlabeled contour lines appear on the right boundaries where the numerical case does not reproduce the analytical solution.

the wedge using Citcom, and directly compare the results to the analytical solutions for pressure and pressure derivatives (Figure 5.1).

Citcom uses a lower order function to solve for pressure than is used for velocity. In 2D, the shape function for pressure is constant for each element while the function for velocity is linear. In this type of formulation pressure is inherently discontinuous across element boundaries, and can be prone to oscillations (i.e, checker-board pattern), especially when non-zero velocity boundary conditions are used (*Hughes*, 2000). Normally, smoothing techniques are sufficient to remove pressure oscillations. In Figure 5.1, however, numerical problems can be easily seen, more so in the derivatives of pressure, on the right side boundary with prescribed flow-through conditions (figure 5.1b and c). We can calculate the misfit between model and analytical solutions for the region $x <= 0.6$ (i.e., near the corner where the pressure and its variations are most significant) as $\sum |analytical - numerical| / \sum |analytical|$, and find the error for the pressure field, P, to be 0.73%.

Once we have confirmed that Citcom is appropriate for solving kinematic type problems, we can compare the kinematically driven case to the buoyancy drive case with flow-through boundary conditions to be discussed later (figure 5.2). Our kinematic calculation (figure 5.2a) uses the classic boundary conditions of corner flow: the dipping slab has a prescribed downdip dimensionless velocity of one, the surface above the arc corner (right side) has a fixed velocity of zero, and the surface above the oceanic corner (left side) has a horizontal dimensionless velocity of one towards the trench (i.e, the same as subducting slab velocity). The remaining three sides of our domain, for both kinematic and buoyancy cases, are flow-through conditions, where velocity parallel to the boundaries is zero and stress perpendicular to the boundaries is zero. Our buoyancy driven dynamic case (figure 5.2b) uses different conditions at the top surface and within the down-going slab: the top surface is a free-slip condition where shear stress is zero, while the slab has a set dimensionless density anomaly (of -1) instead of fixed velocity. Both cases are isoviscous mediums with 64 elements per unit length in each direction. The model domain extends from the surface to

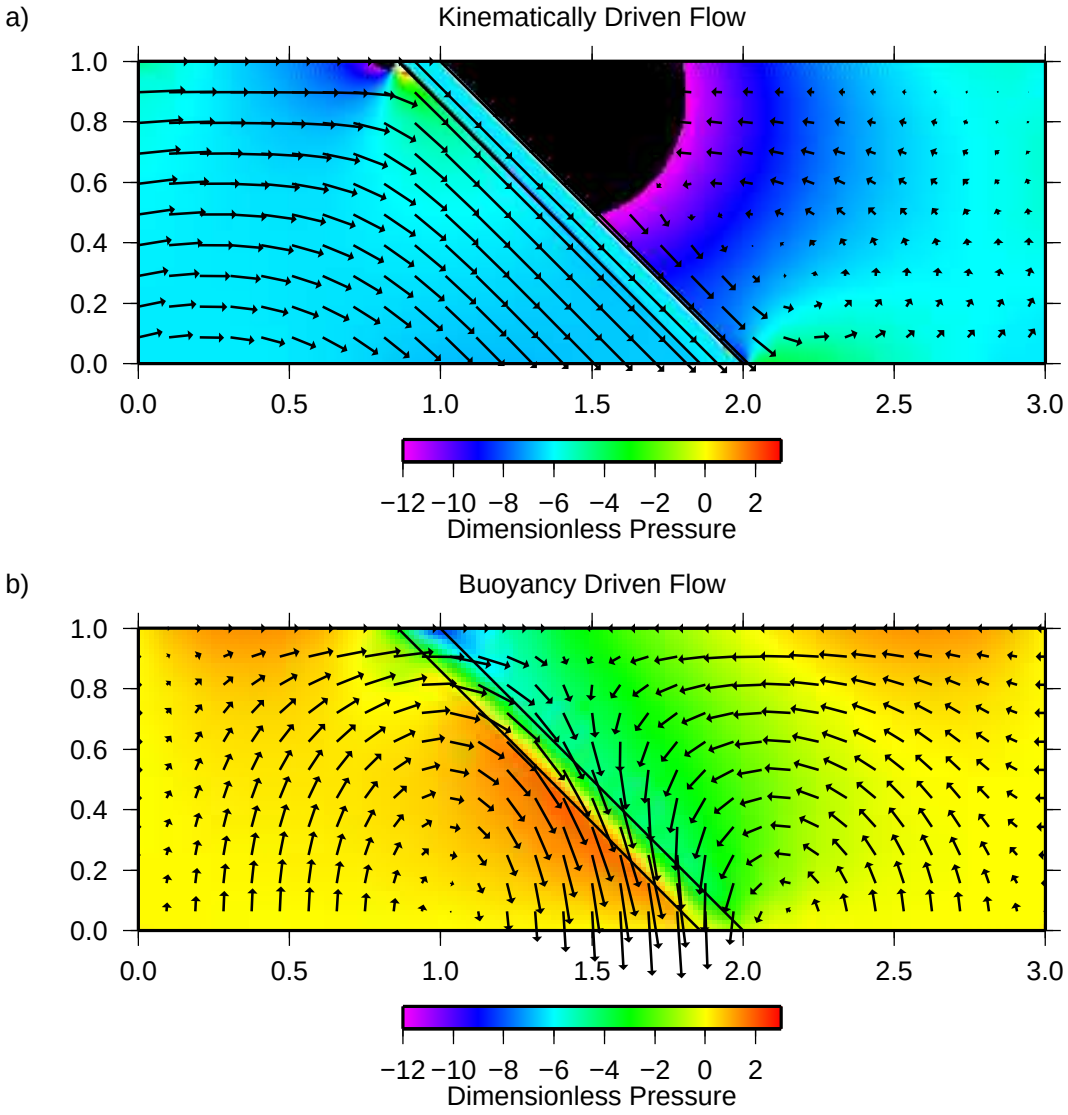

Figure 5.2: Comparison of flow (arrows) and pressure (colored background) fields for kinematically (a) and buoyancy (b) driven problems. Plate areas where velocity or buoyancy is prescribed are bounded by solid black lines. Kinematic calculation is prescribed with dimensionless velocities of one within the plate and at the surface on the oceanic side. Density difference in buoyancy calculation is adjusted so that velocity within the plate is also approximately one. This calculation also uses a free slip condition on the top surface. Both calculations have flow in/flow out side and bottom boundaries. Note different scales for pressure fields.

a depth of 1000 km and the slab is 100 km thick. We plot both cases with the same color scale, which saturates the kinematic case, but allows easy comparison of pressure gradients between the two cases.

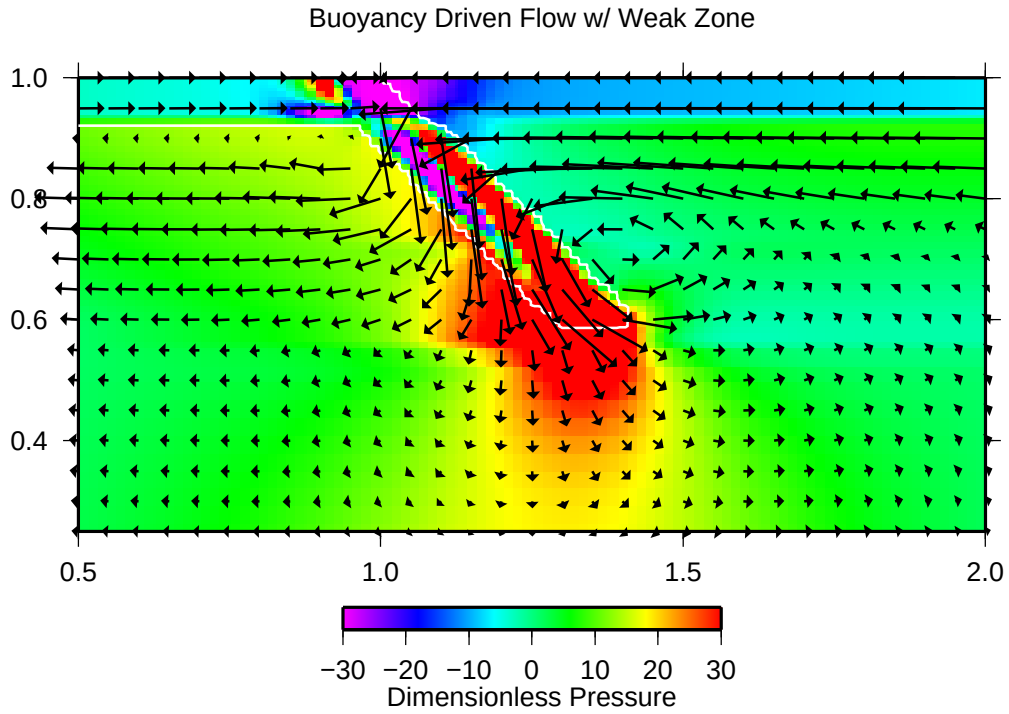

Figure 5.3: Comparison of flow (arrows) and pressure (colored background) fields for a more realistic buoyancy driven case. The background lithosphere and mantle has a layered viscosity structure, where the lithosphere (0 km $\leq$ depth $\leq$ 100 km), upper mantle (100 km $<$ depth $\leq$ 410 km), transition zone (410 km $<$ depth $\leq$ 660 km), and lower mantle (660 km $<$ depth) have viscosities of 100, 0.1, 1, and 10 respectively. Oceanic plate is outlined in white. Area shown is part of larger model space from $0 \leq x \leq 3$, $0 \leq z \leq 1$.

It is clear that the kinematic and dynamic cases (figure 5.2) have very different flow and pressure fields, and would therefore imply very different conclusions for quantities such as surface stresses and dynamic topography. The kinematic case displays similar flow and pressure fields to the analytical corner flow solution. In both arc and oceanic corners there is flow parallel to the top surface and plate boundaries. The negative pressure field in the arc corner (right side) is radially symmetric about the corner point, with the largest magnitudes concentrated in the corner (as in figure 5.1a). The oceanic corner (left side) has a pressure

field with much smaller magnitude than that in the arc corner. In contrast, the dynamic case has differences in the flow and pressure fields concentrated around the slab. Flow is no longer parallel within and around the slab, and instead varies along the slab's length. For the lower portion of the slab, the velocity implies that over time the dip should steepen in contrast to the kinematic case, where velocity normal to the slab surface is zero. The pressure field is no longer symmetric about the corner point in the arc side, and the along slab variation is reduced. Furthermore on the oceanic side, the highest pressures are no longer in the corner, but further along the slab. If we examine the pressure difference across the slab at bottom depths (say z = 0.3), the buoyancy driven case has a larger difference between the slab top and bottom (-3 to +2) than in the kinematic case (-9 to -6). This is notable since both cases have the same level of pressure on the top of the slab relative to the value at the far boundary (e.g., -9 to -6 for kinematic vs. -3 to 0 for dynamic). Only gradients in pressure are meaningful in these calculations; the overall magnitude is not.

While the cases in figure 5.2 are idealized, experiments with more realistic setup exhibit some of the same behavior. In figure 5.3 we show the flow and pressure fields for a case that may be closer to natural subduction. We use a model domain that extends from the surface to a depth of 1500 km. The background lithosphere and mantle has a layered viscosity structure, where the lithosphere (0 km $\leq$ depth $\leq$ 100 km), upper mantle (100 km $<$ depth $\leq$ 410 km), transition zone (410 km $<$ depth $\leq$ 660 km), and lower mantle (660 km $<$ depth) have viscosities of 100, 0.1, 1, and 10 respectively. The subducted plate, outlined in white, has a dip angle of 45 degrees, extends to a depth of 600 km, and has a dimensionless density difference of negative one. Viscosity for the surface plates and slab is set to 100. Within the lithosphere, between the overriding plate and the subducting plate, we use a weak zone where viscosity is set to the upper mantle value of 0.1. This effectively decouples the deformation between the plates, and results in the plates having more realistic velocities (not imposed) with motion directed towards the subduction zone. Boundary conditions are the same as in the earlier dynamic case in figure 5.2b.

As before, the flow field shows that the motion of the plate is not strictly slab parallel, as in the corner flow solution. The addition of the weak zone, allowing realistic surface motion, does not aid in shallowing the slab near the surface, although some shallowing does occur at the slab bottom near the boundary of the lower mantle ($x = 0.553$). The pressure field also shows similarity to the previous case driven by slab buoyancy. Outside of the high viscosity slab, which has the largest pressures, the other large magnitudes of pressure are concentrated below the plate as opposed to above the plate in the arc corner. These cases are meant to illustrate the point that kinematic and dynamic cases display very different flow and pressure fields and across slab pressure gradients. With such significant differences between kinematic and dynamic cases, even when allowing for more realistic surface motion, it seems necessary to reexamine what forces are controlling slab dip.

5.3.2 Torque Balance

In studies examining the steady state corner flow of subduction zones, it is a popular idea that the dip of subducted slabs is controlled by the balance of torques acting on the plate. In this section we examine this idea by determining the contributing torques along the slab and approximate the slab deformation by viscous bending. By comparing this model to numerical results we can test how applicable the model is to subduction dip. We concentrate on velocities normal to the slab surface as these determine how the dip of the slab will change. The slab normal velocities between the bending approximation and our numerical results may be expected to disagree when the viscosity of the slab is low relative to the rest of the mantle. This may be due to stretching deformation within the slab, and we examine this further below.

As mentioned earlier we sample the dynamic pressure and viscous stress loads above and below the slab from our Citcom calculations and use them in equation 5.3. Velocities from Citcom have been sampled along the middle of the slab. The velocities at the top and bottom surfaces of the slab differ slightly when the viscosity contrast is low, and this

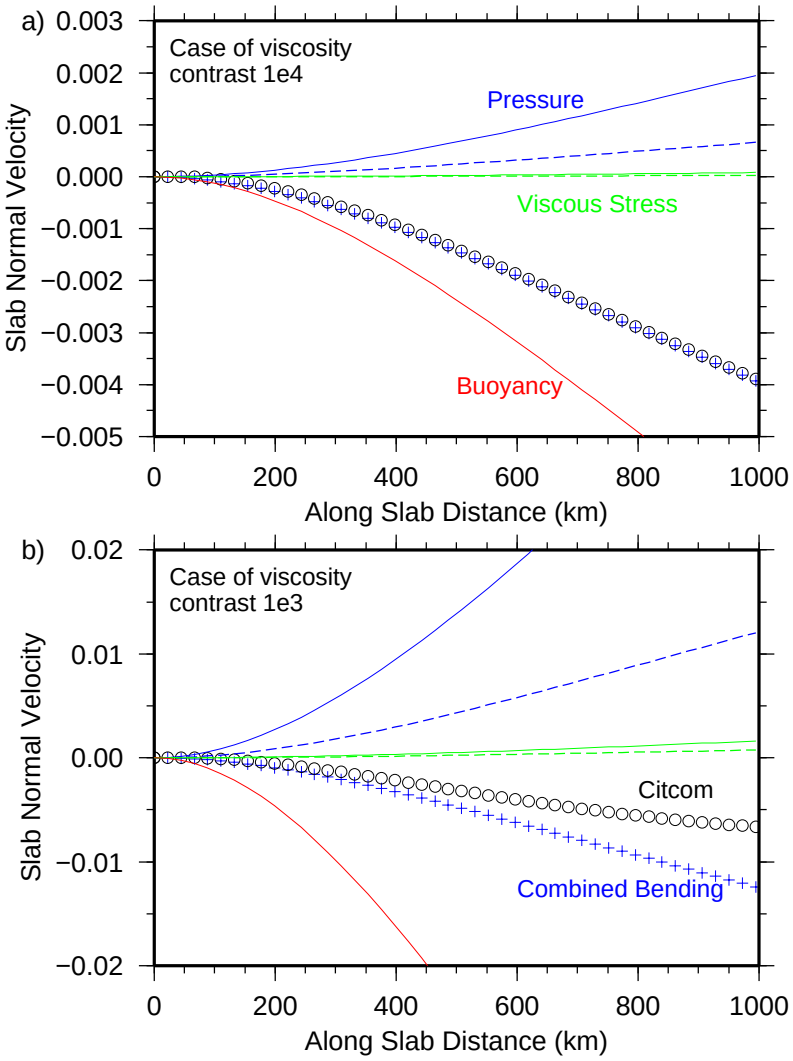

Figure 5.4: Example profiles of dimensionless slab normal velocity from several contributions. Viscous bending resulting from slab buoyancy is shown in red. Contributions from pressure above (solid line) and below (dashed line) the slab are shown in blue. Contributions from viscous stresses above (solid) and below (dashed) the slab are shown in green. The combined bending from these contributions is shown with blue crosses, while the slab normal velocity from Citcom is displayed with black circles. Slabs are 100km thick and dip at 45 degrees. a) Case of viscosity contrast 1e4. Here Citcom and combined bending velocities overlap. b) Case of viscosity contrast 1e3.

is discussed further below. The resulting slab normal velocities can be plotted (figure 5.4) to show the varying contributions from pressures and viscous forces (e.g., equation 5.3) to the total velocity from the bending model. Negative normal velocities represent motion that steepens the slab. When we consider a case of a slab dipping at 45 degrees with a large viscosity contrast between the slab and ambient mantle (1e4, and boundary conditions were discussed in the model section, figure 5.4a), the slab normal velocity predicted from the bending model agrees well with that from Citcom. The largest contributor to slab normal velocity is the negative buoyancy. The pressures above the below the slab both act to shallow the slab, or reduce its negative normal velocity, with the pressure above the slab in the arc corner having the larger effect. Contributions from the deviatoric viscous stress are near zero, which is expected when the viscosity contrast is large since the stresses are scaled by the ambient viscosity. For a case of lower viscosity contrast (1e3, figure 5.4b) the agreement between Citcom results and the bending model is not as good. In this case the disagreement is mainly concentrated at the bottom end of the slab, where the Citcom velocities have lower magnitude than those from the bending model. This is typical of many cases with significant misfit; in the majority of cases the velocities from the bending model are more negative than those from Citcom, implying that the bending model predicts more steepening.

Examining the slab normal velocity profiles for several cases allows a different understanding of the misfit between the two models (figure 5.5). Overall, the models agree with each other at larger viscosity contrasts, when the slab is more rigid. As this viscosity contrast is reduced, the misfit increases. In some cases, such as figure 5.5b, the misfit can be considered as a nearly constant percentage of the Citcom normal velocity at any point along the slab. In other cases, such as in figure 5.5c, the Citcom velocities display significant changes in moment (curvature) along the slab which are not displayed in the bending results. This is also apparent for lower viscosity contrasts (e.g., 1e2) and in these cases the misfit varies along the slab.

The good agreement between the bending model and our numerical results occurs when

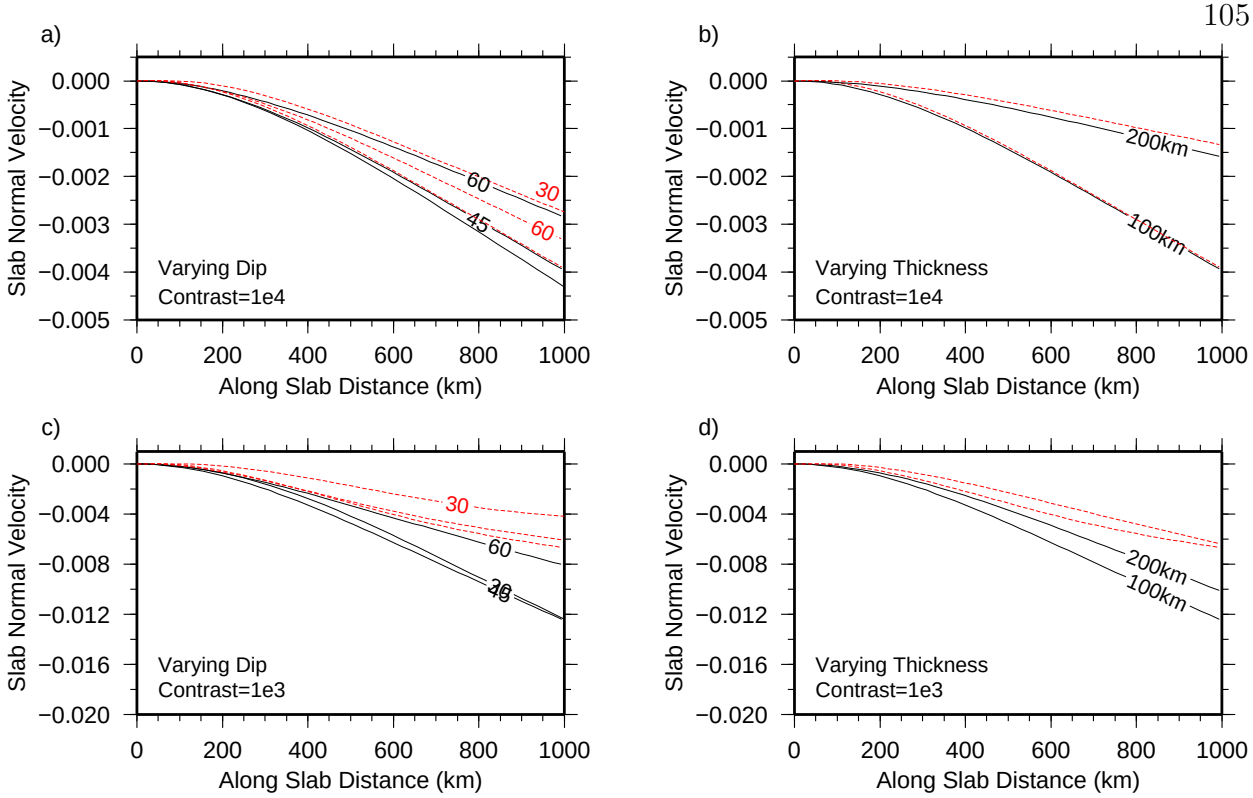

Figure 5.5: Profiles of dimensionless velocity along the slab for Citcom data (red lines) and viscous bending model (black lines). Top row uses a viscosity contrast of 1e4 and bottom row uses a viscosity contrast of 1e3. Left column of panels is for varying dip while right column shows varying thickness. a) Lines are marked with dip. Black and red lines that overlap are for 45 degree dip. b) Red line for 100km lies near black line for 100km, and vice versa. c) Two overlapping unlabeled red lines are for 45 and 60 degree dips. d) Overlapping red lines are for 100km and 200km thicknesses.

the viscosity contrast between the slab and ambient mantle is greater than $\geq 3 \times 10^3$ (figure 5.6a for average slab normal velocities). As the viscosity contrast between the slab and mantle is reduced, the disagreement between the two methods quickly increases. When the viscosity contrast is 10^3, the misfit in figure 5.6a approaches 100%. Equation 5.3 implies a monotonic and direct relationship of slab normal velocity and slab viscosity. Therefore when other factors are held constant, increasing viscosity of the slab by ten times will reduce the slab normal bending velocity by ten times. However, the velocities from Citcom models are not as sensitive to slab viscosity when the slab viscosity contrast is smaller than 3000 (figure 5.6a), leading to a large misfit between these two models (figure 5.6a). In figure 5.6b,d it is

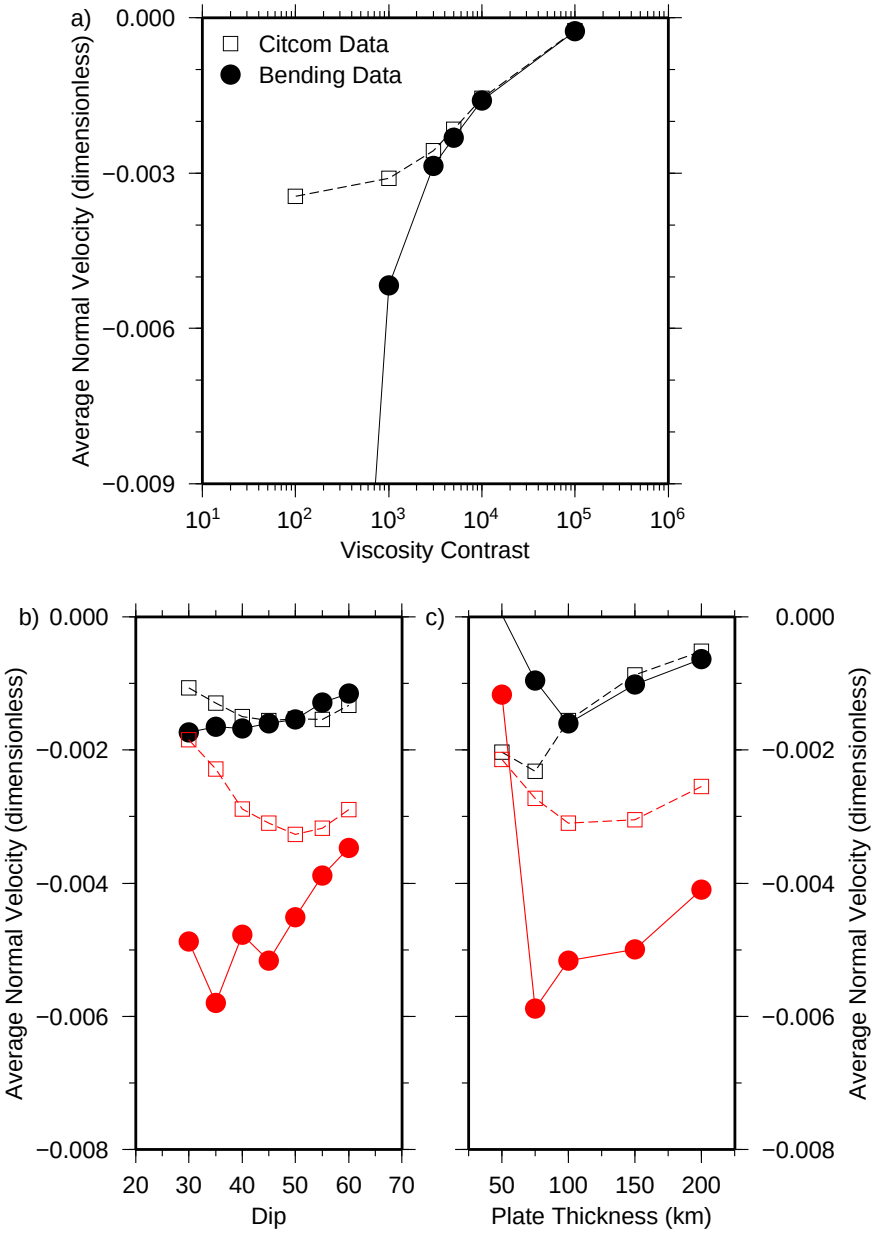

Figure 5.6: Comparisons between Citcom numerical data (circles with solid line) and data from the viscous bending approximation (squares with dashed line). a) Results for a slab 100km in thickness, dipping at 45 degrees, for various viscosity contrasts between the slab and ambient mantle. b) Results for a slab 100km thick for various dips. Black data has a viscosity contrast of 10^4 between slab and ambient mantle, while red data has contrast of 10^3. c) Results for slabs of various thicknesses, dipping at 45 degrees. Black and red data as in b).

apparent that even at very large slab thicknesses (200 km) the bending approximation does not perform significantly worse than for slabs of moderate thickness (100 km). Instead, the misfit related to viscosity contrast is more important than the misfit related to slab thickness (i.e., how well the slab approximates a thin sheet).

In figures 5.6b and c, we additionally compare the velocities for varying dip and plate thickness, respectively. Using kinematic results as a cue, the pressure field in the arc corner can be expected to vary significantly with slab dip. As dip varies, the portion of buoyancy normal to the slab surface also varies, however, and the net result for contrast 1e4 is that velocities do not vary significantly (figure 5.6b). For a lower viscosity contrast (1e3) the velocities vary more with dip and have worse agreement which appears dip dependent. While the slab viscosity is linearly related to the normal velocity for a fixed load, the slab thickness is related with a power of two in Equation 5.3, and therefore might be expected to be an important controlling parameter. Indeed, absolute velocities for 1e4 contrast vary more with thickness than with dip. Interestingly, slabs 100 km or thicker show better agreement between bending and Citcom models than slabs thinner than 100 km, for $1e4$ and $1e3$ viscosity contrasts even though the thin sheet approximation should be more valid for thinner slabs.

We also plot the absolute value of average slab normal velocities from Citcom models (from the slab mid-plane) against those from the bending model in figure 5.7, so that cases with the best matches lie near the diagonal line with a slope of one. When viewing all of the data together (figure 5.7a) clear differences can be seen between cases with high viscosity contrast ($\geq$ 1e4) and those with lower but perhaps more realistic contrast ($\leq$ 1e3). Cases with high viscosity contrast and more rigid slabs can be better approximated by viscous bending than the lower contrast cases. When the viscosity contrast is low, the viscous bending model significantly over predicts slab normal velocities by an order of magnitude compared with those from Citcom. It should also be clear that slabs thinner than 100 km exhibit much worse agreement for the bending approximation as many of the 75 km thick cases (squares, figure 5.7) lie the furthest away from the diagonal line. In figures 5.7b,c,

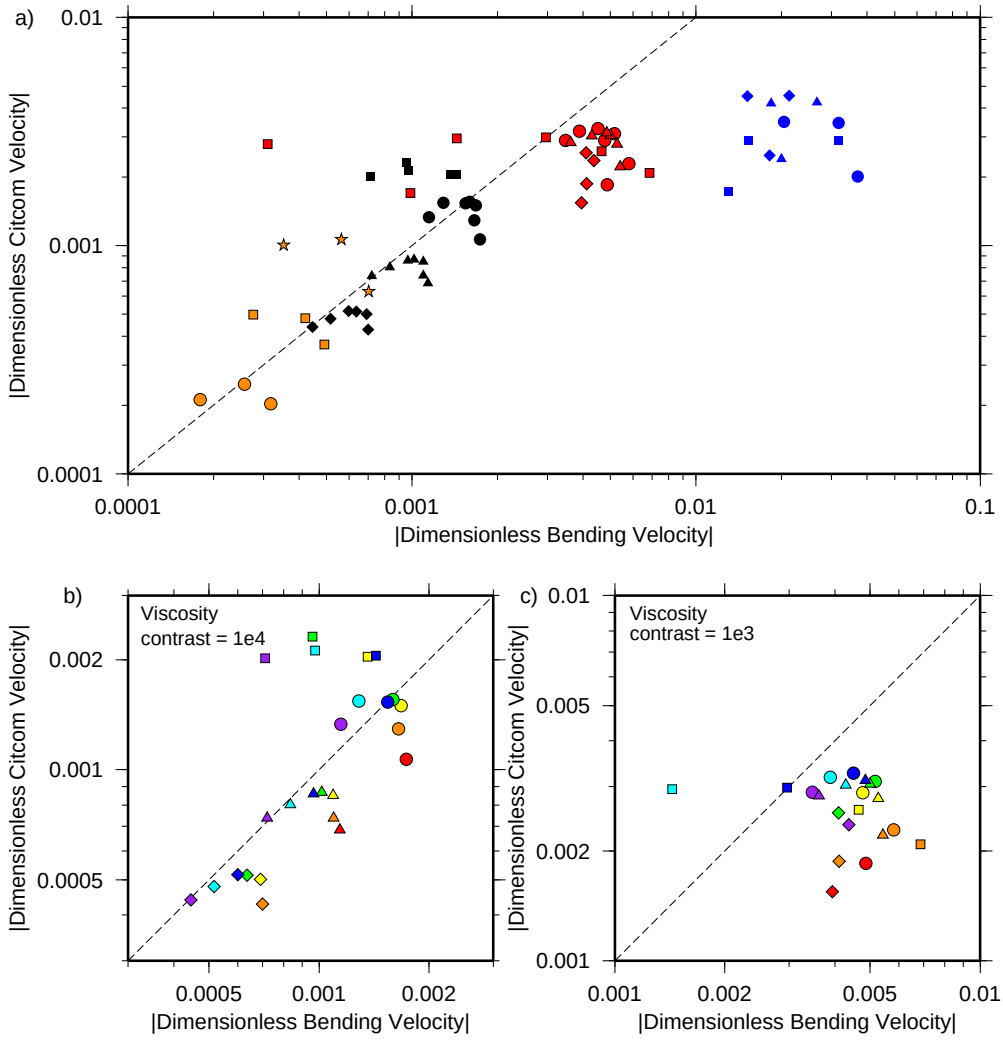

Figure 5.7: Plots of the absolute value of average dimensionless Citcom velocity vs. bending velocity for various thicknesses and dips. In all figures varying thickness is indicated by shape. Cases of 200km thick slabs are diamonds, 150km thick slabs are triangles, 100km thick slabs are circles, 75km thick slabs are squares, and 50km thick slabs are stars. a) Cases with viscosity contrast of 1e2 are blue, cases with contrast of 1e3 are red, cases with contrast of 1e4 are black, and cases with viscosity contrast of 1e5 are orange points. b) Cases with viscosity contrast = 1e4. Colors represent slab dip angle. Cases with 30 degree dip are red, 35 degree dips are orange, 40 degree dips are yellow, 45 degree dips are green, 50 degree dips are blue, 55 degree dips are cyan, and 60 degree dips are purple. Shapes represent thickness as in a). c) Cases with viscosity contrast = 1e3. Colors and shapes are as in b). One to one line shown dashed in all figures.

which each focus on a single viscosity contrast, we highlight the variation of velocity with slab dip and thickness. Overall, steeper dips (e.g., purple or cyan) display better agreement. While cases with thickness greater than 100 km have about the same agreement, cases with plates thinner than 100 km show poor agreement (e.g., squares = 75 km), as they plot further from the diagonal line. For the cases of lower viscosity contrast (1e3, figure 5.7c), steeper dips again show better agreement. However, the overall accuracy is not as good as cases for 1e4 contrast, and the bending model over predicts the slab normal velocities (more steepening) compared with the Citcom model.

In the solution from *Ribe* (2001) the bending and stretching of thin viscous sheets was derived with asymptotic expansions that exploit how the sheet is thin relative to its length. This allows deformation of the sheet to be expressed along its mid surface. Under these conditions the characteristic timescales of bending and stretching are related to one another simply depending on the ratio of thickness to length. These assumptions work well when the sheet is very viscous relative to the ambient medium. When the viscosity of the sheet is not as high relative to the ambient medium, however, internal deformation within the sheet may be significant. In figure 5.8 we plot the ratio between average slab parallel velocity and average slab normal velocity from the slab mid-plane, expressed as a percentage. When the slab is very rigid and has a high viscosity contrast with the mantle (e.g., 1e4) the magnitude of slab parallel velocity is very small compared with slab normal velocity. This agrees well with the model problems of *Ribe* (2001), where stretching deformation occurred on a much slower timescale than bending. As the viscosity contrast is reduced, slab parallel velocity becomes more significant, and for cases with viscosity contrast 1e2 it can exceed 50% of the slab normal velocity when the dip is steep. Of course for a vertical slab the normal component of velocity might vanish and this ratio will be very large, but comparing the steeply dipping slabs (60 degrees) for 1e2 contrast with higher viscosity contrasts show this is not a large concern for these dips. When slab parallel and slab normal velocities are examined in more detail (figure 5.8b, a case with 1e2 viscosity contrast and dip=60 degrees)

differences can be seen between the slab normal velocity at the top and bottom surfaces of the slab. These differences are concentrated near the fixed end of the slab. This internal deformation within the slab is a likely cause of the disagreement between the bending model and our numerical results.

Overall, our results here suggest that the bending model works well in predicting slab normal velocity and hence slab dip for more rigid slabs (> more than 3 orders of magnitude more viscous than the ambient mantle and > 100 km thick), but the bending model fails to predict slab normal velocities or slab dips for slabs with more realistic viscosity contrasts (< 3 orders of magnitude).

5.4 Discussion and Conclusions

When kinematic corner flow models are used to examine the dip angle of subducting slabs, there is no deformation within the slab, and the slabs simply rotate in response to torques applied on their surfaces. We examine a viscous bending model that balances torques on the slab by allowing shear on planes perpendicular to the slab surface. Both models give insight, but both also appear inadequate because slabs display significant internal deformation when their viscosity is closer to commonly assumed values.

When subducted slabs have a viscosity within a few orders of magnitude of the ambient mantle, balancing the viscous bending torques on the slab is not a good approximation for the slab's normal velocity due to extension of the slab parallel to the the slab surface. For this approximation to be valid, and for the theory of *Ribe* (2001) to be accurate, the slab needs to have a viscosity contrast at least 3e3 times larger than the mantle. An estimate of average upper mantle viscosity of 10^{20} Pa s suggests that the average slab viscosity would need to be greater than 3×10^{23} Pa s for this good agreement (e.g. *Harig et al.*, 2010b), which is higher than the estimated slab strength from other dynamic studies (e.g. *Moresi and Gurnis*, 1996). This indicates that balancing the torques on subducted slabs is not a good way to infer slab dip angle, and could lead to incorrect conclusions on the processes

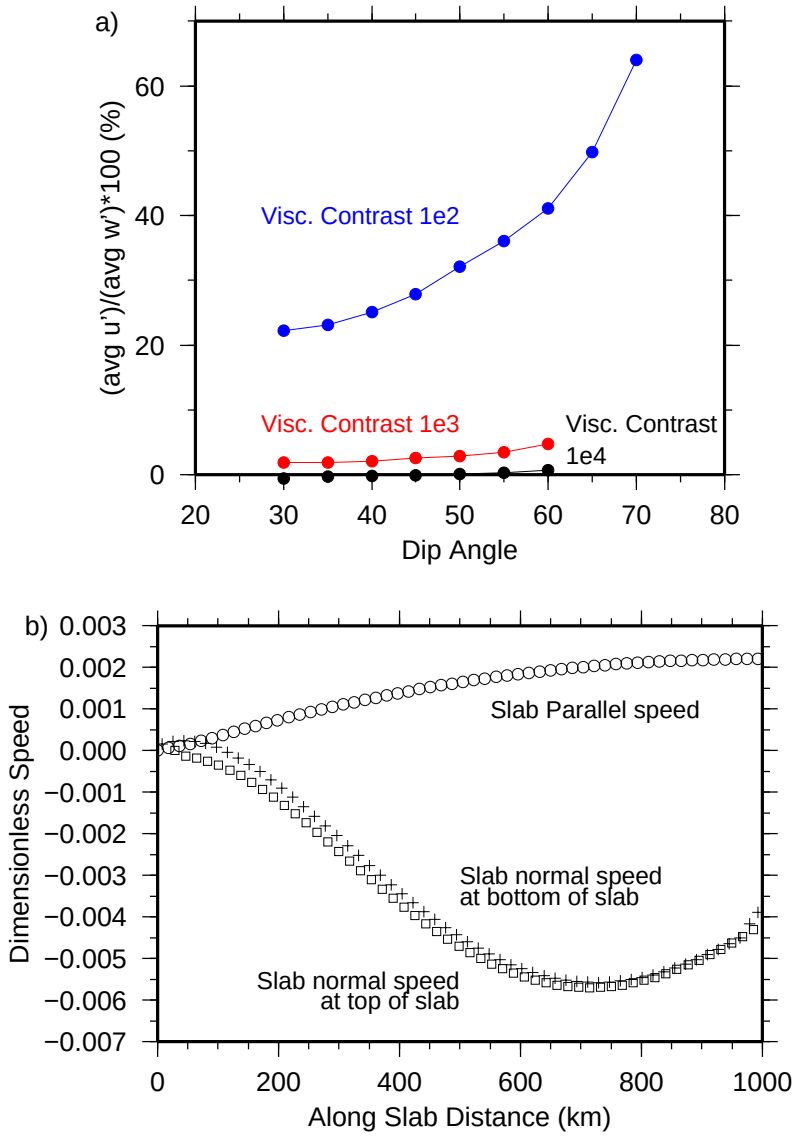

Figure 5.8: a) Plot of average slab parallel speed along the slab divided by average slab normal speed along the slab, expressed as a percentage, vs. dip angle. Three different viscosity contrasts are shown: 1e4 in black, 1e3 in red, and 1e2 in blue (as in figure 5.7a). b) An example of how slab normal and slab parallel speed vary along slab for a case with dip = 60 degrees and viscosity contrast equal to 1e2. Positive slab parallel speed (i.e., downdip extension) is shown with circles and is from the middle of the slab. Slab normal speed is shown at both the top (squares) and bottom (crosses) boundaries of the slab.

behind shallow angle subduction.

Our main conclusions can be summarized as follows:

1) Considering subduction with kinematic experiments and some models with plausible dynamics leads to very different conclusions about the preferred dip of subducting slabs. Bringing these models into agreement is not a straightforward task and it is not entirely clear this is possible.

2) When subducted slabs have a high viscosity relative to the ambient mantle ($\geq$ 1e4) their deformation can be approximated by the viscous bending of a thin beam. An exception to this good agreement is that thin slabs of < 75 km show quite poor agreement to the approximation even though the thin sheet approximation should be more valid for these thin plates. Generally, the agreement is better for steeper dips than for shallow dips.

3) When subducted slabs have a lower, but perhaps still large viscosity relative to the ambient mantle ($\leq$ 1e3) balancing the viscous bending torques on the slab is not a good approximation for the slab's deformation due to internal deformation within the slab. This suggests that perhaps this method is not a good way to make inferences about slab dip angle.

5.5 Acknowledgments

This research was supported by the National Science Foundation and the Graduate School at the University of Colorado. Figures created with the GMT software (*Wessel and Smith*, 1998).

Bibliography

Allmendinger, R. W., T. E. Jordan, S. M. Kay, and B. L. Isacks (1997), The evolution of the Altiplano-Puna Plateau of the Central Andes, *Annu. Rev. Earth Planet Sci.*, *25*, 139–174.

Artemieva, I. M. (2009), The continental lithosphere: Reconciling thermal, seismic, and petrologic data, *Lithos*, *109*, 23–46, doi:10.1016/j.lithos.2008.09.015.

Atwater, T., and J. Stock (1998), Pacific-North America plate tectonics of the Neogene southwestern United States: An update, *Int. Geol. Rev.*, *40*, 375–402.

Austrheim, H. (1991), Eclogite formation and dynamics of crustal roots under continental collision zones, *Terra Nova*, *3*, 492–499.

Ballard, S., and H. N. Pollack (1987), Diversion of heat by Archean cratons: a model for southern Africa, *Earth Planet. Sci. Lett.*, *85*, 253–264.

Barazangi, M., and B. L. Isacks (1976), Spatial distribution of earthquakes and subduction of the Nazca plate beneath South America, *Geology*, *4*, 686–692.

Bassi, G., and J. Bonnin (1988), Rheological modelling and deformation instability of lithosphere under extension, *Geophys. J. Int.*, *93*, 485–504.

Batchelor, G. K. (2000), *An introduction to fluid dynamics*, Cambridge University Press.

Becker, T. W. (2006), On the effect of temperature and strain-rate dependent viscosity on global mantle flow, net rotation, and plate-driving forces, *Geophys. J. Int.*, *167*, 943–957, doi:10.1111/j.1365-246X.2006.03172.x.

Becker, T. W. (2008), Azimuthal seismic anisotropy constrains net rotation of the lithosphere, *Geophys. Res. Lett.*, *35*, L05303, doi:10.1029/2007GL032928.

Becker, T. W., C. Faccenna, R. J. O'Connell, and D. Giardini (1999), The development of slabs in the upper mantle: Insights from numerical and laboratory experiments, *J. Geophys. Res.*, *104* (B7), 15,207–15,226.

Becker, T. W., J. B. Kellogg, G. Ekström, and R. J. O'Connell (2003), Comparison of azimuthal seismic anisotropy from surface waves and finite strain from global mantle-circulation models, *Geophys. J. Int.*, *155*, 696–714.

Becker, T. W., S. Chevrot, V. Schulte-Pelkum, and D. K. Blackman (2006), Statistical properties of seismic anisotropy predicted by upper mantle geodynamic models, *J. Geophys. Res.*, *111*, B08309, doi:10.1029/2005JB004095.

Behn, M. D., C. P. Conrad, and P. G. Silver (2004), Detection of upper mantle flow associated with the African Superplume, *Earth Planet. Sci. Lett.*, *224*, 259–274.

Benz, H. M., and G. Zandt (1993), Teleseismic tomography: lithospheric structure of the San Andreas fault system in northern and central California, in *Seismic Tomography: Theory and practice*, edited by H. M. Iyer and K. Hirahara, pp. 440–465, Chapman and Hall.

Billen, M. I. (2008), Modeling the dynamics of subducting slabs, *Annu. Rev. Earth Planet Sci.*, *36*, 325–356, doi:10.1146/annurev.earth.36.031207.124129.

Billen, M. I., and G. Hirth (2007), Rheologic controls on slab dynamics, *Geochem., Geophys., Geosyst.*, *8*(8), Q08012, doi:10.1029/2007GC001597.

Bird, P. (1978), Initiation of Intracontinental Subduction in the Himalaya, *J. Geophys. Res.*, *83*(B10), 4975–4987.

Brace, W. F., and D. L. Kohlstedt (1980), Limits on lithospheric stress imposed by laboratory experiments, *J. Geophys. Res.*, *85*, 6248–6252.

Canright, D., and S. Morris (1993), Buoyant instability of a viscous film over a passive fluid, *J. Fluid Mech.*, *255*, 349–372.

Cathles, L. M. (1975), *The viscosity of the Earth's mantle*, Princeton University Press, Princeton.

Chandrasekhar, S. (1961), *Hydrodynamic and Hydromagnetic Stability*, Oxford University Press, Oxford.

Christensen, U. R. (1996), The influence of trench migration on slab penetration into the lower mantle, *Earth Planet. Sci. Lett.*, *140*, 27–39.

Conrad, C. P., and M. D. Behn (2010), Constraints on lithosphere net rotation and asthenospheric viscosity from global mantle flow models and seismic anisotropy, *Geochem., Geophys., Geosyst.*, *11*(5), Q05W05, doi:10.1029/2009GC002970.

Conrad, C. P., and B. H. Hager (1999), Effects of plate bending and fault strength at subduction zones on plate dynamics, *J. Geophys. Res.*, *104*, 17,551–17,571.

Conrad, C. P., and C. Lithgow-Bertelloni (2006), Influence of continental roots and asthenosphere on plate-mantle coupling, *Geophys. Res. Lett.*, *33*, L05312.

Conrad, C. P., and P. Molnar (1997), The growth of Rayleigh-Taylor-type instabilities in the lithosphere for various rheological and density structures, *Geophys. J. Int.*, *129*, 95–112.

Conrad, C. P., and P. Molnar (1999), Convective instability of a boundary layer with temperature and strain-rate-dependent viscosity in terms of 'available buoyancy', *Geophys. J. Int.*, *139*, 51–68.

Conrad, C. P., M. D. Behn, and P. G. Silver (2007), Global mantle flow and the development of seismic anisotropy: Differences between the oceanic and continental upper mantle, *J. Geophys. Res.*, *112*, B07317, doi:10.1029/2006JB004608.

Conrad, C. P., B. Wu, E. I. Smith, T. A. Bianco, and A. Tibbetts (2010), Shear-driven upwelling induced by lateral viscosity variations and asthenospheric shear: A mechanism for intraplate volcanism, *Phys. Earth Planet. Inter.*, *178*, 162–175, doi:10.1016/j.pepi.2009.10.001.

Davies, J. H., and D. J. Stevenson (1992), Physical model of source region of subduction zone volcanics, *J. Geophys. Res.*, *97*(B2), 2037–1070.

Dayem, K. E., G. A. Houseman, and P. Molnar (2009), Localization of shear along a lithospheric strength discontinuity: Application of a continuous deformation model to the boundary between Tibet and the Tarim Basin, *Tectonics*, *28*, TC3002, doi:10.1029/2008TC002264.

Debayle, E. (1999), SV-wave azimuthal anisotropy in the Australian upper mantle: Preliminary results from automated Rayleigh waveform inversion, *Geophys. J. Int.*, *137*, 747–754.

Debayle, E., and B. L. N. Kennett (2000a), The Australian continental upper mantle: Structure and deformation inferred from surface waves, *J. Geophys. Res.*, *105*, 25,423–25,450.

Debayle, E., and B. L. N. Kennett (2000b), Anisotropy in the Australian upper mantle from Love and Rayleigh waveform inversion, *Earth Planet. Sci. Lett.*, *184*, 339–351.

Debayle, E., B. Kennett, and K. Priestley (2005), Global azimuthal seismic anisotropy and the unique plate-motion deformation of Australia, *Nature*, *433*, 509–512.

Dewey, J. F., and J. M. Bird (1970), Mountain belts and the new global tectonics, *J. Geophys. Res.*, *75*, 2625–2647.

Dewey, J. F., and K. C. A. Burke (1973), Tibetan, Variscan, and Precambrian basement reactivation: products of continental collision, *J. Geol.*, *81*, 683–692.

Dricker, I. G., and S. W. Roecker (2002), Lateral heterogeneity in the upper mantle beneath the Tibetan plateau and its surroundings from SS-S travel time residuals, *J. Geophys. Res.*, *107*, 1–11.

Ducea, M. N., and J. B. Saleeby (1996), Buoyancy sources for a large, unrooted mountain range, the Sierra Nevada, California: Evidence from xenolith thermobarometry, *J. Geophys. Res.*, *101*(B4), 8229–8244.

Ducea, M. N., and J. B. Saleeby (1998), A case for delamination of the deep batholithic crust beneath the Sierra Nevada, California, *Int. Geol. Rev.*, *133*, 78–93.

Ekström, G., and A. M. Dziewonski (1998), The unique anisotropy of the Pacific upper mantle, *Nature*, *394*, 168–172.

Elkins-Tanton, L. T. (2005), Continental magmatism caused by lithospheric delamination, *Spec. Pap. Geol. Soc. Am.*, *388*, 449–461.

Elkins-Tanton, L. T. (2007), Continental magmatism, volatile recycling, and a heterogeneous mantle caused by lithospheric gravitational instabilities, *J. Geophys. Res.*, *112*, 1–13.

Elkins-Tanton, L. T., and T. L. Grove (2003), Evidence for deep melting of hydrous metasomatized mantle: Pliocene high-potassium magmas from the sierra nevadas, *J. Geophys. Res.*, *108*, 2350.

Elkins-Tanton, L. T., and B. H. Hager (2000), Melt intrusion as a trigger for lithospheric foundering and the eruption of the Siberian flood basalt, *Geophys. Res. Lett.*, *27*, 3937–3940.

England, P., and G. Houseman (1989), Extension during continental convergence, with application to the Tibetan Plateau, *J. Geophys. Res.*, *94*(B12), 17,561–17,579.

England, P., G. Houseman, and L. Sonder (1985), Length scales for continental deformation in convergent, divergent, and strike-slip environments: Analytical and approximate solutions for a thin viscous sheet model, *J. Geophys. Res.*, *90*, 3551–3557.

England, P., R. Engdahl, and W. Thatcher (2004), Systematic variation in the depths of slabs beneath arc volcanoes, *Geophys. J. Int.*, *156*, 377–408.

Evans, B., and C. Goetze (1979), Temperature variation of hardness of olivine and its implication for polycrystalline yield stress, *J. Geophys. Res.*, *84*, 5505–5524.

Farmer, G. L., A. F. Glazner, and C. R. Manley (2002), Did lithospheric delamination trigger late Cenozoic potassic volcanism in the southern Sierra Nevada, California?, *Geol. Soc. Am. Bull.*, *114*, 754–768.

Farmer, G. L., T. Bailley, and L. T. Elkins-Tanton (2008), Mantle source volumes and the origin of the mid-Tertiary ignimbrite flare-up in the southern Rocky Mountains, western U.S., *Lithos*, *102*, 279–294.

Fletcher, R. C., and B. Hallet (1983), Unstable extension of the lithosphere: a mechanical model for Basin-and-Range structure, *J. Geophys. Res.*, *88*(B9), 7457–7466.

Forsyth, D. W. (1975), The early structural evolution and anisotropy of the oceanic upper mantle, *Geophys. J. R. astr. Soc.*, *43*, 103–162.

Forte, A. M., and W. R. Peltier (1994), The kinematics and dynamics of poloidal – toroidal coupling of mantle flow: the importance of surface plates and lateral viscosity variations, *Adv. Geophys.*, *36*, 1–119.

Fouch, M. J., and S. Rondenay (2006), Seismic anisotropy beneath stable continental interiors, *Phys. Earth Planet. Inter.*, *158*, 292–320.

Fouch, M. J., K. M. Fischer, E. M. Parmentier, M. E. Wysession, and T. J. Clarke (2000), Shear wave splitting, continental keels, and patterns of mantle flow, *J. Geophys. Res.*, *105*(B3), 6255–6275.

Fountain, D. M., and N. I. Christensen (1989), Composition of the continental crust and upper mantle: A review, in *Geophysical framework of the continental United States*, *Geological Society of America Memoir*, vol. 179, edited by L. C. Pakiser and W. D. Mooney, Geological Society of America.

Freeden, W., and V. Michel (1999), Constructive approximation and numerical methods in geodetic research today – An attempt at a categorization based on an uncertainty principle, *Journal of Geodesy*, *73*, 452–465.

Gao, S., R. L. Rudnick, W.-L. Xu, H.-L. Yuan, Y.-S. Liu, R. J. Walker, I. S. Puchtel, X. Liu, H. Huang, X.-R. Wang, and J. Yang (2008), Recycling deep cratonic lithosphere and generation of intraplate magmatism in the North China Craton, *Earth Planet. Sci. Lett.*, *270*, 41–53.

Gemmer, L., and G. A. Houseman (2007), Convergence and extension driven by lithospheric gravitational instability: evolution of the Alpine-Carpathian-Pannonion system, *Geophys. J. Int.*, *168*, 1276–1290.

Gilbert, H. J., A. F. Sheehan, D. A. Wiens, K. G. Dueker, L. M. Dorman, J. Hildebrand, and S. Webb (2001), Upper mantle discontinuity structure in the region of the Tonga Subduction Zone, *Geophys. Res. Lett.*, *28*(9), 1855–1858.

Goetze, C. (1978), Mechanisms of creep in olivine, *Philos. Trans. R. Soc. London*, *288*, 99–119.

Gripp, A. E., and R. G. Gordon (2002), Young tracks of hotspots and current plate velocities, *Geophys. J. Int.*, *150*, 321–361.

Gung, Y., M. Panning, and B. Romanowicz (2003), Global anisotropy and the thickness of continents, *Nature*, *422*, 707–711.

Hager, B. H. (1984), Subducted slabs and the geoid: constraints on mantle rheology and flow, *J. Geophys. Res.*, *89*(B7), 6003–6015.

Hager, B. H., and M. A. Richards (1989), Long-wavelength variations in Earth's geoid: physical models and dynamical implications, *Philos. Trans. R. Soc. London*, *328*, 309–327.

Han, D., and J. Wahr (1995), The viscoelastic relaxation of a realistically stratified earth, and a further analysis of postglacial rebound, *Geophys. J. Int.*, *120*(2), 287–311, doi: 10.1111/j.1365-246X.1995.tb01819.x.

Han, L., and M. Gurnis (1999), How valid are dynamic models of subduction and convection when plate motions are prescribed?, *Phys. Earth Planet. Inter.*, *110*, 235–246.

Harig, C., P. Molnar, and G. A. Houseman (2008), Rayleigh-Taylor instability under a shear stress free top boundary condition and its relevance to removal of mantle lithosphere from beneath the sierra nevada, *Tectonics*, *27*, TC6019.

Harig, C., P. Molnar, and G. A. Houseman (2010a), Lithospheric thinning and localization of deformation during rayleigh-taylor instability with nonlinear rheology and implications for intracontinental magmatism, *J. Geophys. Res.*, *115*, B02205, doi:10.1029/2009JB006422.

Harig, C., S. Zhong, and F. Simons (2010b), Constraints on upper mantle viscosity from the flow-induced pressure gradient across the Australian continental keel., *Geochem., Geophys., Geosyst.*, *11*(6), Q06004, doi:10.1029/2010GC003038.

Hartog, R., and S. Y. Schwartz (2000), Subduction-induced strain in the upper mantle east of the Mendocino triple junction, California, *J. Geophys. Res.*, *105*, 7909–7930.

Haxby, W. F., and D. L. Turcotte (1978), On isostatic geoid anomalies, *J. Geophys. Res.*, *83*(B11), 5473–5478.

Hess, H. H. (1964), Seismic anisotropy of the uppermost mantle under oceans, *Nature*, *203*, 629–631.

Hirth, G., R. L. Evans, and A. D. Chave (2000), Comparison of continental and oceanic mantle electrical conductivity: Is the Archean lithosphere dry?, *Geochem., Geophys., Geosyst.*, *1*(12), 1–9, doi:10.1029/2000GC000048.

Hoernle, K., J. D. L. White, P. van der Bogaard, F. Hauff, D. S. Coombs, R. Werner, C. Timm, D. Garbe-Schonberg, A. Reay, and A. F. Cooper (2006), Cenozoic intraplate volcanism on new zealand: Upwelling induced by lithospheric removal, *Earth Planet. Sci. Lett.*, *248*, 335–352.

Hoogenboom, T., and G. A. Houseman (2006), Rayleigh-Taylor instability as a mechanism for corona formation on Venus, *Icarus*, *180*, 292–307.

Houseman, G. A., and D. Gubbins (1997), Deformation of subducted oceanic lithosphere, *Geophys. J. Int.*, *131*, 535–551.

Houseman, G. A., and P. Molnar (1997), Gravitational (Rayleigh-Taylor) instability of a layer with non-linear viscosity and convective thinning of continental lithosphere, *Geophys. J. Int.*, *128*, 125–150.

Houseman, G. A., D. P. McKenzie, and P. Molnar (1981), Convective instability of a thickened boundary layer and its relevance for the thermal evolution of continental convergent belts, *J. Geophys. Res.*, *86*(B7), 6115–6132.

Hughes, T. J. R. (2000), *The finite element method: Linear static and dynamic finite element analysis*, Dover Publications.

Jadamec, M. A., and M. I. Billen (2010), Reconciliing surface plate motions with rapid three-dimensional mantle flow around a slab edge, *Nature*, *465*, 338–342, doi:10.1038/nature09053.

Jarrard, R. D. (1986), Relations among subduction parameters, *Reviews of Geophysics*, *24*(2), 217–284.

Jaupart, C., J. C. Mareschal, L. Guillou-Frottier, and A. Davaille (1998), Heat flow and thickness of the lithosphere in the Canadian Shield, *J. Geophys. Res.*, *103*(B7), 15,269–15,286.

Jones, C. H., and R. A. Phinney (1999), Prospecting for the petrology of the upper mantle: Teleseismic shear waves in the Sierra Nevada, California, *Geological Society of America Abstracts with Programs*, *31*(7), A–481.

Jones, C. H., H. Kanamori, and S. W. Roecker (1994), Missing roots and mantle 'drips': Regional P_n and teleseismic arrival times in the southern Sierra Nevada and vicinity, California, *J. Geophys. Res.*, *99*(B3), 4567–4601.

Jones, C. H., G. L. Farmer, and J. Unruh (2004), Tectonics of Pliocene removal of the lithosphere of the Sierra Nevada, California, *Geol. Soc. Am. Bull.*, *116*(11/12), 1408–1422.

Jordan, T. E., B. L. Isacks, R. W. Allmendinger, J. A. Brewer, V. A. Ramos, and C. J. Ando (1983), Andean tectonics related to geometry of subduction of Nazca plate, *Geol. Soc. Am. Bull.*, *94*, 341–361.

Jull, M., and P. B. Keleman (2001), On the conditions for lower crustal convective instability, *J. Geophys. Res.*, *106*(B4), 6423–6446.

Jung, H., and S.-i. Karato (2001), Water-induced fabric transitions in olivine, *Science*, *293*, 1460–1463.

Kaminski, E., and N. M. Ribe (2001), A kinematic model for the recrystallization and texture development in olivine polycrystals, *Earth Planet. Sci. Lett.*, *189*, 253–267.

Karato, S.-i., and P. Wu (1993), Rheology of the upper mantle: A synthesis, *Science*, *260*, 771–778.

Kay, R. W. (1980), Volcanic arc magmas: Implications of a melting-mixing model for element recycling in the crust-upper mantle system, *J. Geol.*, *88*, 497–522.

Kay, R. W., and S. M. Kay (1993), Delamination and delamination magmatism, *Tectonophysics*, *219*, 177–189.

Kennett, B. L. N., E. R. Engdahl, and R. Buland (1995), Constraints on seismic velocities in the Earth from travel times, *Geophys. J. Int.*, *122*, 108–124.

Kerr, R. C., and J. R. Lister (1988), Island arc and mid-ocean ridge volcanism, modelled by diapirism from linear source regions, *Earth Planet. Sci. Lett.*, *88*, 143–152.

Keskin, M. (2003), Magma generation by slab steepening and breakoff beneath a subduction-accretion complex: An alternative model for collision-related volcanism in Eastern Anatolia, Turkey, *Geophys. Res. Lett.*, *30*(24), 1–4.

Keskin, M., J. A. Pearce, and J. G. Mitchell (1998), Volcano-stratigraphy and geochemistry of collision-related volcanism on the Erzurum-Kars Plateau, North Eastern Turkey, *Journal of Volcanology and Geothermal Research*, *85*, 355–404.

King, S. D. (2005), Archean cratons and mantle dynamics, *Earth Planet. Sci. Lett.*, *234*, 1–14, doi:10.1016/j.epsl.2005.03.007.

King, S. D., and G. Masters (1992), An inversion for radial viscosity structure using seismic tomography, *Geophys. Res. Lett.*, *19*(15), 1551–1554.

King, S. D., and J. Ritsema (2000), African hotspot volcanism: Small-scale convection in the upper mantle beneath cratons, *Science*, *290*, 1137–1140.

Knapp, J. H., C. C. Knapp, V. Raileanu, L. Matenco, V. Mocanu, and C. Dinu (2005), Crustal constraints on the origin of mantle seismicity in the Vrancea Zone, Romania: The case for active continental lithospheric delamination, *Tectonophysics*, *410*, 311–323.

Kneller, E. A., P. E. van Keken, S.-i. Karato, and J. Park (2005), B-type olivine fabric in the mantle wedge: Insights from high-resolution non-Newtonian subduction zone models, *Earth Planet. Sci. Lett.*, *237*, 781–797, doi:10.1016/j.epsl.2005.06.049.

Kohlstedt, D. L., B. Evans, and S. J. Mackwell (1995), Strength of the lithosphere: Constraints imposed by laboratory experiments, *J. Geophys. Res.*, *100*(B9), 17,587–17,602.

Lachenbruch, A. H., and J. H. Sass (1977), Heat flow in the United States and the thermal regime of the crust, in *The Earth's crust: its nature and physical properties*, *Geophys Monogr. Ser.*, vol. 20, edited by J. G. Heacock, pp. 626–675, AGU, Washington DC.

Lallemand, S., A. Heuret, and D. Boutelier (2005), On the relationships between slab dip, back-arc stress, upper plate absolute motion, and crustal nature in subduction zones, *Geochem., Geophys., Geosyst.*, *6*(9), Q09006, doi:10.1029/2005GC000917.

Lambeck, K., P. Johnston, and M. Nakada (1990), Holocene glacial rebound and sea-level change in NW Europe, *Geophys. J. Int.*, *103*(2), 451–468, doi:10.1111/j.1365-246X.1990.tb01784.x.

Le Pourhiet, L., M. Gurnis, and J. Saleeby (2006), Mantle instability beneath the Sierra Nevada Mountains in California and Death Valley extension, *Earth Planet. Sci. Lett.*, *251*, 104–119.

Lee, C.-T., R. L. Rudnick, and G. H. Brimhall, Jr. (2001), Deep lithospheric dynamics beneath the Sierra Nevada during the Mesozoic and Cenozoic as inferred from xenolith petrology, *Geochem., Geophys., Geosyst.*, *2*, 1–27.

Lemoine, F. G., S. C. Kenyon, J. K. Factor, R. G. Trimmer, N. K. Pavlis, D. S. Chinn, C. M. Cox, S. M. Klosko, S. B. Luthcke, M. H. Torrence, Y. M. Wang, R. G. Williamson, E. C. Pavlis, R. H. Rapp, and T. R. Olson (1998), The development of the joint NASA GSFC and NIMA geopotential model EGM96, *Tech. Rep. NASA/TP-1998-206861*, NASA Goddard Space Flight Center, Greenbelt, Maryland 20771 USA.

Lev, E., and B. H. Hager (2008), Rayleigh - Taylor instabilities with anisotropic lithospheric viscosity, *Geophys. J. Int.*, *173*(3), 806–814.

Liu, L., M. Gurnis, M. Seton, J. B. Saleeby, R. D. Müller, and J. M. Jackson (2010), The role of oceanic plateau subduction in the laramide orogeny, *Nature Geoscience*, pp. 1–5, doi:10.1038/NGEO829.

Long, M. D., and P. G. Silver (2008), The subduction zone flow field from seismic anisotropy: A global view, *Science*, *319*, 315–318, doi:10.1126/science.1150809.

Long, M. D., and P. G. Silver (2009), Shear wave splitting and mantle anisotropy: Measurements, interpretations, and new directions, *Surveys in Geophysics*, *30*, 407–461, doi:10.1007/s10712-009-9075-1.

Lorinczi, P., and G. A. Houseman (2009), Lithospheric gravitational instability beneath the southeast carpathians, in Press, Tectonophysics.

Manley, C. R., A. F. Glazner, and G. L. Farmer (2000), Timing of volcanism in the sierra nevada of california: Evidence for pliocene delamination of the batholithic root?, *Geology*, *28*(9), 811–814.

Marone, F., and B. Romanowicz (2007), The depth distribution of azimuthal anisotropy in the continental upper mantle, *Nature*, *447*, 198–201.

Masters, G., S. Johnson, G. Laske, H. Bolton, and J. H. Davies (1996), A shear-velocity model of the mantle, *Philos. Trans. R. Soc. London*, *354*, 1385–1411, doi:10.1098/rsta.1996.0054.

McAdoo, D. C. (1981), Geoid anomalies in the vicinity of subduction zones, *J. Geophys. Res.*, *86*(B7), 6073–6090.

McKenzie, D. (1969), Speculations on the consequences and causes of plate motions, *Geophys. J. R. astr. Soc.*, *18*, 1–32.

McKenzie, D. (1979), Finite deformation during fluid flow, *Geophys. J. R. astr. Soc.*, *58*, 689–715.

McKenzie, D., and M. J. Bickle (1988), The volume and composition of melt generated by extension of the lithosphere, *Journal of Petrology*, *29*(3), 625–679.

McNamara, D. E., W. R. Walter, T. J. Owens, and C. J. Ammon (1997), Upper mantle velocity structure beneath the Tibetan Plateau from Pn travel time tomography, *J. Geophys. Res.*, *102*(B1), 493–505.

Mégnin, C., and B. Romanowicz (2000), The three-dimensional shear velocity structure of the mantle from the inversion of body, surface and higher-mode waveforms, *Geophys. J. Int.*, *143*, 709–728.

Mitrovica, J. X. (1996), Haskell [1935] revisited, *J. Geophys. Res.*, *101*(B1), 555–569.

Mitrovica, J. X., and A. M. Forte (2004), A new inference of mantle viscosity based upon joint inversion of convection and glacial isostatic adjustment data, *Earth Planet. Sci. Lett.*, *225*, 177–189, doi:10.1016/j.epsl.2004.06.005.

Mitrovica, J. X., K. Latychev, and M. E. Tamisiea (2007), Time variable gravity: glacial isostatic adjustment, in *Treatise of Geophysics*, vol. 3, edited by T. Herring, pp. 197–211, Elsevier, doi:10.1016/B978-044452748-6.00175-9.

Molnar, P. (1990), S-wave residuals from earthquakes in the Tibetan region and lateral variations in the upper mantle, *Earth Planet. Sci. Lett.*, *101*, 68–77.

Molnar, P., and G. A. Houseman (2004), The effects of buoyant crust on the gravitational instability of thickened mantle lithosphere at zones of intracontinental convergence, *Geophys. J. Int.*, *158*, 1134–1150.

Molnar, P., and C. H. Jones (2004), A test of laboratory based rheological parameters of olivine from an analysis of late Cenozoic convective removal of mantle lithosphere beneath the Sierra Nevada, California, USA, *Geophys. J. Int.*, *156*, 555–564.

Molnar, P., G. A. Houseman, and C. P. Conrad (1998), Rayleigh-Taylor instability and convective thinning of mechanically thickened lithosphere: effects of non-linear viscosity decreasing exponentially with depth and of horizontal shortening of the layer, *Geophys. J. Int.*, *133*, 568–584.

Moresi, L., and M. Gurnis (1996), Constraints on the lateral strength of slabs from three-dimensional dynamic flow models, *Earth Planet. Sci. Lett.*, *138*, 15–28.

Moresi, L., S. Zhong, and M. Gurnis (1996), The accuracy of finite element solutions of Stoke's flow with strongly varying viscosity, *Phys. Earth Planet. Inter.*, *97*, 83–94.

Moresi, L.-N., and V. S. Solomatov (1995), Numerical investigation of 2D convection with extremely large viscosity variations, *Physics of Fluids*, *7*(9), 2154–2162.

Morris, J. D., W. P. Leeman, and F. Tera (1990), The subducted component in island arc lavas: constraints from Be isotopes and B-Be systematics, *Nature*, *344*, 31–36.

Müller, R. D., M. Sdrolias, C. Gaina, and W. R. Roest (2008), Age, spreading rates, and spreading asymmetry of the world's ocean crust, *Geochem., Geophys., Geosyst.*, *9*(4), Q04006, doi:10.1029/2007GC001743.

Nakada, M., and K. Lambeck (1989), Late Pleistocene and Holocene sea-level change in the Australian region and mantle rheology, *Geophys. J. Int.*, *96*, 497–517.

Neil, E. A., and G. A. Houseman (1999), Rayleigh-Taylor instability of the upper mantle and its role in intraplate orogeny, *Geophys. J. Int.*, *138*, 89–107.

Ni, J., and M. Barazangi (1983), High-frequency seismic wave propagation beneath the Indian Shield, Himalayan Arc, Tibetan Plateau and surrounding regions: high uppermost mantle velocities and efficient S_n propagation beneath Tibet, *Geophys. J. R. astr. Soc.*, *72*, 665–689.

Nyblade, A. A., and H. N. Pollack (1993), A global analysis of heat flow from Precambrian terrains: implications for the thermal structure of Archean and Proterozoic lithosphere, *J. Geophys. Res.*, *98*(B7), 12,207–12,218.

Owens, T. J., and G. Zandt (1997), Implications of crustal property variations for models of Tibetan plateau evolution, *Nature*, *387*, 37–43.

Özalaybey, S., and M. K. Savage (1995), Shear wave splitting beneath western United States in relation to plate tectonics, *J. Geophys. Res.*, *100*, 18,135–18,149.

Paulson, A., S. Zhong, and J. Wahr (2007a), Inference of mantle viscosity from GRACE and relative sea level data, *Geophys. J. Int.*, *171*, 497–508, doi:10.1111/j.1365-246X.2007.03556.x.

Paulson, A., S. Zhong, and J. Wahr (2007b), Limitations on the inversion for mantle viscosity from postglacial rebound, *Geophys. J. Int.*, *168*, 1195–1209, doi:10.1111/j.1365-246X.2006.03222.x.

Pearce, J. A., J. F. Bender, S. E. De Long, W. S. F. Kidd, P. J. Low, Y. Güner, F. Saroglu, Y. Yilmaz, S. Moorbath, and J. G. Mitchell (1990), Genesis of collision volcanism in Eastern Anatolia, Turkey, *Journal of Volcanology and Geothermal Research*, *44*, 189–229.

Peltier, W. R. (1976), Glacial-isostatic adjustment II. The inverse problem, *Geophys. J. R. astr. Soc.*, *46*, 669–705.

Peltier, W. R. (1998), Postglacial variations in the level of the sea: implications for climate dynamics and solid-earth geophysics, *Reviews of Geophysics*, *36*(4), 603–689.

Reeg, H., C. H. Jones, H. Gilbert, T. Owens, and G. Zandt (2007), Teleseismic travel-time tomography of the Sierra Nevada and its foundering lithosphere, *Eos Trans. AGU*, *88*(52), Abstract T33A–1150.

Ribe, N. M. (1989), Seismic anisotropy and mantle flow, *J. Geophys. Res.*, *94*, 4213–4223.

Ribe, N. M. (1992), On the relation between seismic anisotropy and finite strain, *J. Geophys. Res.*, *97*, 8737–8747.

Ribe, N. M. (2001), Bending and stretching of thin viscous sheets, *J. Fluid Mech.*, *433*, 135–160.

Ricard, Y., L. Fleitout, and C. Froidevaux (1984), Geoid heights and lithospheric stresses for a dynamical earth, *Ann. Geophys.*, *2*, 267–286.

Ricard, Y., C. Froidevaux, and L. Fleitout (1988), Global plate motion and the geoid: a physical model, *Geophys. J. (Oxford)*, *93*, 477–484.

Ricard, Y., M. Richards, C. Lithgow-Bertelloni, and Y. L. Stunff (1993), A geodynamic model of mantle density heterogeneity, *J. Geophys. Res.*, *98*(B12), 21,895–21,909.

Ritsema, J., H. Jan van Heijst, and J. H. Woodhouse (2004), Global transition zone tomography, *J. Geophys. Res.*, *109*, B02302, doi:10.1029/2003JB002610.

Rudnick, R. L., W. F. McDonough, and R. J. O'Connell (1998), Thermal structure, thickness and composition of continental lithosphere, *Chemical Geology*, *145*, 395–411.

Russo, R. M., and P. G. Silver (1994), Trench-parallel flow beneath the Nazca Plate from seismic anisotropy, *Science*, *263*, 1105–1111.

Saleeby, J., and Z. Foster (2004), Topographic response to mantle lithosphere removal in the southern Sierra Nevada region, California, *Geology*, *32*(3), 245–248.

Saltus, R. W., and A. H. Lachenbruch (1991), Thermal evolution of the Sierra Nevada: tectonic implications of new heat flow data, *Tectonics*, *10*, 325–344.

Savage, M. K. (1999), Seismic anisotropy and mantle deformation: What have we learned from shear wave splitting?, *Reviews of Geophysics*, *37*, 65–106.

Shapiro, N. M., and M. H. Ritzwoller (2002), Monte-Carlo inversion for a global shear-velocity model of the crust and upper mantle, *Geophys. J. Int.*, *151*, 88–105.

Sibson, R. H. (1977), Fault rocks and fault mechanisms, *J. Geol. Soc., Lond.*, *133*, 191–213.

Sibson, R. H. (1982), Fault zone models, heat flow, and the depth distribution of earthquakes in the continental crust of the United States, *Bull. Seismol. Soc. Amer.*, *72*, 151–163.

Silver, P. G. (1996), Seismic anisotropy beneath the continents: Probing the depths of geology, *Annu. Rev. Earth Planet Sci.*, *24*, 385–432.

Silver, P. G., S. S. Gao, K. H. Liu, and The Kaapvaal Seismic Group (2001), Mantle deformation beneath southern Africa, *Geophys. Res. Lett.*, *28*, 2493–2496.

Simons, F. J., and F. A. Dahlen (2006), Spherical Slepian functions and the polar gap in geodesy, *Geophys. J. Int.*, *166*, 1039–1061, doi:10.1111/j.1365-246X.2006.03065.x.

Simons, F. J., and R. D. van der Hilst (2002), Age-dependent seismic thickness and mechanical strength of the Australian lithosphere, *Geophys. Res. Lett.*, *29*(11), 1–4, doi: 10.1029/2002GL014962.

Simons, F. J., and R. D. van der Hilst (2003), Seismic and mechanical anisotropy and the past and present deformation of the Australian lithosphere, *Earth Planet. Sci. Lett.*, *211*, 271–286, doi:10.1016/S0012-821X(03)00198-5.

Simons, F. J., R. D. van der Hilst, J.-P. Montagner, and A. Zielhuis (2002), Multimode Rayleigh wave inversion for heterogeneity and azimuthal anisotropy of the Australian upper mantle, *Geophys. J. Int.*, *151*(3), 738–754, doi:10.1046/j.1365-246X.2002.01787.x.

Simons, F. J., R. D. van der Hilst, and M. T. Zuber (2003), Spatiospectral localization of isostatic coherence anisotropy in Australia and its relation to seismic anisotropy: Implications for lithospheric deformation, *J. Geophys. Res.*, *108*(B5), 2250, doi:10.1029/2001JB000704.

Simons, F. J., F. A. Dahlen, and M. A. Wieczorek (2006), Spatiospectral concentration on a sphere, *SIAM Review*, *48*(3), 504–536, doi:10.1137/S0036144504445765.

Simons, F. J., J. C. Hawthorne, and C. D. Beggan (2009), Efficient analysis and representation of geophysical processes using localized spherical basis functions, *Proc. SPIE*, *7446*(74460G), doi:10.1117/12.825730.

Simons, M., and B. H. Hager (1997), Localization of the gravity field and the signature of glacial rebound, *Nature*, *390*, 500–504.

Sleep, N. H. (1975), Stress and flow beneath island arcs, *Geophys. J. R. astr. Soc.*, *42*(3), 827–858.

Smith, G. P., D. A. Wiens, K. M. Fischer, L. M. Dorman, S. C. Webb, and J. A. Hildebrand (2001), A complex pattern of mantle flow in the Lau backarc, *Science*, *292*, 713–716, doi:10.1126/science.1058763.

Spiegelman, M., and D. McKenzie (1987), Simple 2-D models for melt extraction at mid-ocean ridges and island arcs, *Earth Planet. Sci. Lett.*, *83*, 137–152.

Stern, T., P. Molnar, D. Okaya, and D. Eberhart-Phillips (2000), Teleseismic P wave delays and modes of shortening the mantle lithosphere beneath South Island, New Zealand, *J. Geophys. Res.*, *105*(B9), 21,615–21,631.

Stern, T. A., W. R. Stratford, and M. L. Salmon (2006), Subduction evolution and mantle dynamics at a continental margin: Central North Island, New Zealand, *Reviews of Geophysics*, *44*, 1–36.

Stevenson, D. J., and J. S. Turner (1977), Angle of subduction, *Nature*, *270*, 334–336.

Stock, G. M., R. S. Anderson, and R. C. Finkel (2004), Pace of landscape evolution in the Sierra Nevada, California, revealed by cosmogenic dating of cave sediments, *Geology*, *32*, 193–196.

Stöckhert, B., and J. Renner (1998), Rheology of crustal rocks at ultrahigh pressure, in *When Continents Collide: Geodynamics and Geochemistry of Ultrahigh-Pressure Rocks*, edited by B. R. Hacker and J. G. Liou, chap. 3, pp. 57–95, Kluwer Academic Publishers.

Tamisiea, M. E., J. X. Mitrovica, and J. L. Davis (2007), GRACE gravity data constrain ancient ice geometries and continental dynamics over Laurentia, *Science*, *316*, 881–883, doi:10.1126/science.1137157.

Tao, W. C., and R. J. O'Connell (1993), Deformation of a weak subducted slab and variation of seismicity with depth, *Nature*, *361*, 626–628.

Tilmann, F., J. Ni, and INDEPTH III Seismic Team (2003), Seismic imaging of the downwelling Indian lithosphere beneath central Tibet, *Science*, *300*, 1424–1427.

Tovish, A., G. Schubert, and B. P. Luyendyk (1978), Mantle flow pressure and the angle of subduction: Non-Newtonian corner flows, *J. Geophys. Res.*, *83*(B12), 5892–5898.

Tsenn, M. C., and N. L. Carter (1987), Upper limits of power law creep of rocks, *Tectonophysics*, *136*, 1–26.

Turcotte, D. L., and E. R. Oxburgh (1967), Finite amplitude convection cells and continental drift, *J. Fluid Mech.*, *28*, 29–42.

Turcotte, D. L., and G. Schubert (2002), *Geodynamics*, vol. Second Edition, Cambridge University Press.

Turner, S., N. Arnaud, J. Liu, N. Rogers, C. Hawkesworth, N. Harris, S. Kelley, P. V. Calsteren, and W. Deng (1996), Post-collision, shoshonitic volcanism on the Tibetan Plateau: Implications for convective thinning of the lithosphere and the source of ocean island basalts, *Journal of Petrology*, *37*, 45–71.

Unruh, J. R. (1991), The uplift of the Sierra Nevada and implications for late Cenozoic epeirogeny in the western Cordillera, *Geol. Soc. Am. Bull.*, *103*, 1395–1404.

van Hunen, J., S. Zhong, N. M. Shapiro, and M. H. Ritzwoller (2005), New evidence for dislocation creep from 3-D geodynamic modeling of the Pacific upper mantle structure, *Earth Planet. Sci. Lett.*, *238*, 146–155, doi:10.1016/j.epsl.2005.07.006.

van Keken, P. E., C. Currie, S. D. King, M. D. Behn, A. Cagnioncle, J. He, R. F. Katz, S.-C. Lin, E. M. Parmentier, M. Spiegelman, and K. Wang (2007), A community benchmark for subduction zone modeling, *Phys. Earth Planet. Inter.*, *171*, 187–197, doi:10.1016/j.pepi.2008.04.015.

Verma, R. K. (1960), Elasticity of some high-density crystals, *J. Geophys. Res.*, *65*, 757–766.

Walker, K. T., G. H. R. Bokelmann, S. L. Klemperer, and A. A. Nyblade (2005), Shear-wave splitting around hotspots: Evidence for upwelling-related mantle flow?, *Spec. Pap. Geol. Soc. Am.*, *388*, 171–192.

Wessel, P., and W. H. F. Smith (1998), New, improved version of Generic Mapping Tools released, *Eos Trans. AGU*, *79*(47), 579.

Whitehead, J. A., and D. S. Luther (1975), Dynamics of laboratory diapir and plume models, *J. Geophys. Res.*, *92*, 4817–4825.

Wieczorek, M. A., and F. J. Simons (2005), Localized spectral analysis on the sphere, *Geophys. J. Int.*, *162*, 655–675, doi:10.1111/j.1365-246X.2005.02687.x.

Willett, S. D., and C. Beaumont (1994), Subduction of Asian lithospheric mantle beneath Tibet inferred from models of continental collision, *Nature*, *369*, 642–645.

Woodward, R. L., and P. Molnar (1995), Lateral heterogeneity in the upper mantle and SS-S traveltime intervals for SS rays reflected from the Tibetan Plateau and its surroundings, *Earth Planet. Sci. Lett.*, *135*, 139–148.

Wu, P., and W. R. Peltier (1982), Viscous gravitational relaxation, *Geophys. J. R. astr. Soc.*, *70*(2), 435–485.

Wu, P., and W. R. Peltier (1983), Glacial isostatic adjustment and the free air gravity anomaly as a constraint on deep mantle viscosity, *Geophys. J. R. astr. Soc.*, *74*, 377–450.

Yang, Y., and D. W. Forsyth (2006), Rayleigh wave phase velocities, small-scale convection, and azimuthal anisotropy beneath southern California, *J. Geophys. Res.*, *111*, 1–20.

Yuen, D. A., and R. Sabadini (1985), Viscosity stratification of the lower mantle as inferred from the J2 observation, *Ann. Geophys.*, *3*, 647–654.

Zhang, N., S. Zhong, W. Leng, and Z.-X. Li (2010), A model for the evolution of the earth's mantle structure since the early paleozoic, doi:10.1029/2009JB006896, in Press, JGR-Solid Earth.

Zhang, S., and S.-i. Karato (1995), Lattice preferred orientation of olivine aggregates deformed in simple shear, *Nature*, *375*, 774–777.

Zhao, W.-L., and W. J. Morgan (1985), Uplift of Tibetan Plateau, *Tectonics*, *4*(4), 359–369.

Zhong, S. (2001), Role of ocean-continent contrast and continental keels on plate motion, net rotation of lithosphere, and the geoid, *J. Geophys. Res.*, *106*(B1), 703–712.

Zhong, S. (2006), Constraints on thermochemical convection of the mantle from plume heat flux, plume excess temperature, and upper mantle temperature, *J. Geophys. Res.*, *111*, B04409.

Zhong, S., and M. Gurnis (1995), Towards a realistic simulation of plate margins in mantle convection, *Geophys. Res. Lett.*, *22*(8), 981–984.

Appendix A

Linear (First-Order) Stability Analysis

In our examination of Rayleigh–Taylor instabilities we perform a linear stability analysis in cases of constant density to find analytical solutions for growth rate q' as a function of wavenumber, k' (*Conrad and Molnar*, 1997; *Molnar et al.*, 1998; *Chandrasekhar*, 1961). This derivation is mainly an expansion of *Conrad and Molnar* (1997) and corrects some typographic errors.

The governing equations for 2-D incompressible flow with small Reynolds number include the Stokes equations (x and z components respectively)

$$\begin{aligned} 0 &= \frac{\partial \sigma_{xx}}{\partial x} + \frac{\partial \sigma_{xz}}{\partial z} \\ 0 &= \frac{\partial \sigma_{xz}}{\partial x} + \frac{\partial \sigma_{zz}}{\partial z} - \rho g \end{aligned} \tag{A.1}$$

and the continuity equation for incompressibility

$$\nabla \cdot \mathbf{u} = \frac{\partial u}{\partial x} + \frac{\partial w}{\partial z} = 0. \tag{A.2}$$

Here u and w are the velocities in the x and z directions, respectively, σ_{xx} is the stress acting in the x direction on a plane perpendicular to x (i.e. a normal stress), σ_{xz} is the stress acting in the x direction on a plane perpendicular to z (i.e. a shear stress), ρ is density, and g is gravity, which acts in the negative z direction. For the first order analysis we consider first order perturbations to the stress and strain rate, defined as

$$\tilde{\sigma}_{xx} = \frac{2\bar{\eta}}{n}\tilde{\epsilon}_{xx} - \tilde{p}, \qquad \tilde{\sigma}_{zz} = \frac{2\bar{\eta}}{n}\tilde{\epsilon}_{zz} - \tilde{p}, \qquad \tilde{\sigma}_{xz} = 2\bar{\eta}\tilde{\epsilon}_{xz}. \tag{A.3}$$

where tildes indicate perturbations to the background field, $\bar{\eta}$ is viscosity, and $\tilde{p}$ is pressure, from *Conrad and Molnar* (1997). Using these, and assuming viscosity is an exponential function of depth (z), Equation A.1 becomes

$$\begin{aligned} 0 &= \frac{2\bar{\eta}}{n}\tilde{u}_{xx} - \tilde{p}_x + \bar{\eta}(\tilde{u}_{zz} + \tilde{w}_{xz}) + \gamma\bar{\eta}(\tilde{u}_z + \tilde{w}_x) \\ 0 &= \bar{\eta}(\tilde{u}_{xz} + \tilde{w}_{xx}) + \frac{2\bar{\eta}}{n}\tilde{w}_{zz} + \frac{2\gamma\bar{\eta}}{n}\tilde{w}_z - \tilde{p}_z - \tilde{\rho}g \end{aligned} \tag{A.4}$$

with $\tilde{\rho}$, the density perturbation, resulting from the expansion of pressure, $\tilde{p}$. Here we begin using the convention that subscripts indicate partial derivatives. From *Chandrasekhar* (1961), we seek solutions that have a sinusoidal dependence in x, as:

$$e^{ikx} \tag{A.5}$$

where k is wavenumber. So we expand A.4 to

$$\begin{aligned} ik\tilde{p} &= -\frac{2\bar{\eta}k^2}{n}\tilde{u} + \bar{\eta}(D^2\tilde{u} + ikD\tilde{w}) + \gamma\bar{\eta}(D\tilde{u} + ik\tilde{w}) \\ D\tilde{p} &= \bar{\eta}(ikD\tilde{u} - k^2\tilde{w}) + \frac{2\bar{\eta}}{n}D^2\tilde{w} + \frac{2\gamma\bar{\eta}}{n}D\tilde{w} - \tilde{\rho}g \end{aligned} \tag{A.6}$$

where D is the derivative $\partial/\partial z$. Now using the continuity equation

$$\nabla \cdot \mathbf{u} = ik\tilde{u} + D\tilde{w} = 0 \tag{A.7}$$

we have

$$ik\tilde{u} = -D\tilde{w}. \tag{A.8}$$

Then

$$\begin{aligned} ik\tilde{p} &= -\bar{\eta}k^2\left(\frac{2}{n}-1\right)\tilde{u}+\bar{\eta}D^2\tilde{u}+\gamma\bar{\eta}\left(D\tilde{u}+ik\tilde{w}\right) \\ D\tilde{p} &= -\bar{\eta}\left(D^2+k^2\right)\tilde{w}+\frac{2\bar{\eta}}{n}D^2\tilde{w}+\frac{2\gamma\bar{\eta}}{n}D\tilde{w}-\tilde{\rho}g \end{aligned} \tag{A.9}$$

and taking $\partial/\partial x$ through both sides, remembering (A.8), we have

$$\begin{aligned} k^2\tilde{p} &= \bar{\eta}k^2\left(\frac{2}{n}-1\right)D\tilde{w}+\bar{\eta}D^3\tilde{w}+\gamma\bar{\eta}\left(D^2+k^2\right)\tilde{w} \\ D\tilde{p} &= -\bar{\eta}\left(D^2+k^2\right)\tilde{w}+\frac{2\bar{\eta}}{n}D^2\tilde{w}+\frac{2\gamma\bar{\eta}}{n}D\tilde{w}-\tilde{\rho}g. \end{aligned} \tag{A.10}$$

Now to eliminate pressure, $\tilde{p}$, between these equations, we multiply the z component by k^2 and get

$$k^2D\tilde{p} = -k^2\bar{\eta}(D^2+k^2)\tilde{w}+\frac{2\bar{\eta}k^2}{n}D^2\tilde{w}+\frac{2\gamma\bar{\eta}k^2}{n}D\tilde{w}-\tilde{\rho}gk^2 \tag{A.11}$$

and take $\partial/\partial z$ of the x component via four chain rules to get

$$\begin{aligned} k^2D\tilde{p} = \bar{\eta}D^4\tilde{w}+2\gamma\bar{\eta}D^3\tilde{w}+\left[-\bar{\eta}k^2\left(\frac{2}{n}-1\right)(\gamma+1)+\gamma^2\bar{\eta}\right]D^2\tilde{w} \\ +\gamma\bar{\eta}k^2D\tilde{w}+\gamma^2\bar{\eta}k^2\tilde{w}. \end{aligned} \tag{A.12}$$

Setting these two equations equal yields

$$\begin{aligned} D^4\tilde{w}+2\gamma D^3\tilde{w}+\left[\gamma^2-2k^2\left(\frac{2}{n}-1\right)\right]D^2\tilde{w}-2k^2\gamma\left(\frac{2}{n}-1\right)D\tilde{w} \\ +(\gamma^2+k^2)k^2\tilde{w} = -\frac{\tilde{\rho}gk^2}{\bar{\eta}}. \end{aligned} \tag{A.13}$$

With conservation of mass we require

$$\frac{\partial\tilde{\rho}}{\partial t}+u\frac{\partial\bar{\rho}}{\partial x}+w\frac{\partial\bar{\rho}}{\partial z}=0. \tag{A.14}$$

Then, assuming exponential growth, $\tilde{w}\approx e^{qt}$, from density perturbations only in the z direction, we have

$$q\tilde{\rho} = -\tilde{w}\frac{\partial \bar{\rho}}{\partial z} \tag{A.15}$$

which we can substitute into (A.13), the result of which is a homogeneous differential equation:

$$\begin{aligned} D^4\tilde{w} + 2\gamma D^3\tilde{w} + \left[\gamma^2 - 2k^2(\frac{2}{n} - 1)\right] D^2\tilde{w} - 2k^2\gamma(\frac{2}{n} - 1)D\tilde{w} \\ + (\gamma^2 + k^2 - \frac{gk^2}{\bar{\eta}q}D\bar{\rho})\tilde{w} = 0 \end{aligned} \tag{A.16}$$

A solution to this from *Bassi and Bonnin* (1988) is

$$\begin{aligned} W = Acos(\beta kz)e^{\alpha' kz} + B\frac{sin(\beta kz)}{\beta k}e^{\alpha' kz} \\ + Ccos(\beta kz)e^{\alpha'' kz} + D\frac{sin(\beta kz)}{\beta k}e^{\alpha'' kz} \end{aligned} \tag{A.17}$$

where W represents the downward velocity and

$$\begin{aligned} &\beta = \frac{r}{a}, \qquad \alpha' = a - \frac{m}{2}, \qquad \alpha'' = -a - \frac{m}{2}, \\ &r = \left(\frac{m^2}{4} + \frac{n-1}{n^2}\right)^{1/2}, \\ &a = \left\{\frac{m^2}{8} + \frac{1}{n} - \frac{1}{2} + \frac{1}{2}\left[\frac{m^4}{16} + \frac{m^2}{2}\left(\frac{2}{n} + 1\right) + 1\right]^{1/2}\right\}^{1/2}, \\ &m = \frac{\gamma}{k} = \frac{1}{kL}. \end{aligned} \tag{A.18}$$

We solve Equation A.17 in each material for the undetermined coefficients. In the case of a layer over an infinite halfspace, Figure 2.2, we use the boundary conditions shown. For the lower halfspace, $C = D = 0$ to prevent divergence at large negative z. So, we require six boundary conditions to find a full solution. These boundary conditions are: no vertical velocity at the top boundary, $z = h$, $\tilde{w}_1(h) = 0$, no horizontal velocity at the top

boundary $\tilde{u}_1(h) = 0$ or no shear stress at the top boundary $\tilde{\sigma}_{1,xz}(h) = 0$, continuity of vertical and horizontal velocity at the interface $\tilde{w}_1(0) = \tilde{w}_2(0)$ and $\tilde{u}_1(0) = \tilde{u}_2(0)$, continuity of shear stress on the interface $\tilde{\sigma}_{1,xz} = \tilde{\sigma}_{2,xz}$, and continuity of normal stress at the interface $\tilde{\sigma}_{1,zz}(0) - \tilde{\sigma}_{2,zz}(0) + \tilde{w}_2(0)\bar{\eta}_1(0)/(q'L) = 0$. The second boundary condition has an important distinction. Much of the previous Rayleigh-Taylor work has been focused on a fixed top condition, where horizontal velocity is zero. *Conrad and Molnar* (1997) *Molnar et al.* (1998) *Houseman and Molnar* (1997) However, a free top condition, where supported shear stress on the upper boundary is zero, functions as the other end member of possible crust and mantle lithosphere coupling. This coupling is a controlling factor in how the growth rate varies with wavenumber. Generally, reduced coupling tends to enhance the growth rate at longer wavelengths. Here we focus on experiments with a free top condition to further quantify this effect on longer wavelengths.

The boundary conditions involving vertical velocity, $\tilde{w}$, are directly solved from equation A.17. Those with horizontal velocity can be derived from equation A.7 so that

$$\tilde{u}(z) = -\frac{1}{ik}\frac{\partial \tilde{w}}{\partial z}(z). \tag{A.19}$$

Shear stress continuity is developed from equations A.3 and A.7 as

$$\tilde{\sigma}_{xz} = -\frac{\bar{\eta}}{ik}(D^2 + k^2)\tilde{w}. \tag{A.20}$$

Normal stress continuity on the sloped boundary is written as

$$\tilde{\sigma}_{1,zz} - \tilde{\sigma}_{2,zz} = -(\rho_1 - \rho_2)g\varphi \tag{A.21}$$

where φ is the z-coordinate of the perturbed boundary away from the original depth of $z = 0$. The right hand side of this equation represents pressure change due to the perturbation of the layer interface.

The six equations satisfying the boundary conditions (or more for complex problems) are assembled in matrix form as

$$\mathbf{MC} = 0 \tag{A.22}$$

where $\mathbf{C}$ is the vector of undetermined coefficients. This vector can be nonzero only when $det(\mathbf{M}) = 0$, and so we solve this to find an equation of growth rate. *Conrad and Molnar* (1997)

In the process, we define the nondimensionalization of q' and k' to include the exponential scaling of viscosity as

$$q = \frac{(\rho_1 - \rho_2)gL}{\eta_0} q' \quad \text{and} \quad k' = kL \tag{A.23}$$

and incorporate them into the solution. The growth rate will now be a function of two parameters: k' which is non-dimensional wavenumber, and h/L which is the layer thickness divided by the e-folding length of the exponential viscosity. *Molnar et al.* (1998)